SAPIENZA
UNIVERSITÀ DI ROMA

Development of tools for quality control on therapeutic carbon beams with a fast-MC code (FRED)

Dottorato di Ricerca in Fisica degli acceleratori – XXXIII Ciclo

Candidate

Micol De Simoni

ID number 1478632

Thesis Advisor

Prof. Vincenzo Patera

Co-Advisor

Prof. Angelo Schiavi

2019/2020

Development of tools for quality control on therapeutic carbon beams with a fast-MC code (FRED)

Ph.D. thesis. Sapienza – University of Rome

This thesis has been typeset by LaTeX and the Sapthesis class.

Author's email: micol.desimoni@uniroma1.it

A Rudy ed Egon

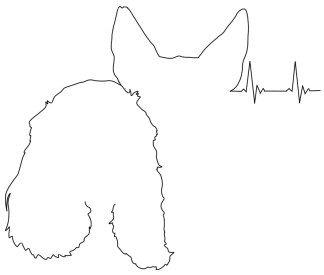

Contents

Introduction

In the fight against tumors, different types of cancer require different ways of treatment: surgery, radiotherapy, chemotherapy, hormone therapy and immunotherapy often used in combination with each other.
About 50% of cancer patients undergo radiotherapy treatment which exploits the ability of ionizing radiation to damage the genetic heritage of cancer cells, causing apoptosis and preventing their reproduction. The non-invasive nature of radiation represents a viable alternative for those tumors that are not surgically operable because they are localized in hardly reachable anatomical sites or on organs which removal would be too disabling for the patient.
A new frontier of radiotherapy is represented by Particle Therapy (PT). It consists of the use of accelerated charged particle beams (in particular protons and carbon ions) to irradiate solid tumors. The main advantage of such a technique with respect to the standard radiotherapy using x-rays/electron beams is in the different longitudinal energy release profiles. While photons' longitudinal dose release is characterized by a slow exponential decrease, for charged particles a sharp peak at the end of the path provides a more selective energy release. By conveniently controlling the peak position it is possible to concentrate the dose (expressed as the energy release per unit mass) to tumors and, at the same time, preserve surrounding healthy tissues.
In particle therapy treatments, the achieved steep dose gradients demand highly accurate modelling of the interaction of beam particles with tissues. The high ballistic precision of hadrons may result in a superior delivered dose distribution compared to conventional radiotherapy only if accompanied by a precise patient positioning and highly accurate treatment planning. This second operation is performed by the Treatment Planning System (TPS), sophisticated software that provides position, intensity and direction of the beams to the accelerator control system. Nowadays one of the major issues related to the TPS based on Monte Carlo (MC) is the high computational time required to meet the demand for high accuracy.
The code **FRED** (*Fast paRticle thErapy Dose evaluator*) has been developed to allow a fast optimization of treatment plans in proton therapy while profiting from the dose release accuracy of a MC tool [1]. Within FRED, the proton interactions are described with the precision level available in leading-edge MC tools used for medical physics applications, with the advantage of reducing the simulation time up to a factor of 1000. In this way, it allows a MC plan recalculation in a few minutes on GPU (*Graphics Processing Unit*) cards, instead of several hours on CPU (*Central Processing Unit*) hardware.
For the exceptional speed of the proton tracking algorithms implemented in FRED and for the excellent results achieved, the door to several applications within the particle therapy field has been opened. In particular, the success of FRED with protons determined the interest of CNAO (*Centro Nazionale di Adroterapia Oncologica*) center in Pavia to develop FRED also for carbon therapy applications, to recalculate treatment plans with carbon ions. Among the several differences between proton and

carbon beams, the nuclear fragmentation of the projectile in a ^{12}C treatment, which does not occur with protons, is certainly the most important. The simulation of the ion beam fragmentation gives an important contribution to the dose deposition. The total dose released is due not only to the primary beam but also to secondary and tertiary particles. Also for proton beams, there are secondary particles, mostly secondary protons from target fragmentation, which contribute on the level of some percent to the dose deposition for higher proton beam energies. However, fragments of the projectile, produced only by carbon beams, having on average the same energy per nucleon of the primary beam and a lower mass, can release dose after the peak causing the well-known fragmentation tail.

The goal of this thesis is the complete development of a GPU MC for carbon therapy in FRED framework. This work includes the complete modelling of the interaction between the beam and a patient, balancing the speed of calculation with the accuracy of implemented physical models. As far as possible, despite the lack of experimental data in the energy range of PT, the nuclear model has been implemented as a data-driven tracking model of carbon ions.

In Chapter 1 the main radio-biological and physical aspects of protons and ions beams will be presented. This chapter is crucial to understand the efficiency of this technique and its characteristics but also to have a first approach to the physical behaviour of ions that have been implemented in the code. Moreover, a comparison between proton and carbon ion beams and the photon beams used in radiotherapy will be shown to highlight the differences between these techniques.

Chapter 2 is focused on what happens before the beam arrives at the patient starting from the acceleration of the ions. After a description of the basic concepts of accelerator machines, cyclotrons and synchrotron will be described. Different beam delivery techniques used in PT to obtain the desired deposition of dose in the tumor will be presented. Then, the differences between analytic TPS and MC TPS will be described. At the end of the chapter, the dose monitoring techniques presently used will be shown.

In Chapter 3 a comparison between the full-MC, in particular FLUKA, and the new fast-MC FRED will be presented, with an emphasis on the time performance comparison. For what concerns FRED, a state of the art of fast-MC with protons will be described while the implementation of ions will be presented in a specific chapter.

In Chapter 4 the physical model implemented in the code for carbon ion therapy will be presented. The adjustments done to the ionization energy loss and multiple scattering of ions will be described. It will be shown how the nuclear model, entirely new in the code, has been developed parameterizing existent data. The implementation of the Local Effect Model (LEM I) in the code will be described as well. This model is necessary to calculate the Relative Biological Effectiveness (RBE) and the RBE-weighted dose used to obtain the TPS.

In Chapter 5 results obtained after having implemented the new models will be described. A first test has been done comparing FRED with a full-MC observing the distribution of dose, RBE and RBE-weighted dose for single pencil beams of carbon ion at different energies in a water target and then simulating a cube of dose. Finally, the few experiments found in the literature at the energy range of PT have been simulated and results have been compared with the ones reported in the papers.

Chapter 1

Particle Therapy

Cancer represents, in North European countries, the United States and Australia, the second cause of death (30%) after cardiovascular diseases. To treat cancer patients it is possible to choose between different therapy techniques depending on the kind of tumor, dimension, position and general health conditions of the patient. Different oncological therapies in most cases are used in combination between them to have the highest possible effectiveness in tumor control.
The surgical removal of the tumor mass is a very effective strategy when localized, but it is not always feasible, for instance, due to the proximity of cancer to so-called Organs At Risk (OAR) or the peculiarity of the affected tissue (such as liver tumors or some cases of pancreas tumors).
Chemotherapy is usually used in case of tumor rapid cell replication rate. It exploits anti-tumor drugs to kill cancer cells and, differently from surgery and radiotherapy which are local (or loco-regional) treatments, chemotherapy belongs to the group of systemic treatments (together with immunotherapy, hormonotherapy, etc.). The main disadvantage of such a technique is the relevant side effects related to drug aggressiveness.
Standard radiotherapy (RT) consists of the irradiation of the tumors with X-rays or γ-rays. Due to its ability to control tumor growth, RT is essential in cancer treatment. Radiotherapy has as well some limitations, mainly related to the dose released by the photon beam to the healthy tissue surroundings the tumor volume. To limit these problems a possible alternative to conventional radiotherapy is Particle Therapy (PT). It consists of the irradiation of tumor volume with beams of charged particles, typically protons and carbon ions. The main advantage of hadrons, compared to photons used in standard radiotherapy, lies in their favorable energy release. As it can be observed in Fig. 1.8, while photons energy released in the absorber medium decreases exponentially as a function of penetration depth, hadrons have different behavior: at the beginning their energy release is very low and a considerable part of the energy is deposited at the end of the range in a sharp peak, called Bragg Peak (BP). This typical feature provides a dose distribution conformal to the tumor, with consequent reduction of damage to healthy tissues.
In this chapter, the feature of particle therapy beams is described to understand how and when they can be a better choice to treat a tumor with respect to photons.

1.1 Physical bases

The purpose of this section is to describe the physical processes that drive the dose released in PT. The interaction of charged particles crossing a material is

well known. In a general treatment on the interaction of charged particles with matter, e^- and e^+ have to be distinguished from heavier charged particles (muons, protons, pions, α-particles, and other heavier ions), since different physics processes are involved. According to the goal of this thesis, only the physics of heavy charged particles will be treated.

1.1.1 Stopping Power

The stopping power is the average energy loss by a charged particle per unit path length. The processes that make the primary particle lose its energy can be related to electronic or nuclear interactions. The stopping power takes into account both contributes and it depends on the properties of incident particles and of the crossed materials. Since the nuclear stopping power is not relevant for the projectiles and energies of interest of particle therapy, in this thesis only the electronic stopping power will be presented. The formula that describes the energy loss by charged particles heavier than electrons is the Bethe-Bloch formula [2]:

$$-\frac{dE}{dx} = \frac{2\pi N_A Z m_e c^2 \rho z^2 r_e^2}{A\beta^2}\left[ln\left(\frac{2m_e\gamma^2 v^2 T_e^{max}}{I^2}\right) - 2\beta^2 - \delta(\beta\gamma) - 2\frac{C}{Z}\right], \quad (1.1)$$

where N_A is the Avogadro's number, z is the incident particle charge, m_e and r_e are the mass and the classical radius of an electron, ρ is the density of the material crossed, T_e^{max} is the maximum energy transferred to an electron in a single collision, Z and A are the atomic and mass number, I is the mean excitation potential expressed in eV, $\delta(\beta\gamma)$ and C are two corrective terms.
The maximum energy that a particle of mass M can transfer in the collision with an electron of mass m_e is:

$$T_e^{max} = \frac{2m_e c^2 \eta^2}{1 + 2s\sqrt{1+\eta^2} + s^2}, \quad (1.2)$$

where $\eta = \beta\gamma$ and $s = \frac{m_e}{M}$. If $M \gg m_e$, it is possible to approximate:

$$T_e^{max} \simeq 2m_e c^2 \eta^2, \quad (1.3)$$

which corresponds at almost 1/500 of the particle energy per nucleons.
The therm δ is the density correction to ionization energy loss. It becomes important at high energies because, along the path of the incident particles, their electric field tends to polarize target atoms encountered. Therefore, all the collisions with the outer electrons will contribute less to the total energy loss than predicted by the Bethe-Bloch equation (Eq. 1.1).
C represents the shells correction to ionization energy loss. The contribution of this factor is significant at low energies when the particle velocity is equal to or even lower than the velocity of orbital electrons. In this case, the assumption made to develop the Bethe-Bloch formula (Eq. 1.1), that is the stationary of the orbital electron with respect to the incident particle, is not valid anymore.
The excitation potential I is an important parameter usually determined experimentally for each element or material.
A semi-empirical method to compute I is described by the following equations:

$$I = 12Z + 7 \quad \text{for} \quad Z < 13 \quad (1.4)$$

$$I = 9.76Z + 5.58Z^{-0.19} \quad \text{for} \quad Z \geq 13 \tag{1.5}$$

For liquid water, I is often set to 75 eV.
The stopping power in several materials is shown in Fig. 1.1. Except in hydrogen, particles with the same velocity have similar rates of energy loss in different materials, although there is a slow decrease in the rate of energy loss with increasing Z. The different behavior at high energies between a gas (He in the figure) and the other materials is due to the density-effect correction, δ, discussed previously.

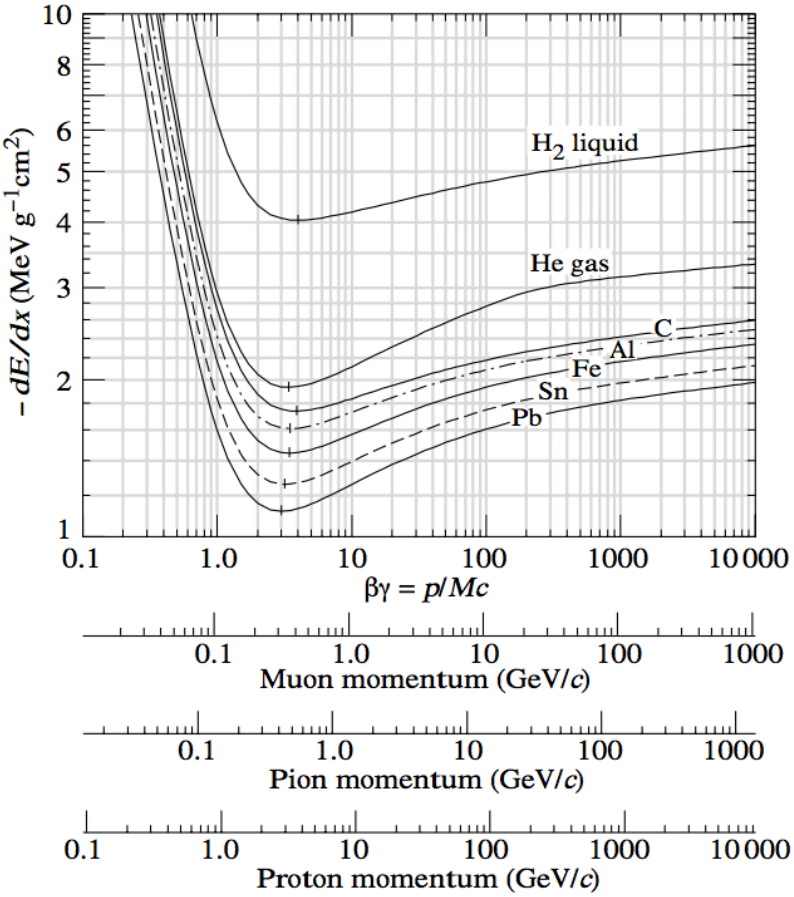

Figure 1.1. Mean energy loss rate in liquid (bubble chamber) hydrogen, gaseous helium, carbon, aluminum, iron, tin, and lead [3].

At low energies, the dominant contribution in the Bethe-Bloch formula (Eq. 1.1) is due to the $1/\beta^2$ factor, then the stopping power decreases until it reaches the minimum around 0.96c, where c is the velocity of light. This point is where the particle is referred to as the Minimum Ionization Particle (MIP). From the MIP point, the factor $1/\beta^2$ remains almost constant, the logarithmic factor prevails and makes the stopping power slowly increase as particle energy increases, while the density correction compensates the relativistic rise and reduces the slope. In Fig. 1.2 is reported the stopping power for different particles with respect to the kinetic energy.
Following these features, when a charged particle penetrates inside a material its

stopping power goes from low values to greater values (after the crossing of the MIP point). This means that, while at the entrance channel it has a small energy release per unit path length, then the energy loss increases considerably as its velocity becomes lower. At the end of the path, the particle is slow enough to have a velocity comparable with atomic electrons: this condition promotes target atoms ionization with consequent reduction of the stopping power.

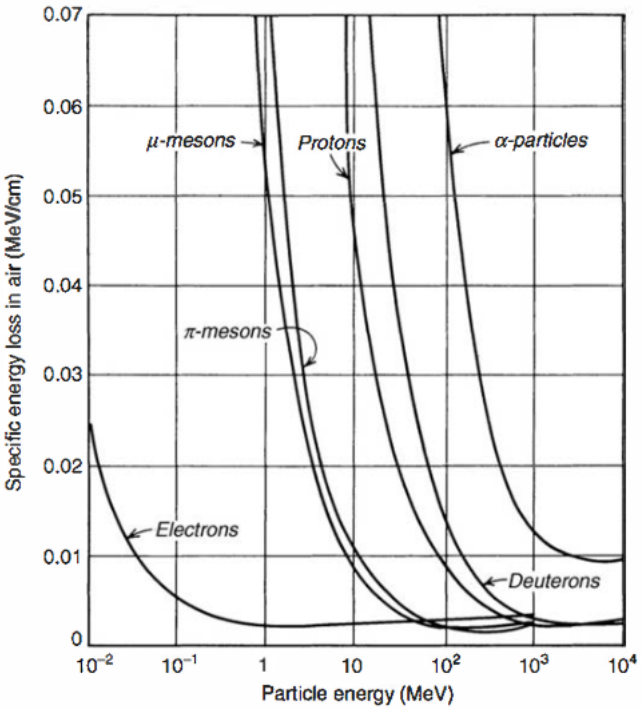

Figure 1.2. Energy loss in air versus the energy of different charged particles [3].

1.1.2 Energy Straggling

The interactions of charged particles with atomic nuclei have statistical nature, for this reason the energy lost by a particle in a layer of material is not exactly equal to the stopping power (Sec 1.1.1) multiplied by the thickness crossed. It is distributed with an energy straggling probability function that depends on the particle energy and material properties.
Two different regimes, thick and thin absorber regimes, can be identified and the k parameter can be used to distinguish them:

$$k = \frac{\xi}{T_e^{max}}, \tag{1.6}$$

where T_e^{max} is the maximum energy transferable by a projectile to an electron in a single collision, described in the Eq.1.2. The ξ parameter is the characteristic energy loss corresponding to the leading term in the Bethe–Bloch formula:

$$\xi = \frac{153.4 z^2 Z \rho \delta z}{\beta^2 A} keV, \tag{1.7}$$

where z and Z/A are the ion charge state and the particle atomic number over atomic mass ratio of the medium with density ρ.

Thick absorber regime

Following Seltzer and Berger [4], there is the thick absorber regime when $k \geq 10$. In this regime, the number of collisions suffered by the incoming particle is large and the energy fluctuations can be well approximated by a Gaussian distribution centered on the mean energy loss value given by the stopping power (Sec. 1.1.1). The standard deviation of the distribution is computed as follows [4]:

$$\sigma_E^2 = \xi T_e^{max} \left(1 - \frac{1}{2}\beta^2\right) \text{MeV}^2, \tag{1.8}$$

where T_e^{max} and ξ are described respectively by Eq. 1.2 and Eq. 1.7.

Thin absorber regime

The $k < 10$ condition defines the thin absorber regime, when the number of collision is not enough to lead to a Gaussian distribution of energy loss. The energy fluctuation is well described by the model developed by *Landau* [5] and *Vavilov* [6]. Landau was the first to develop a model for very thin layers ($k < 0.01$). He formulated an universal expression to be computed numerically:

$$f(\epsilon, \delta x) = \frac{1}{\xi}\phi(\lambda), \tag{1.9}$$

where f is the Landau energy loss distribution, δx is the path-length, ξ is described by Eq. 1.7 and:

$$\phi(\lambda) = \frac{1}{2\pi i}\int_{c-i\infty}^{c+i\infty} e^{u+ln(u)+\lambda u} du, \tag{1.10}$$

$$\lambda = \frac{\epsilon - \bar{\epsilon}}{\xi} - \gamma' - \beta^2 - ln\frac{\xi}{T_e^{max}}. \tag{1.11}$$

In these equations $c \geq 0$, $\gamma' = 1 - \gamma$ where γ is the Euler's constant, $\bar{\epsilon}$ and ϵ are respectively the average and the actual energy loss and T_e^{max} is described by Eq. 1.2.
In Landau's theory there is one crucial restriction: the average value of the distribution is infinite and if the number of steps is large the average fluctuation could be greater than zero. One solution to this problem is to set a maximum value of extracted variable λ to be accepted.
For $0.01 \leq k < 10$, a more accurate straggling distribution that solves also the infinite average energy issue was derived by *Vavilov* [6]. He worked out the following expression for the energy loss distribution:

$$f(\epsilon, \delta f) = \frac{1}{\xi}\phi_v(\lambda_v, k, \beta^2), \tag{1.12}$$

where:

$$\phi_v(\lambda_v, k, \beta^2) = \frac{1}{\pi i}\int_{c-i\infty}^{c+i\infty} \phi(s) e^{\lambda s} ds, \tag{1.13}$$

$$\phi(s) = e^{k(1+\beta^2\gamma)} e^{\psi(s)}, \tag{1.14}$$

$$\psi(s) = slnk + (s + \beta^2 k)[ln(s/k) + E_1(s/k)] - ke^{-s/k}, \tag{1.15}$$

where $E_1(z)$ is an exponential integral. Vavilov variable λ_v is related to λ by the relation:

$$\lambda_v = k(\lambda + logk). \tag{1.16}$$

1.1.3 Range

The range is defined as the path that a particle can travel before losing all its energy and stop. The range can be computed by integrating the inverse of the stopping power in the full energy spectrum of the incident particle E_p:

$$R(E_p) = \int_0^{E_p} \frac{dE}{-dE/dx}. \tag{1.17}$$

It depends on the initial particle kinetic energy, the type of the incident particle and the material crossed.

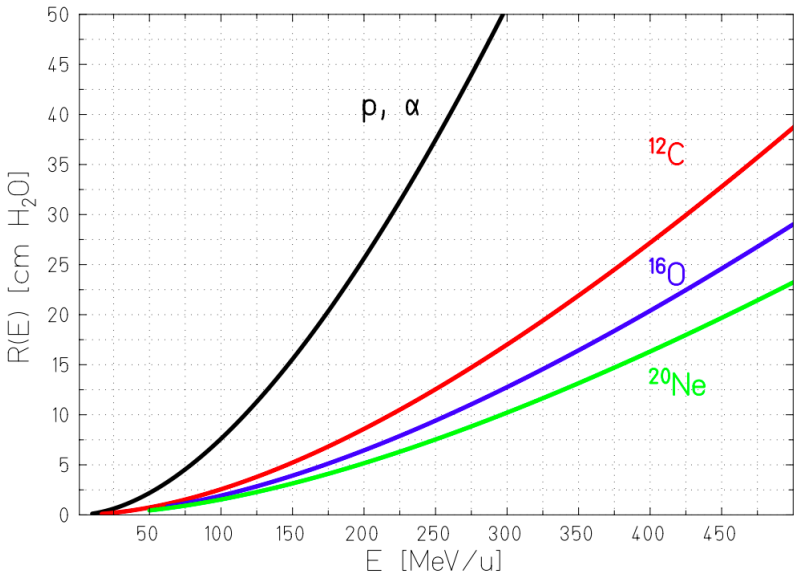

Figure 1.3. Mean range of ions in water versus their energy per nucleons [7].

To study the relation between the range and particle type for a fixed material, it is possible to differentiate the relation $E = m_p \gamma c^2$ respect to β:

$$\frac{dE}{d\beta} = m_p c^2 \frac{\beta^{3/2}}{1 - \beta^2} = m_p f(\beta), \tag{1.18}$$

where $f(\beta)$ is a function of β.
For a fixed material, the stopping power is a function only of the charge and the velocity:

$$\frac{dE}{dx} = z^2 g(\beta), \tag{1.19}$$

so, it is possible to express the range as:

$$R(E) = \frac{m_p}{z^2} \int_0^{\beta} \frac{f(\beta)}{g(\beta)} d\beta = \frac{m_p}{z^2} h(\beta), \tag{1.20}$$

where $h(\beta)$ is a function that depends only on the initial velocity of the particle. So, as it is possible to observe in Fig. 1.3, for a fixed material and fixed beam energy, the range scales with a factor m_p/z^2, which can be express also as A/z^2.
Because of multiple Coulomb scattering, that will be described in the Sec. 1.1.4, particles continuously change their direction, so the depth at which the particle stops fluctuates around the particle range.

1.1.4 Multiple Coulomb Scattering

Multiple scattering defines the process in which a particle undergoes a large succession of interactions that cause a change of direction. It is usually called multiple Coulomb scattering because it is dominated by electrostatic or Coulombian forces.
Several theories of multiple scattering have been formulated in small-angle approximations. A classical treatment is due to *Molière* [8]. In this section, features of the process will be described, with particular attention to the three approximations of the Molière theory implemented in the code.

Molière Theory

The complete treatment of the Molière theory [8] would require a very long derivation. We will describe a simple case with some assumptions:

- the target crossed by the particle beam is made of a single element;
- the material is thin enough that the energy of the particle can be considered constant;
- the scattering angle θ with respect to the initial direction of the beam is small, to approximate $sin\theta$ with θ.

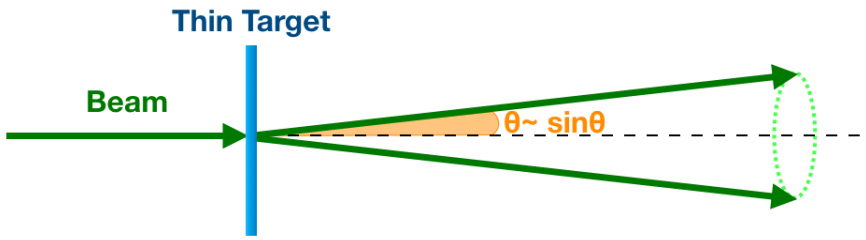

Figure 1.4. The scattering angle θ with respect to the initial direction of the beam due to its crossing through a thin and homogeneous material is shown.

Before computing the scattering angle θ, some quantities have to be defined. The *characteristic single scattering angle* χ_c is given by:

$$\chi_c^2 = \frac{c_1 t}{(pv)^2}, \tag{1.21}$$

where p and v are respectively the particle momentum and velocity, and c_1 is defined as:

$$c_1 = 4\pi N_A \alpha (\hbar c)^2 \frac{z^2 Z^2}{A}, \tag{1.22}$$

where N_A is the Avogadro's number, Z and A are respectively atomic number and atomic weight of the material crossed, $\alpha \simeq 1/137$ is the fine structure constant, and $(\hbar c)$ is the usual conversion factor ($\sim 197 \times 10^{-13} MeV$).
The physical meaning of χ_c is that on average a particle suffers exactly one single scatter greater than χ_c crossing the target.
Another important parameter is the *screening angle* χ_a:

$$\chi_a^2 = \chi_0^2(1.13 + 3.7\alpha_B^2), \tag{1.23}$$

where:

$$\chi_0^2 = \frac{c_2^2}{(pc)^2}, \tag{1.24}$$

and α_B is the Born parameter defined as:

$$\alpha_B^2 = \frac{c_3}{\beta^2}. \tag{1.25}$$

The constants c_2 and c_3 are:

$$c_2 = \left[\frac{1}{0.885}\left(\frac{e^2}{\hbar c}\right)(m_e c^2) Z^{1/3}\right]^2 \tag{1.26}$$

$$c_3 = \left[\left(\frac{e^2}{\hbar c}\right) zZ\right]^2 \tag{1.27}$$

The screening angle represents the value at which the single scattering cross-section stabilizes because of the screening effect of atomic electrons of the nuclear charge.
The *reduced target thickness* B is described by the equation:

$$B - lnB = b \tag{1.28}$$

and can be solved by standard numerical algorithms knowing that:

$$b = ln\left(\frac{\chi_c^2}{1.167\chi_a^2}\right). \tag{1.29}$$

So, B is proportional to the natural logarithm of the normalized target thickness, and the proportionality coefficient depends on the material.
Finally, the Molière's characteristic multiple scattering angle is defined by the following equation:

$$\theta_M = \frac{1}{\sqrt{2}}(\chi_c\sqrt{B}), \tag{1.30}$$

defining a reduced angle:

$$\theta' = \frac{\theta}{\chi_c\sqrt{B}}. \tag{1.31}$$

Molière approximated the theta distribution function $f(\theta)$ as:

$$f(\theta) = \frac{1}{2\pi\theta_M^2}\frac{1}{2}\left[f^{(0)}(\theta') + \frac{f^{(1)}(\theta')}{B} + \frac{f^{(2)}(\theta')}{B^2}\right], \tag{1.32}$$

where:

$$f^{(n)}(\theta') = \frac{1}{n!}\int_o^\infty ydyJ_0(\theta' y)e^{y^2/4}\left(\frac{y^2}{4}ln\frac{y^2}{4}\right)^n, \tag{1.33}$$

while $f^{(0)}$ is a Gaussian:

$$f^{(0)}(\theta') = 2e^{-\theta^2}. \tag{1.34}$$

The foregoing equations, with Bethe's improved tables for $f^{(1)}(\theta')$ and $f^{(2)}(\theta')$ [9] allow to compute the distribution function $f(\theta)$ for a thin layer of material composed by a single element with atomic number $Z \gg 1$ and with small energy loss for the incident particle.
To generalize to the low-Z elements two different approaches have been followed in literature. The first one is due to Bethe and it is a simple substitution of the Z^2 term in the Molière function with the term $(Z(Z+1))$.
The second method has been developed by *Fano* [10]. It gives a correction of the factor b and it is more complicated with respect to the Bethe approach.

Single Gaussian approximation

This is the simplest approach and describes the central part of the distribution. It is derived from the first approximation of the Molière formula (Eq. 1.32) and it is a Gaussian distribution with zero mean:

$$f_G(\theta) = \frac{1}{\sqrt{2\pi}\theta_0}exp\left[-\frac{1}{2}\frac{\theta^2}{\theta_0^2}\right]. \tag{1.35}$$

The width of the distribution is computed using Highland's formula [11]:

$$\theta_0 = \frac{14.1\text{MeV}}{pv}z\sqrt{\frac{L}{L_R}}\left[1+\frac{1}{9}log\left(\frac{L}{L_R}\right)\right]\text{rad}, \tag{1.36}$$

where p, v and z are the momentum, velocity and charge of the particle, L and L_R are the thickness and the radiation length of the material. θ_0 is the planar angle, it is small enough to be considered analogous to the angle of Molièr θ_M.

Double Gaussian approximation

A slight improvement can be obtained by adding a second Gaussian distribution with a larger width to the core Gaussian:

$$f_{2G}(\theta) = \frac{1-w}{\sqrt{2\pi}\sigma_1}exp\left[-\frac{1}{2}\frac{\theta^2}{\sigma_1^2}\right] + \frac{w}{\sqrt{2\pi}\sigma_2}exp\left[-\frac{1}{2}\frac{\theta^2}{\sigma_2^2}\right], \tag{1.37}$$

with $\sigma_1 < \sigma_2$ and $w \ll 1$. The central width σ_1 is very close to θ_0.

Gauss–Rutherford approximation

The correction to the central Gaussian is here represented by a Rutherford-like distribution with wider tails:

$$f_{GR}(\theta) = \frac{1-w}{\sqrt{2\pi}\sigma_1}exp\left[-\frac{1}{2}\frac{\theta^2}{\sigma_1^2}\right] + \frac{wa}{(\theta+b)^c}, \tag{1.38}$$

with $c \simeq 2.0$. The parameters of the distributions depend on the step length, material and particle energy.

1.1.5 Nuclear Reaction

With respect to electromagnetic interactions in the collision with atomic electrons, the interactions between the projectile nucleus and the target nucleus, nuclear reactions, are much less frequent. However, their effects are significant, especially at large penetration depths. The collision can be elastic or non-elastic.
In the first one, the target nucleus is mildly excited, both this effect can be neglected for the purpose of this thesis. The primary incident particles are scattered at a small angle. An example of an elastic nuclear reaction is:

$$^{12}C +^{16} O \rightarrow^{12} C +^{16} O \tag{1.39}$$

where the particles involved in the reaction does not change their nature.
In a non-elastic collision, when a projectile hits a nucleus, prompt light particles are emitted and the excited nucleus can break-up producing secondary particles. Except for proton beams, both projectile and target nucleus can break-up. A non-elastic reaction could be the following:

$$^{12}C +^{16} O \rightarrow^{12} C + p +^{15} N \tag{1.40}$$

where even if ^{15}N nucleus is produced in the ground state, an amount of energy has been used to extract the proton from the nucleus. As a consequence in a non-elastic nuclear reaction the total kinetic energy is not conserved.
A particular case of non-elastic reaction is inelastic nuclear interaction in which the total kinetic energy of the system is not conserved but the target nucleus state does not change. For instance:

$$^{12}C +^{16} O \rightarrow^{12} C +^{16} O^{\star} \tag{1.41}$$

where the symbols * indicates the excited state.

Nuclear Fragmentation

At the energies required for particle therapy applications (few hundreds MeV), the treatment is influenced by nuclear fragmentation. Since the projectile velocity is sufficiently high to penetrate the Coulombian barrier, reactions between nuclei may occur. This reaction can be as destructive as spallation reactions that lead to a complete disintegration of the projectile and target nucleus or can result only in partial fragmentation. Even if quantum chromodynamics (QCD) is the fundamental theory that describes interactions between quarks and gluons inside the nucleus, the nucleon energy of interest in PT could not be successfully applied to make predictions on nucleus-nucleus collisions, due to the high complexity of mathematical calculations. This has led to the development of empirical or semi-empirical effective models based on experimental data.
Many simple parametrisations of nuclear interaction use a geometrical approximation, in which the nuclei are assumed to be simply spheres. Based on the value of the impact parameter with respect to the radius of the interacting particles, it is possible to distinguish in central and peripherals collisions. The first case occurs when the impact parameter is very small and therefore all nucleons, both of the target and the projectile, can participate in the reaction by creating a high multiplicity of fragments that come out over a wide range of angles. As the impact parameter increases, peripheral collisions occur in which the overlap between the projectile region and that of the target is very small, with a consequent incomplete fusion of the nuclei.

As a result, few fragments are observed usually with speeds approximately equal to those of the projectile, directed in the same direction of the beam fragmentation. The cross-section is a function of the energy of the projectile and the type of the projectile and target. While at high energies a partial fusion is more likely, for energies in the region of the Bragg peak the probability of complete fusion reaches values of about 40-50% depending on the mass of the projectile.

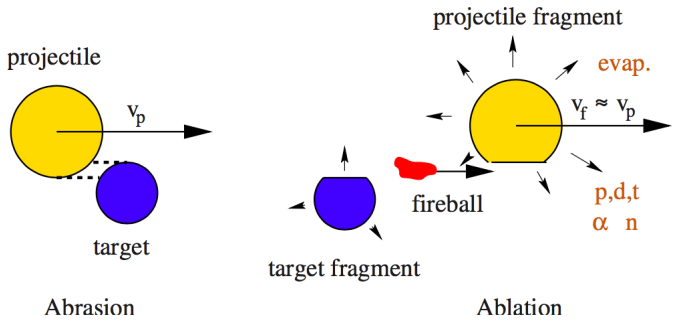

Figure 1.5. Abrasion-ablation model for peripherical collisions at high energies [12].

Peripheral collisions occur in two passages with different time scales (abrasion-ablation model [12], Fig. 1.5); First, with characteristic times of the order of 10^{-23} s, the interaction transfers a certain amount of excitation energy to the target nucleus in the overlapping area, while the rest of the nucleus acts as a spectator (Abrasion). At this stage, light particles are emitted. The projectile fragments follow the initial trajectory at the approximately same speed, while the target's recoil fragments move slower. Subsequently, in the ablation phase, the system thermalizes and the remaining fragments of a projectile and target de-energize by evaporation (emitting neutrons, protons and light nuclei) by fission and by emission of gamma rays. The characteristic time of emission of particles varies between 10^{-21} s and 10^{-16} s for excitation energies of 200 MeV and 10 MeV respectively.
Despite nuclear interactions are less frequent than electromagnetic processes, they have great relevance in PT. The main consequences are:

- Primary beam fluence loss. The number of beam primary arriving at a certain depth depends on the number of inelastic collisions that the beam undergoes. For instance, only $\sim 80\%$ of proton hitting a water target at 160 MeV actually stop in the Bragg peak [13]. For Carbon-ions this fraction is generally lower: $\sim 50\%$ of the total primary Carbon ions arrives at Bragg peak when hitting a water phantom at 290 MeV/u [14].

- The dose distributions are modified. In the buildup region of the Bragg curve, where the dose increases before the Bragg peak, secondary particles contribute considerably to the total energy deposition. Moreover, the height of the Bragg peak is modified. In addition, in the case of carbon ion irradiation, the dose is also delivered beyond the Bragg peak, as shown in Fig. 1.6. The tail is due to the lighter fragments emitted with the same velocity that have a longer range with respect to the carbon beam. Also, the lateral dose distribution is modified by fragmentation: the low energetic secondary particles (including neutrons), which are typically emitted at larger angles, contribute to the low dose envelope at large angles around the beam.

- Several secondary particles, that can potentially exit from the patient, are produced. As it will be shown in the Sec. 2.5, such particles can be used to develop beam range monitoring devices.

For a proton beam, only the fragmentation of the target nuclei is presented, i.e. the evaporation of the excited target following the collision with the consequent production of light particles. The speed of these fragments is quite small and therefore their range does not exceed a few microns thus depositing the energy near the point where the collision occurs. In the case of $Z > 1$ instead, the fragmentation of the target has a small contribution and the projectile fragmentation is dominant. Most of the charged fragments produced in the fragmentation of the incident beam have a velocity similar to that of the projectile but smaller in size. Considering that for particles with the same velocity the trend of the range goes as A/Z^2, the fragments ($Z_{framm} < Z_{proj}$) will stop beyond the Bragg peak of the projectile, creating a tail (Fig. 1.6) that is absent in the case of proton beams.

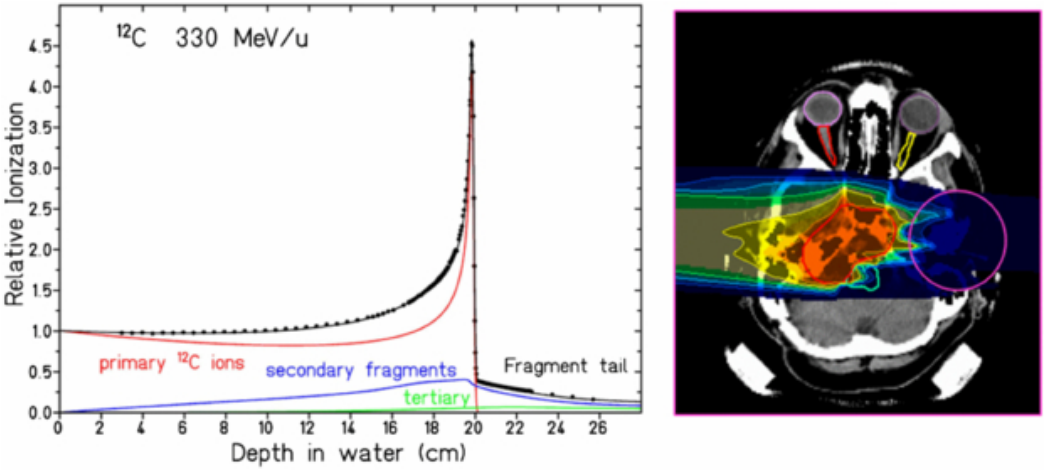

Figure 1.6. Left, in black the Ionization energy release of carbon ion beams of 300 MeV/u in water. In red the contribution of the primary particles is shown. In blue and green the contribution of secondary and tertiary fragments. Right, a typical treatment plan for cancer treatment with ^{12}C ions in the skull base. The colored scale represents the intensity of the dose released (blue for the minimum of the dose and red for the maximum). The small dose beyond the target volume is caused by high-energy nuclear fragments [15].

1.2 Biological parameters

The capability of radiations to induce the tumour cells death and to prevent their reproduction is directly related to the capability to damage the cells DNA. Particles with a charge higher than one induce more severe DNA damages with respect to photons. For this capability, in the following sections, we will refer to protons and carbon ions as a heavy charged particle to distinguish them from photons. This effect, on top of the advantages offered by the peculiar depth-dose profile, makes the PT using carbon ions, for instance, particularly convenient with respect to conventional radiotherapy due to the enhanced biological effectiveness in cell killing. This feature makes PT very attractive for the treatment of radio-resistant local tumours.
In this section, the biological parameters of particle therapy will be described. In

particular, a comparison between conventional radiotherapy, proton and carbon ion beams will be shown.

1.2.1 Dose

One of the relevant quantities in cancer radiation therapy is the absorbed dose. It is defined (ICRU report [16]) as the mean energy deposited by ionizing radiation per unit mass, and it is expressed in gray (1 Gy = 1 J/Kg):

$$D = \frac{dE}{dm} \ [\text{Gy}]. \tag{1.42}$$

Considering a parallel particle beam with fluence F (computed as the ratio between the number of particles dN and the surface crossed dS), it is possible to calculate the dose release inside a thin layer of absorber material with mass density ρ as follows:

$$D[\text{Gy}] = 1.6 \times 10^{-9} \times \frac{dE}{dx}\left[\frac{\text{keV}}{\mu\text{m}}\right] \times F[\text{cm}^{-2}] \times \frac{1}{\rho}, \tag{1.43}$$

where, dE/dx is the linear energy transfer per unit path length that will be described in Sec. 1.2.3.
The goal of radiation therapy is to obtain a perfectly conformal dose distribution, so to concentrate all the dose in the tumor volume and to release zero dose to surrounding healthy tissues.

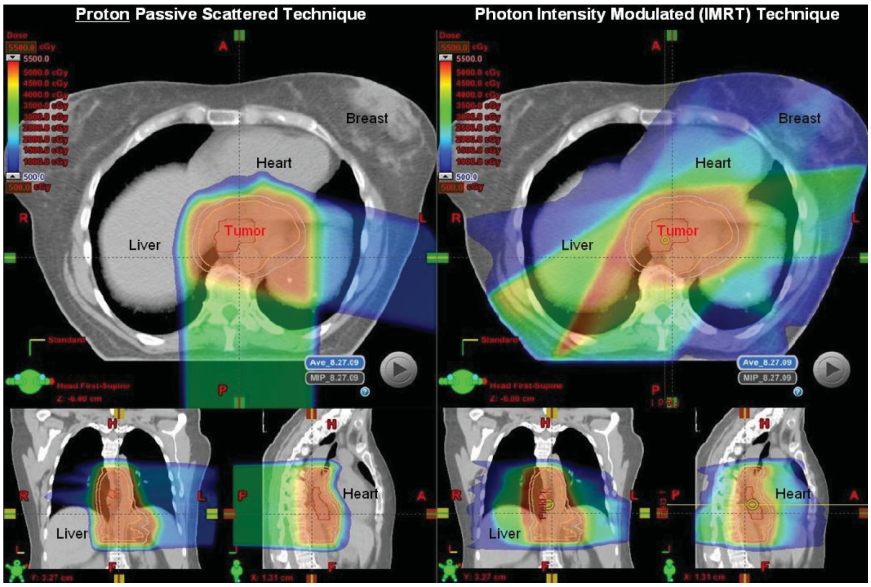

Figure 1.7. Comparison between the treatment plan system (TPS, described in Sec. 2.4) of an IMRT (right) and the TPS of the same tumor using a combination of proton beams. The colorwash scale represents the dose distribution [17].

In standard photon radiotherapy, the conformal dose map is often achieved by modulating the intensity of the radiation beams in multiple small volumes and sending the beams from different directions (called fields, Fig. 1.7). In particle therapy, the selectivity in the energy release of charged particles facilitates the shaping of the dose release.

The beam can scan the tumor volume with tissue compensators interposed between the accelerator's exit window and the patient (*passive scattering*). With this technique, the beam is spread out to be a uniform beam (laterally) through single or double scattering. Most scattering systems can produce a uniform field distribution for maximum field sizes of up to 25 cm diameter. The edges of the beam can then be shaped laterally by collimators to shape the radiation field that impinges on the patient. A spinning range modulator wheel allows for the beam energy to vary with time and the result is that there is a spread in the energies of the primary particle, resulting in a dose distribution that is a spread out Bragg peak. In *active scanning* instead, the tumor is divided into several small volumes, called voxels, and each voxel is irradiated with specific beams with appropriate direction, energy and intensity.
A further consideration is that the relationship between absorbed dose and the biological effect is not simple to evaluate. The same radiations in different tissues show different dose-response relationships. So, the exact computation of the energy deposition is not sufficient to predict the effect of radiation on tissues. In the following sections, the radiobiological aspects will be discussed and the differences between carbon ions and protons' biological effectiveness will be carried out.

1.2.2 Energy deposition

As has been observed in the previous section, the release dose is straightly correlated to the energy deposition. The energy release as a function of the penetration depth of photon and charged particle has different profiles, as reported in Fig. 1.8.

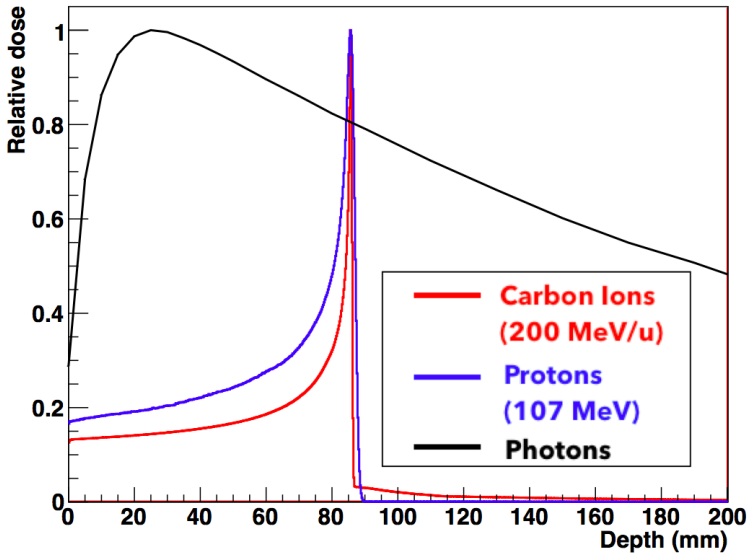

Figure 1.8. Relative dose released during the penetration in water for a beam of photons (black), a beam of 200 MeV/u carbon ion (red) and a beam of 107 MeV/u protons (blue).

The photon energy release shows an increase up to the maximum that occurs after centimetres, followed by an exponential decrease. On the contrary, heavy charged particles have a completely different energy deposition curve. A small amount of energy lost in the entrance channel while a significant amount is released in the Bragg peak, near the end of the particle range. The depth of the Bragg peak is

determined by the material crossed and the particle's initial energy (Fig. 1.9 left). Given the density of the material crossed by the beam, its range inside the patient can be adjusted by changing the beam energy. This peculiar energy deposition could lead to a better conformation to the target volume, with consequent sparing of healthy tissues.

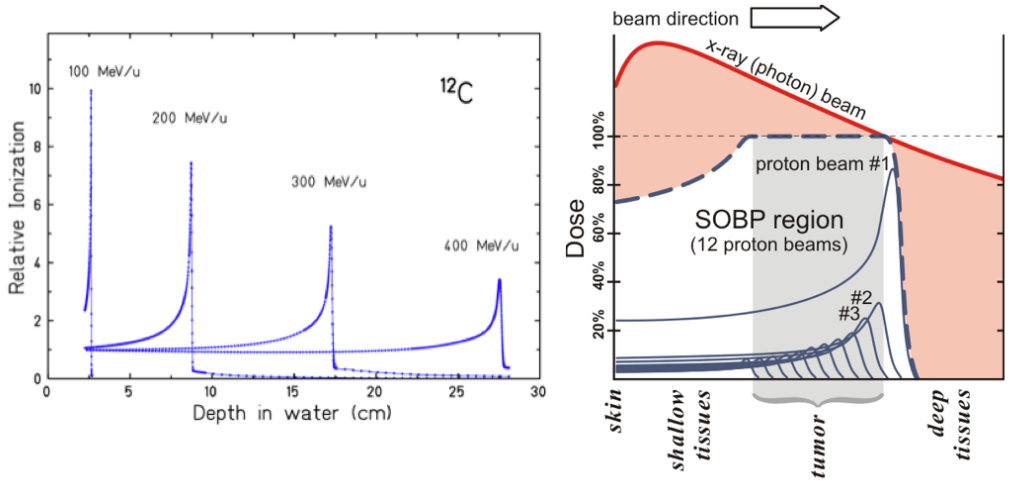

Figure 1.9. Left, the ionization density of a carbon ion on a water target as a function of the penetration depth for different energies is shown. Right, a SOBP, made by the overlapping of 12 Bragg peaks of proton beams at different energies, is represented.

However, the Bragg peak width is too thin to cover the entire tumor volume, so an overlap of beams at different energies is used to obtain a wider profile of dose. The result, shown in Fig. 1.9 (right), is an extended Bragg peak called Spread Out Bragg Peak (SOBP) which cover all the tumor volume. In Fig. 1.10 it is reported a comparison of dose-depth profiles resulting from different radiation therapies. The advantage of particle therapy (both with protons and carbon ions) with respect to conventional radiotherapy can be easily understood by comparing the relative longitudinal dose curves with the ideal goal (Fig. 1.10 a). Ideally, the optimum energy distribution would be concentrated in the tumor volume and completely absent in the surrounding healthy tissues. This is not feasible but there is a huge difference in the behavior of photons, protons and carbon ions. Conventional radiotherapy (Fig. 1.10 b) involves a significant harmful dose release before and beyond the target. This effect can be inefficient especially in presence of near OAR. In proton therapy (Fig. 1.10 c) instead, the dose on a near critical organ can be avoided since after the SOBP there is no release of dose. For what concerns carbon ion therapy (Fig. 1.10 d) an aspect that has to be highlighted is the contribution of nuclear fragments produced by the interaction of carbon ions with target nuclei. This process, that has been discussed in the Sec. 1.1.5, produces a tail in the dose profile beyond the Bragg peak with a consequent overdose delivered to tissues beyond the tumor. However, the dose released by the tail is considerably small compared with the peak. Moreover, this dose distribution has also a better ratio between the peak and the plateau region compared to proton beams. This means that to release the same amount of dose in a region, with carbon ion beams there will be less dose before the peak.

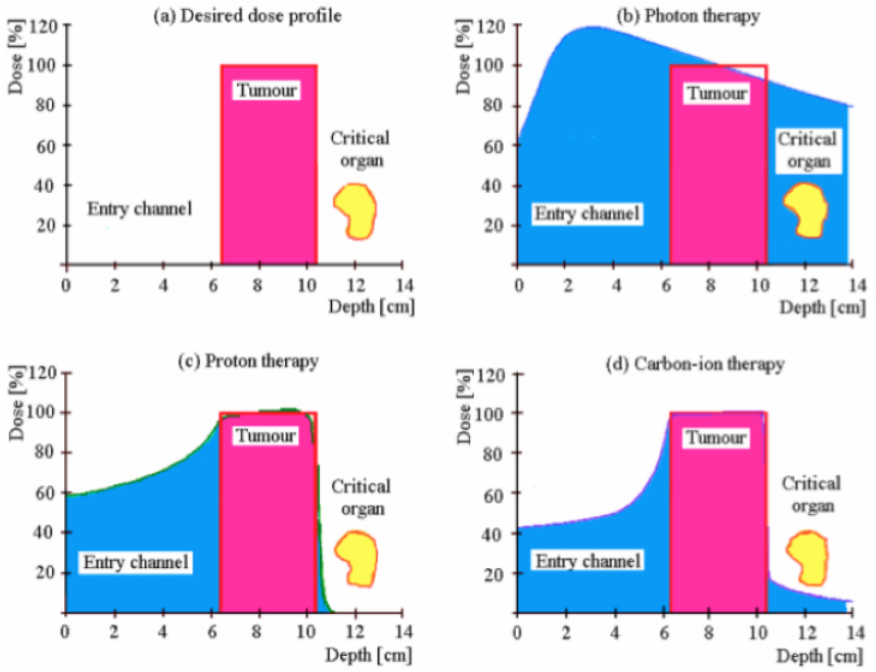

Figure 1.10. Comparison between (a) dose profile desired, (b) conventional radiotherapy with photons, (c) particle therapy with proton beams and (d) particle therapy with carbon ion beams for a given tumour volume (in pink) close to a organ at risk (in yellow).

1.2.3 Linear Energy Transfer

To evaluate the efficiency of ionizing radiation, a further quantity needs to be introduced: the Linear Energy Transfer (LET). It expresses the local energy released and it is defined as the mean energy released per unit path length by an ionizing particle:

$$LET = \frac{\Delta E}{\Delta x} \left[\frac{\text{keV}}{\mu\text{m}}\right]. \tag{1.44}$$

To give the relationship with the stopping power we have to introduce the delta ray production by a charged particle. This process originates from the production of secondary electrons by ionizing atoms of the crossed material. If the energy of secondary electrons is large enough to induce further ionizations they are called delta rays. When it is important to focus on the energy transferred only in the proximity of the primary particle track, a threshold energy Δ of secondaries is established and only the contribution of secondary electrons with energy less than Δ is taken into account. The resulting quantities are called restricted linear energy transfer:

$$LET_\Delta = \left(\frac{\Delta E}{\Delta x}\right)_\Delta \left[\frac{\text{keV}}{\mu\text{m}}\right]. \tag{1.45}$$

In the limit of $\Delta \to \infty$, the LET becomes unrestricted and it is equal to the electronic component of the stopping power (described in Sec. 1.1.1).

1.2.4 Biological effect of ionizing radiation

The biological damage caused to cells by radiation concerns in particular the DNA which contains the genetic instructions used for the growth, development, functioning and reproduction of cells. The cell diameter is 10 - 100 μm while the two helices that make up the DNA are $\sim$ 2 nm apart and are contained in the chromatin of the nucleus whose diameter is $\sim$ 3 μm.
In Fig. 1.11, it is possible to see an example of DNA breakdown by a beam of photons and ions: when radiation passes through the patient's body, it ionizes cells, both healthy and cancer. The electrons produced can directly hit the DNA of the cell (*direct interaction* with DNA), creating more substantial damage, or in turn, ionizing the water. Ionizing the water, which makes up 80% of the human body, free radicals (OH, O) are produced. These radicals are chemically very reactive and, although they have a very short life, they can reach the nuclei of cells and damage DNA (*indirect interaction* with DNA).

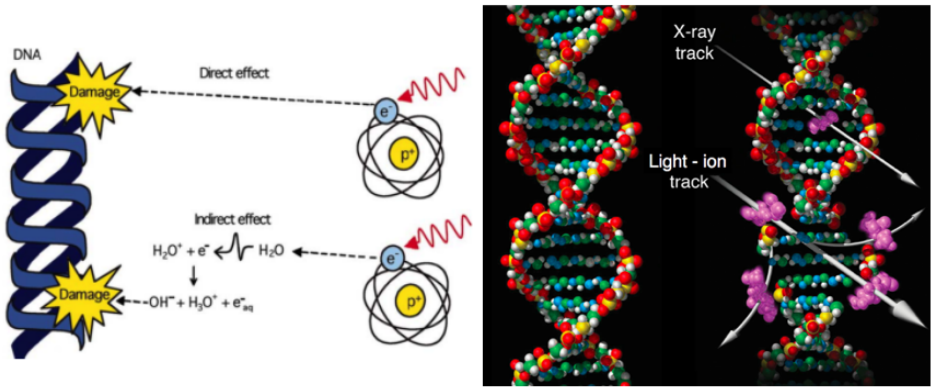

Figure 1.11. Left, a DNA's helix broken by the direct action of an ionized electron created by the passage of a gamma rays e from the action of free radical OH induced by ionizing radiation of a photon. Right, an example of the difference between damage caused on a helix of DNA by photon beams and ions.

Cells have an extremely elaborate repair system and can repair simple damages. The fraction of irreparable damage depends on the LET of the incident beam and the relative biological effectiveness. The lesions induced to the DNA, directly or indirectly, are classified into two different types: single-strand break (SSBs) and double-strand break (DSBs). The first one consists of one single break and it is typical of low-LET radiations. It is easily repaired by the cell which can use the safe strand as a template to recover the break. The double-strand break consists of two or more breaks occurring in both strands. It is considered the most important lesion produced in chromosomes by radiation: the interaction of two DSBs may result in cell killing, carcinogenesis, or mutation. This kind of lesion is predominant in high-LET radiations.

1.2.5 Ionization density

The ionization density is closely related to the LET and to the pattern of energy release. It is defined as the number of ions per unit path length produced by radiation crossing a material.
The differences between photons, protons and carbon ions ionization density are

shown in Fig. 1.12. Protons and photons have a sparse ionization density and so are called low-LET radiation, while carbon ions are high-LET particles due to their larger ionization density. This means that the amount of energy released for unit path length by photons and protons is smaller than heavier ions. On the other hand, it has to be considered that, while photons are sparsely ionizing during all their path, protons can reach high LET values at the end of their range in tissues (in the proximity of the BP).
In the range of beam energies for the standard radiotherapy, the mean distance between two ionization event is d $\sim$ 200 nm, while, for carbon ions, it can vary from d $\sim$ 4 nm at the entry channel up to d $\sim$ 0.3 nm at the level of the Bragg peak. If we consider that the DNA helix has a mean dimension of $\sim$ 2 nm we can conclude how carbons and high-LET radiations have a higher Double-Strand Break probability with respect to photons, and this leads to higher damage capability.

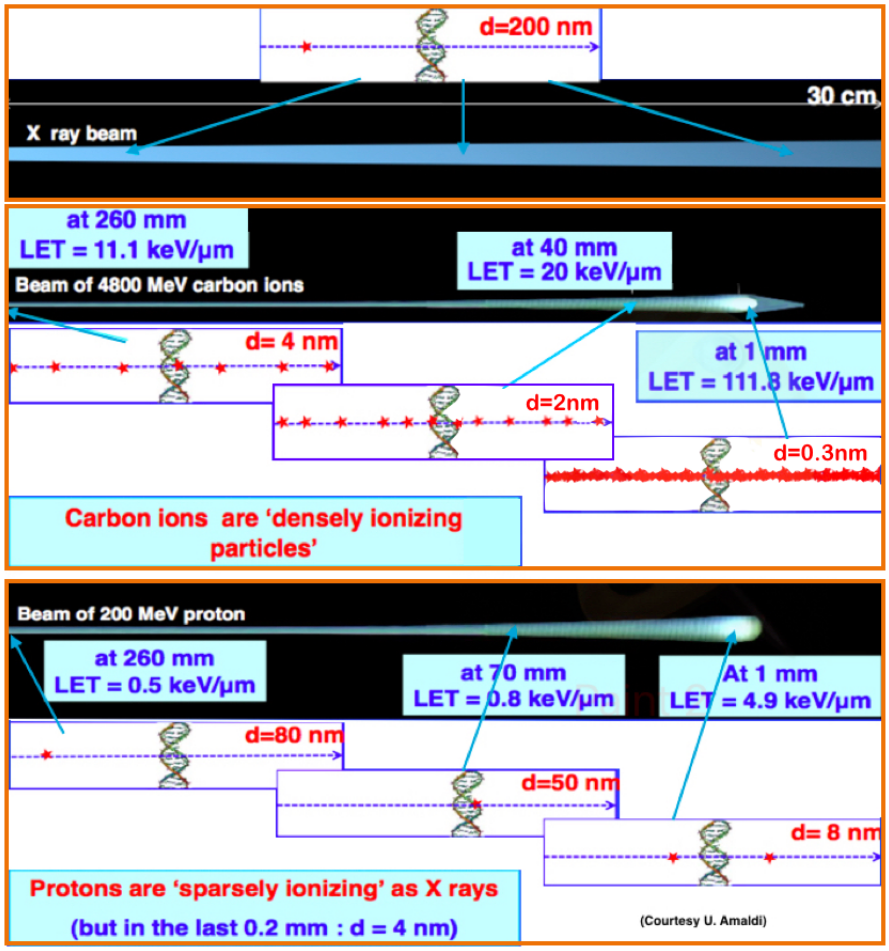

Figure 1.12. Comparison of the LET obtained with X-ray beams (on the top), carbon io beams (in the center) and proton beams (in the bottom); d is the mean distance between two ionizations.

1.2.6 Lateral beam spread

When a charged particle crosses material it suffers from elastic Coulomb interactions with target nuclei and atomic electrons. Because of such interactions, the direction of the particle changes with respect to the original direction. The macroscopic result of multiple Coulomb scattering (Sec. 1.1.4) is the beam spread in the plane perpendicular to its direction.
The extent of the lateral spread is related to the target material density and the primary particle mass. Higher density material induces more scattering events, with a consequent larger lateral spread of the lateral beam. On the contrary, heavier particles will suffer smaller deviation with respect to their original direction in comparison to lighter particles.

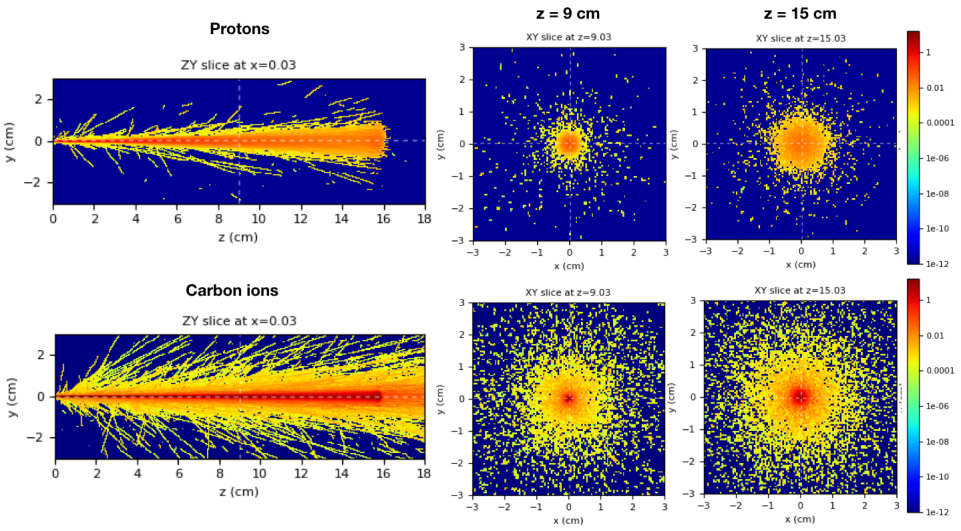

Figure 1.13. The energy release in the water of a 150 MeV proton beam and on a 285 MeV/u carbon beam is shown respectively on the top and the bottom. On the left, the longitudinal map can be observed, on the right transverse beam spots at 9 cm depth and 15 cm depth are represented. The maps have been obtained with FLUKA Monte Carlo software and for both the distributions the beam size is with a FWHM of 0.5 cm.

In Fig. 1.13, an example of a proton and a carbon beam with the same range, with energy 150 MeV and 285 MeV/u respectively, both crossing a water volume is shown. It is possible to observe how carbon beam shows a lateral spread smaller than protons.
The lateral spread out of the beam due to multiple scattering forces to carefully consider any materials interposed between the accelerator ejector and the patient, such as the beam pipe exit window, external beam monitors, collimators, compensators, air and so on. This contribution is more evident at low energies (considering the typical travelling distance of 0.5-1.0 m) since the path of the beam in the patient body is shorter and the spread due to the tissues crossed is lower. On the other hand, at high energies the penetration depth inside the patient increases and the lateral spread due to the interaction with tissues is predominant.
In Fig. 1.14 computed lateral spread of carbons and protons from standard treatment to the beamline is shown. For the aforementioned reasons, and in particular for protons, the amount of material along the beam path in front of the patient should be minimized.

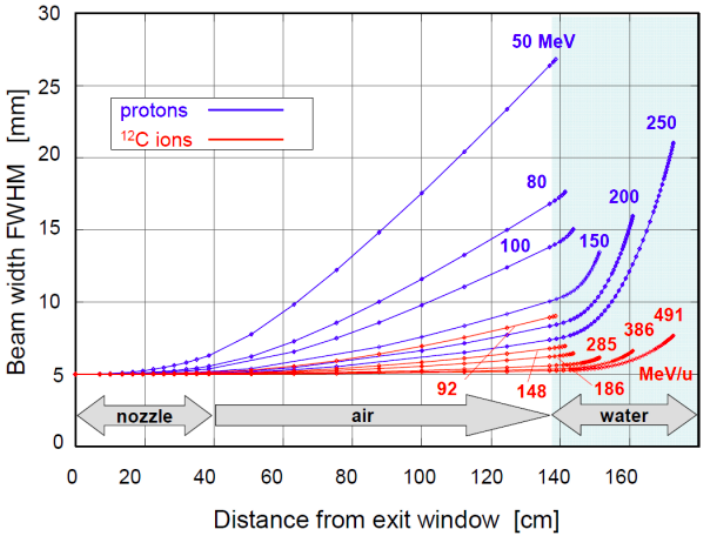

Figure 1.14. Calculated beam spread for ^{12}C ions and protons in a typical treatment beamline. It was assumed that an initially parallel particle beam (5 mm full width at half maximum) passes through the nozzle (including a thin vacuum window and beam monitors) and enters a water absorber (patient) at 1 m distance from the nozzle exit. At small depth (i.e., small particle energies) the width is mainly determined by scattering in the nozzle, while at higher energies the scattering in the water absorber dominates. Carbon ions show a much smaller spread than protons at the same penetration depth [7].

1.2.7 RBE

A very important aspect that has to be taken into account in radiation therapy of cancer is the fact that a given amount of dose has effects on the cell, which depends on the radiation features and the biological tissue irradiated. To quantify the effectiveness of charged particles in cells killing a parameter called Relative Biological Effectiveness (RBE) has been introduced. It is defined as the ratio of the dose of reference radiation (D_x, typically γ-rays or x-rays) to the dose of the radiation needed to produce the same biological effect D_i, that means with the same cell survival rate:

$$RBE = \frac{D_x}{D_i}. \tag{1.46}$$

In proton therapy treatment the RBE value is often considered fixed at RBE = 1.1 [18]. For carbons, this assumption is not valid and an appropriate model has to be used in the calculation of the treatment plan and the relative biological effect.
Survival curves are often used to evaluate the biological effect. They represent the percentage of survival cells in the function of the dose absorbed after irradiation. For a fixed survival fraction the RBE can be graphically computed by the ratio of the two respective doses. In Fig. 1.15 is shown an example of cell survival curves relative to a photon irradiation and heavy ions (such as carbons) irradiation. With survival cells, we mean the cells that maintain their reproductive integrity. The curves are often represented with a linear scale on the x-axis (dose), and a logarithmic scale on

the y-axis (survival fraction).
Radiations with high ionization density show an exponential cell survival trend that in the semi-log representation translates into a straight line curve. On the contrary, a low ionization density radiations curve has an initial slope followed by a shoulder and then at high dose values, the shape is almost straight. The most used model for the cell survival function S is the linear-quadratic [19]:

$$S(D) = \frac{N_{survival}}{N_{seed}} = e^{-(\alpha D + \beta D^2)} \tag{1.47}$$

where D is the absorbed dose and α and β are two experimental parameters that define the lethal and sublethal damage respectively.
The ratio α/β defines the shoulder of the curve and it is a very important parameter in standard radiotherapy.
The RBE is the most important quantity in biological treatment planning in particle therapy since it determines the photon-equivalent dose, also referred to as RBE-weighted dose. It is conveniently used to compare the results of conventional radiation with other radiations such as neutrons, protons, or carbon ions. The RBE can be used for many biological effects such as DNA strand breaks, mutations, or transformations. In the scope of heavy-ion therapy, however, the RBE for cell killing and normal-tissue complications are most relevant.
Furthermore, because the LET of light ions is higher at lower energy, it means that at the entrance channel of the beam the RBE will be lower (because the energy is high) and in the proximity of the BP, it increases.

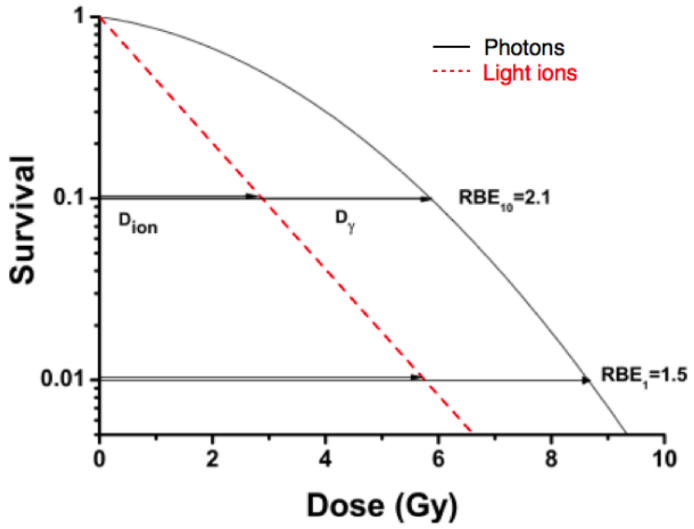

Figure 1.15. Survival curves for a typical photon (black and solid line) and heavy ions radiation (red and dashed line). The determination of the RBE is shown for two different survival level (1% and 10%) [7].

1.2.8 OER

The presence of oxygen in cellular tissue can increase the effect of radiation through stabilizing and making less repairable the radicals induced damage. Cells irradiated with low LET radiation in the presence of oxygen are more sensitive

than the same cells irradiated under conditions of hypoxia (Fig. 1.16) [20]. The parameter that was introduced to describe this strengthening is the OER (Oxygen Enhancement Ratio) defined as:

$$OER = \frac{D_{pO_2}}{D_O} \tag{1.48}$$

where D_{pO2} is the dose in hypoxic condition, at a given oxygenation level pO_2, D_O is the dose in normal oxygen supply condition.
Typical values of OER are between 1 (if the damage produced by the radiation is independent of the presence of the oxygen) and 3 (if the damage is straightly dependent on the oxygen).
The effect becomes negligible if high LET radiation is used. For radiation of the highest LET components of highly charged hadrons (namely carbon and oxygen [21]), cellular inactivation is less mediated by hydrogen and hydroxyl radicals but is directly due to the ionization produced. For this reason, radiation of charged hadrons is the most effective for the treatment of poorly oxygenated tumors.

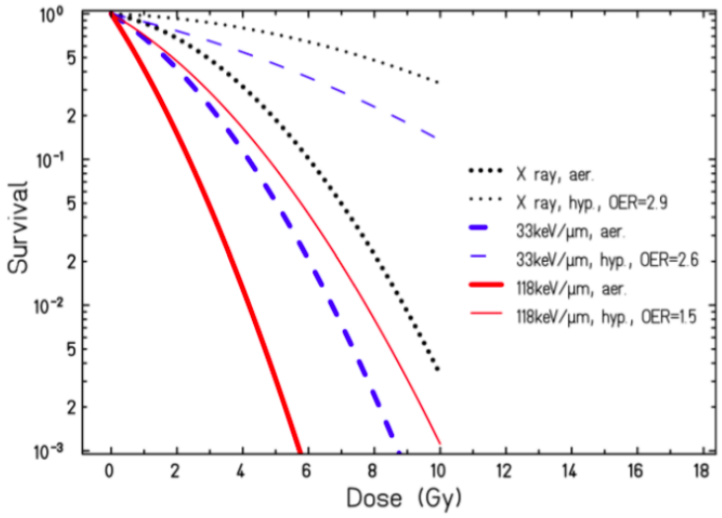

Figure 1.16. Survival curve of human kidney cells as a function of the dose of irradiated cells in the presence of oxygen (thicker line) and conditions of severe hypoxia (thinner line) for different energies and therefore different LET. The influence of the oxygen level for carbon ions at 33 keV/μm is represented in blue, at 118 keV/μm in red. In black, however, it is possible to observe the variation for X-rays [22].

Chapter 2

Accelerators for Particle Therapy

Charged particle beams are provided by particle accelerators. The most used accelerators technologies in particle therapy centers are cyclotrons and synchrotrons. Today in the world there are 106 facilities in operation, 14 of which use carbon ion beams and 92 proton beams [23]. Other 41 are under development (35 of proton beams, 6 of carbon ion beams) [24] and they will be in operation in the next few years. Despite the favourable dose release of protons and ^{12}C ions with respect to standard photon beams, particle therapy is still a small fraction of external radiotherapy. This is due mainly to space and cost motivations. In particular, particle therapy machine only recently, and for proton beam only, reached a dimension such that can be reasonably hosted in a pre-existing clinical structure. The high number of proton beam facilities compared to carbon ion is because, while protons can be accelerated with cyclotrons, it is necessary to use a synchrotron to create a carbon ion beam at the energy of interest for particle therapy (50-450 MeV/u). As explained later on, a synchrotron needs a large infrastructure dedicated to being built and operated.

Table 2.1. Typical clinical requirements for particle therapy using carbon ions or protons [25].

Parameter	**Value**
Extraction energy (**proton**) (min,max)	60,240 MeV
Extraction energy (**carbon**) (min,max)	110, 450 MeV/u
Energy step (**proton**) (at min, at max)	5, 1 MeV
Energy step (**carbon**)(at min, at max)	15, 6 MeV/u
Energy resolution (at min, at max)ΔE/E	3.5%,1.8%
Voxel size (min, max)	$4 \times 4 \times 4, 10 \times 10 \times 10$ mm^3
Smallest field of view (min, max)	$100 \times 100, 250 \times 250$ mm^2
Clinical dose rate (min, max)	2, $>$ 10 Gy/min
Cycle rate (min, max)	0.5, 2 kHz
Bunch charge (**proton**) (min, max)	1.6, 16 fC
Bunch charge (**carbon**) (min, max)	300, 3000 fC
Bunch charge stability and bunch charge measurement accuracy	$<$10%

In Tab. 2.1 typical clinical accelerator requirements in particle therapy are shown. The basic principles of accelerators and the characteristics of the machines used in particle therapy facilities will be described.

2.1 Basic concepts

In most particle accelerators, an electric field is used to accelerate the charged particles, while a magnetic field is applied to change the direction of the particles and in this way to guide them through the accelerating structure. In the following, we will need some details of the Lorentz force to treat the features of the machines used in PT.
The motion of the particle, with velocity v and in a magnetic field, is driven by the Lorentz force :

$$\vec{F_L} = q(\vec{v} \times \vec{B}), \tag{2.1}$$

where $\vec{B}$ is the magnetic induction fields.
$\vec{F_L}$ provides the centripetal acceleration necessary to keep the particle moving in a circle in the plane perpendicular to the magnetic field. If the velocity is perpendicular to the $\vec{B}$ field, it is possible to express F_L as a centripetal force:

$$F_L = \frac{mv^2}{r}, \tag{2.2}$$

where r is the radius of curvature. Thus, using Eq. 2.1 and Eq. 2.2, one obtains:

$$\frac{qB}{m} = \frac{v}{r} = \omega_c, \tag{2.3}$$

where ω_c is the angular velocity. The frequency (f_c) at which the particle completes a circular path is:

$$f_c = \frac{\omega_c}{2\pi} = \frac{v}{2\pi r} = \frac{Bq}{2\pi m}. \tag{2.4}$$

Using this information it is possible to write:

$$B_r = \frac{mv}{q} = \frac{p}{q}, \tag{2.5}$$

where p is the momentum and B_r is known as the magnetic rigidity. It is a measure of the reluctance of the particle to be bent in a curve in the presence of a magnetic field. A much greater magnetic field will be required to keep a carbon ion (≈ 12 times the mass of a proton) in the same orbit as a proton of the same velocity.
This analysis is correct when the velocity of the particle is small relative to the velocity of light c. When the velocity approaches c, the effects of special relativity need to be taken into account. For example, a proton accelerated to 250 MeV (the energy needed to cross the human body) will move with a velocity of approximately 60% of light velocity. To take into account the relativistic effects, it is necessary to write the momentum by its relativistic equivalent:

$$p = \beta\gamma mc, \tag{2.6}$$

and so:

$$B_r = \frac{p}{v} = \frac{\beta\gamma mc}{q}, \tag{2.7}$$

where $\beta = v/c$ and $\gamma = (1 - \beta^2)^{-1/2}$.

2.2 Accelerators

Particle accelerators are machines that use electromagnetic fields to increase the kinetic energy of charged particles. Their acceleration processes are based on the Lorentz force caused by the presence of an electric field. Since an electric field can be either electrostatic or dynamic, most accelerators today work with time-varying fields and in particular using resonant cavities and electric fields oscillating at radiofrequency (RF).
Due to electrical breakdown effects, potential gradients in electric fields are usually limited to a few MV/mm [26]. Therefore, to reach higher energies, particle accelerators consist of a series of multiple accelerating elements traversed once (*single-pass scheme*) by the beam, or of a closed-loop arrangement of a few accelerating elements traversed many times (*multi-pass scheme*). The first, linear accelerators, usually are used to accelerate X-ray or electrons and will not be described in this thesis. The latter, cyclotrons and synchrotrons, are used to accelerate protons and carbon ions. They generally allow more efficient use of the accelerating elements but raise the issues of beam injection, cycling and extraction [27].
For medical applications, an accelerator should yield a stable and preferably continuous beam at maximal energies of about 250 MeV for protons and 450 MeV/u in the case of carbon ions. Moreover, other aspects to be considered are the reduction of the size, weight and price of the accelerators, especially regarding the development of affordable single-room facilities. Furthermore, studies are under development for the reduction of treatment times through higher beam currents and faster switching between beam energies [28][29].
The characteristics of cyclotrons and synchrotrons used in particle therapy will be described in this section.

2.2.1 Cyclotrons

A cyclotron is a large circular magnet providing a constant magnetic field across the gap between the pole-faces (Fig. 2.1).
A particle is injected into the magnetic field with an initial velocity, near the centre of the magnet, inside two "dee" (D) shaped hollow electrodes, which are placed between the poles of the magnet. While the particle is inside the D, it is shielded from the electric field. In this way, only the magnetic force applies and the particle moves along a circular path. A potential difference is established between the two Ds, so that each time the particle crosses from one D to the other, it sees a small accelerating voltage and moves outwards, following a new orbit at a slightly larger radius. During the time that the particle is inside the D, the polarity of the voltage is changed, so that it is continually accelerated. The frequency with which the accelerating voltage must be changed is the frequency defined in Eq. 2.4 (called cyclotron frequency). Eventually, the radius will reach a maximum value, determined by the radius of the magnet pole faces, and the particle will escape.
This description ignores relativistic effects, which become significant when the proton kinetic energy is larger than approximately 15 MeV [25]. To reach higher energies, it is necessary either to modify the magnetic field as a function of the radius or to vary the accelerating radio-frequency.
The main limitation of the cyclotron is that as the energy increases so does the size of the magnet. Moreover, relativistic effects mean that the magnetic field has to increase even faster. If one would like to use a cyclotron to accelerate carbon ion up to the maximum energy used to particle therapy (400 MeV/u), the diameter of the Ds would be too large and the accelerator too expensive and massive.

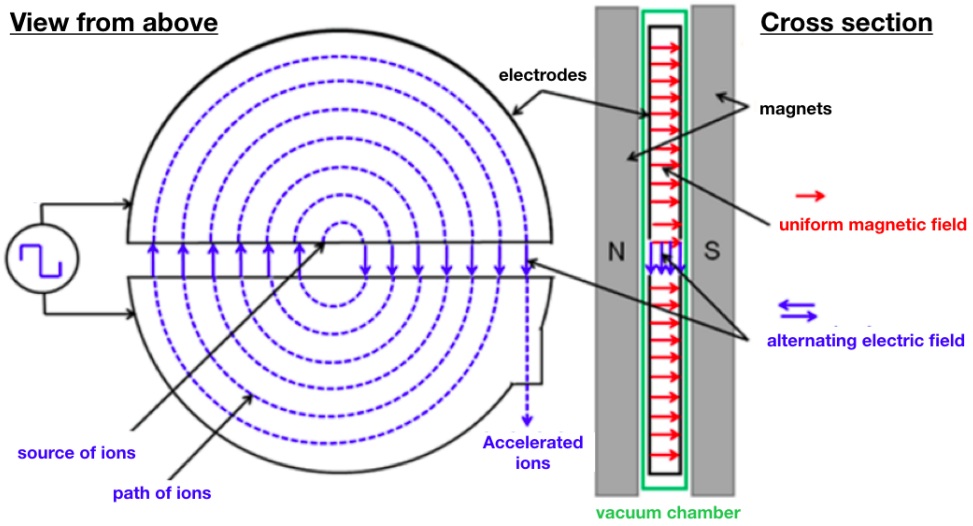

Figure 2.1. Schematic diagram of a cyclotron observing it in the view from above (left) and in the cross-section.

2.2.2 Synchrotrons

Synchrotrons are circular machine with a fixed particle orbital radius. According to Eq. 2.3, to have a fixed radius, the magnetic field must vary as the particles accelerate. At very high energies, when the velocity is close to the speed of light, the RF is constant. Whereas at energies needed for proton and ion therapy, the RF must vary, in synchronisation with the energy and the magnetic fields. This technique is complicated but the advantage is that the magnets and the RF cavities are much smaller and therefore cheaper. Moreover, the limit of the maximum particle energy achievable is higher with respect to cyclotrons, mainly due to the limit of accelerating gradient achievable.
In Fig. 2.2, an example of a layout of a synchrotron is shown. Generally, a linear accelerator is used to pre-accelerate the ion (typically to a few MeV), which is then injected into the synchrotron ring. When the ion transits through the RF cavity, it is accelerated, acquiring energy and increasing velocity. The magnetic field of the bending magnet needs to be increased to match this increase in velocity to keep particles in a fixed orbit. Therefore, unlike the cyclotron where the particle spirals outward with increasing energy under the action of the constant magnetic field, the synchrotron accelerates the particle at a constant trajectory even when the particle energy increases. The guide field can be provided by a narrow ring of magnets. Dipole magnets are used to bend the beam to follow the circular orbit.
Not all the particles have exactly the right energy, position and direction to follow the desired orbit. Although the bending magnets have a weak focusing effect in the horizontal plane, the real advance came with the technique of strong focusing. In strong focusing, quadrupole magnets (a magnet consisting of four poles) spaced around the ring between the bending magnets continually focus and defocus the beam.

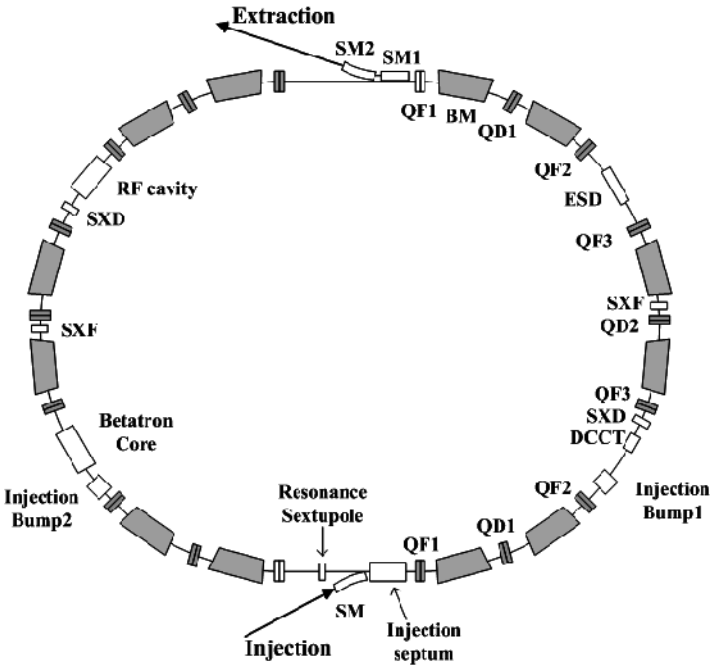

Figure 2.2. Schematic diagram of a synchrotron. QF is the horizontally focusing quadrupole, QD us the horizzontally defocusing quadrupole, SX is the sextupole and BM is the bending dipole [30].

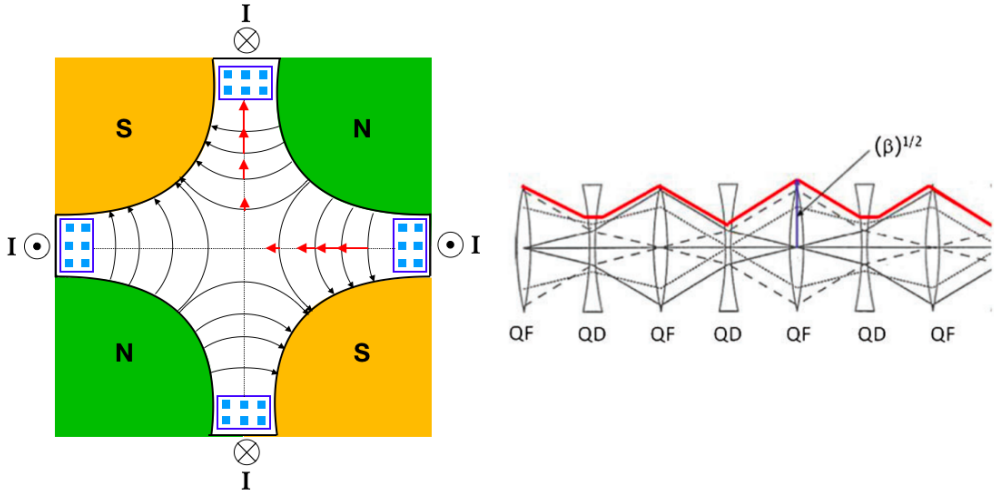

Figure 2.3. Left, magnetic force lines owing to a focusing dipole magnet which focuses the particle in the horizontal plane while defocuses in the other plane. Right, alternative focusing and defocusing quadruple represented using a lens analogy. The net effect is focusing in both directions. QD is the horizontally defocusing quadrupole and QF is the horizontally focusing quadrupole.

As it is possible to observe in Fig. 2.3, this happens because quadrupoles have an odd behaviour, compared with optical lenses, which focuses on both planes, horizontally and vertically. However, if a quadrupole focuses on one plane (for example the horizontal plane), it defocuses in the other (vertical) plane. It can easily

be shown that the combination of two lenses of equal strength, one focusing and one defocusing, has a net focusing effect. By constantly focusing and defocusing around the ring, it is possible to keep the transverse size of the particle bunch small, leading to a small aperture and therefore cheaper magnets.
Each particle is constantly changing its position and angle, with respect to the ideal orbit, describing an ellipse in the horizontal and vertical planes. This is called the phase space. The area swept by the ensemble of particles in the two transverse phase space planes is called the emittance (ϵ), and it is a fundamentally important parameter of the accelerator. The particle motions around the ideal orbit are called betatron oscillations, and the main characteristic is described by the β-function, which varies around the circumference of the machine. At any point, the physical size of the beam in the horizontal (vertical) plane is given by $\sqrt{\beta_{x(y)}\epsilon_{x(y)}}$.
The discussion above assumes that the main components' magnets are perfectly constructed. However, real magnets of finite length always have higher multipole components and there is also dispersion in the magnets owing to the finite distribution of momenta. These can be partially compensated by including higher-order multipole magnets (for example sextupole with six pole faces) in the design.

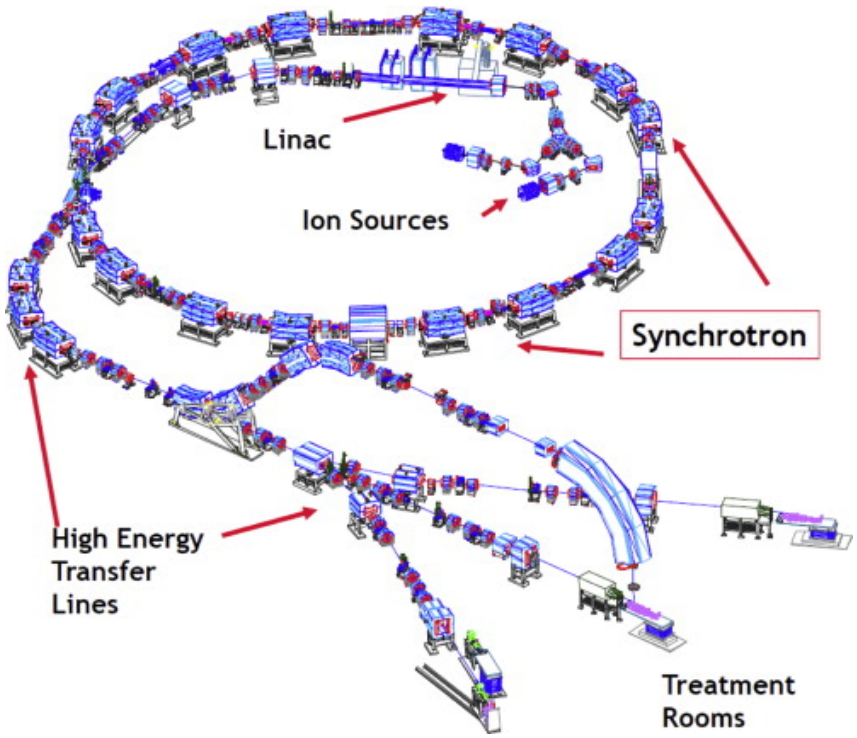

Figure 2.4. Schematic diagram of the CNAO synchrotron [31].

When the beam reaches the desired energy, it must be extracted into an external beam-line and transported to where it is needed. One method uses kicker and septum magnets. A kicker magnet, which has a very fast rise time, is used to divert the entire beam to the transport line, where a septum is a magnetic (or sometimes electrostatic) device for deflecting a beam, or part of it, from its normal path. It can be used to split the ion beam into two beams so that one of the beams can be extracted while the other beam stays in orbit. Other extraction mechanisms can be

used, such as the RF driven extraction, where the betatron oscillations are enhanced, sending the beam into the septum.
In Fig. 2.4, an example of the layout of the CNAO (*Centro Nazionale di Adroterapia Oncologica* sited in Pavia, Italy) synchrotron and its main components are shown. This is one of the few worldwide synchrotrons in particle therapy centers using both protons and carbon ions to treat tumors. A peculiarity of this layout is the injection LINAC (LINear ACcelerator) positioned inside the ring to save space. In this specific case, the LINAC boosts the particle energy from 0.04 MeV/u up to 7 MeV/u. In the figure, it is possible to observe also the extraction line which is connected to transfer lines to transport the beam to three different treatment rooms.

2.2.3 Comparison between Cyclotrons and Synchrotrons

The main advantages of cyclotrons with respect to synchrotrons is the facility of generation and of installation (because of the compact size) and the reliability. Furthermore, cyclotrons deliver continuous and high intensity beam. Their major drawback is the constant energy output. To obtain the required energy distribution, an Energy Selection System (ESS) outside of the accelerator is needed. Such systems typically use an adjustable degrader that scatters and attenuates the beam. The degrader is usually made from graphite and consists of several wedges that can move in and out of the beam path. Alternatively, it can be designed as a rotating wheel of blocks of different thickness. While degrading the beam can lower the beam energy, it also significantly increases the energy spread. The desired energy must therefore be filtered out using a combination of a deflecting dipole magnet and a movable slit collimator. The ESS starts with the highest energy and treats the most distant layer of the tumour first. Then the energy of the beam is lowered and the closer layers of the tumour are treated. The process continues until the whole tumour is painted. A disadvantage of cyclotrons is the fact that up to now they only produce proton beams. With the progress of superconducting magnets technologies that make machines very compact the possibility of a carbon cyclotron for medical use is open.
The most important advantage of synchrotrons is the possibility to deliver beam with variable energy and so other processes are not necessary. At the present, they are the only type of accelerators that can provide heavier ions beams for cancer treatment purposes. These better performances are paid with greater costs with respect to cyclotrons, than the bigger dimension and the complexity of the machine system. Moreover, synchrotrons deliver lower beam current than cyclotrons, with consequent longer treatment time needed.

2.3 Beam Delivery Techniques

The Bragg peak that characterizes the energy releases of ions asks for high precision in the delivery of the beam to the patient. The features of the beam sent to the patient, like direction, fluence, energy, are computed by a complex software control system, the Treatment Planning Systems which will be described in Sec. 2.4. In parallel with the software computation, the precision of the dose distribution, and so the efficacy of the treatment, is strictly dependent on the beam delivery system that physically delivers the beams. In designing the treatment plan, attention must be paid to several items that could bring to an overdose of healthy tissues and underdose of tumor. Some possible problems can arise from technical aspects like mistakes in the patient geometry or density reconstruction by imaging, errors in

beam delivery. Problems can also be due to unavailable aspect of the treatment like the morphological changes between fractions or intrinsic patient movements like breath.
Two main strategies for beam delivery are followed in the ion therapy facilities currently in operation: *passive beam modulation* and *active beam scanning*. The first technique, described in Fig. 2.5, obtains a uniform and conformal dose distribution by using passive field shaping elements.

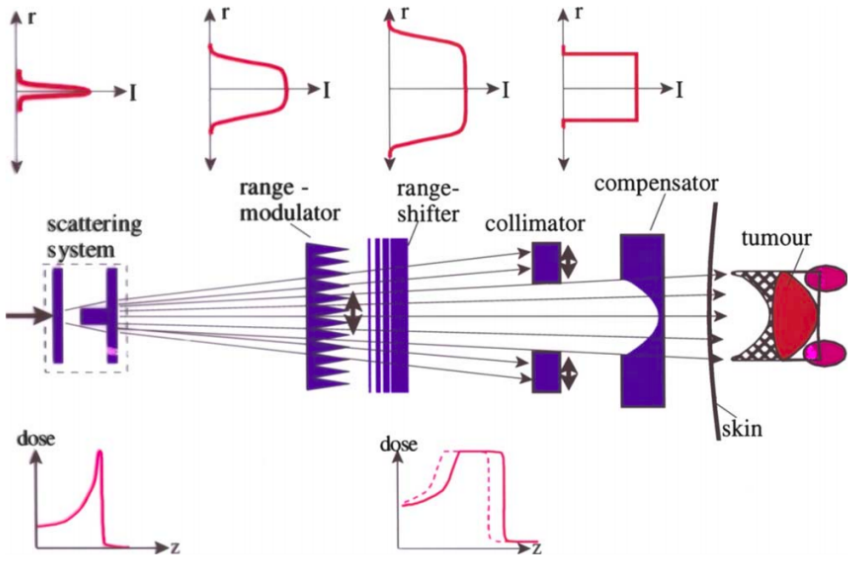

Figure 2.5. Sketch of a fully passive beam shaping system. The initially narrow beam is broadened by a scattering system and adapted to the target volume by various passive beam shaping devices. Adaption of the dose field to the distal contour of the target volume is achieved by a compensator, but results in unwanted normal-tissue dose in the proximal part (indicated by the doubly hatched area) [7].

The beam initially narrow is broadened by a scattering system. Then, the energy spectrum of the beam, initially almost monoenergetic, is spread by the range modulators, in order to cover the longitudinal size of the tumor. In the end, a collimator and a compensator are designated to shape the beam field on the target. With this procedure, thanks to the scattering, the dimension of the beam increases until it has the transverse dimension of the tumor. The main disadvantage of passive techniques is the undesired dosage to proximal healthy organs comes to the secondary fluxes produced by the interaction of the beam with materials of passive elements. In particular, secondary neutrons can travel long distances and release unavoidable and unwanted dose in normal tissues of the patient.
In the active beam scanning (Fig. 2.6), with the CT as a point of reference, the tumor volume is ideally divided into a small spot grid with a given energy layer spacing and lateral spot spacing with sizes varying from some tenths of mm up to 5 mm. The set of beams with the same energy is called a slice. With the guidance of the control system, scanning magnets deflect and steer a single mono-energetic beam, called pencil-beam, to deliver dose to many voxels of the CT and the dose grid. The spot grid points are typically placed by an optimizer not only inside the Planning Target Volume (PTV) but also outside (adjacent to the PTV). The depth

of penetration of the Bragg peak is adjusted by varying the initial kinetic energy of the beam in order to release, as the sum of different pencil beams, the planned dose to each small volume.
The scanning of the spot grid point along with the slice, performed by magnetic beam deflection, gives a zigzag scan path. One advantage of active scanning systems is that no patient-customized hardware is needed, except for the immobilization apparatus. Furthermore, the absence of materials interposed between the accelerator exit-window and the patient avoids the production of harmful secondary radiation. The other benefit of this technique is that the possibility of changing the dose for each spot grid point allows to compensate for pre-irradiation of proximal regions and to obtain a homogeneous dose distribution to any irregular volume. On the other hand, active scanning asks for accelerator high level performances in terms of energy stability and beam deliver position reproducibility. Even if control and safety systems are more demanding with respect to passive technique, these advantages make active scanning the preferred delivery system in all the new PT treatment centres.

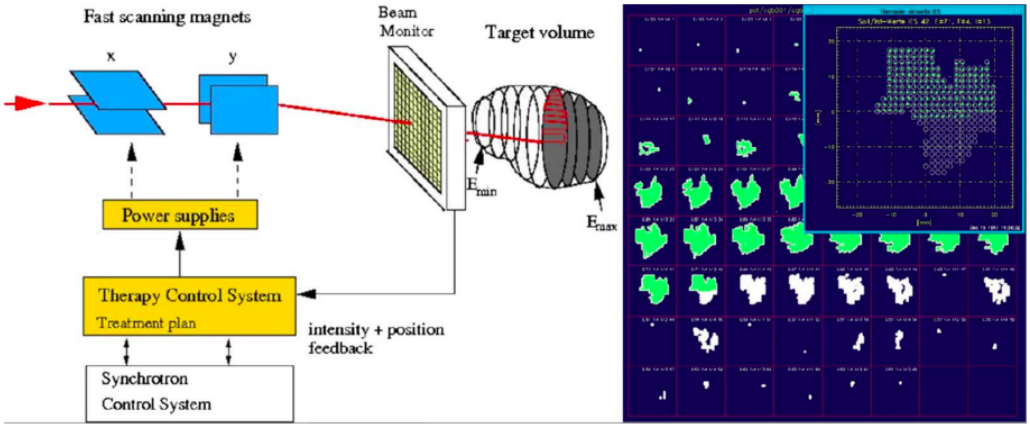

Figure 2.6. Principle of the intensity-controlled magnetic scanning system at GSI. Left: the target volume is irradiated by moving a pencil-like ion beam with fast magnets over thin slices in depth. The required beam parameters are supplied on a pulse-to-pulse operation by the synchrotron control system. Right: Beam's-eye view of slices for a typical patient treatment plan. In each panel, one slice is shown. The actually irradiated slice is seen in the magnified panel with the raster point positions indicated as open circles. The superimposed dots show the beam center positions measured online by a multiwire chamber. The spot size of the beam is larger than the circles and overlaps many positions [7].

2.4 TPS

As already observed in the previous section, in particle therapy treatment, the achieved steep dose gradients demand highly accurate modelling of the interaction of beam particles with tissues. The high ballistic precision of hadrons may result in a superior delivered dose distribution with respect to conventional radiotherapy only if accompanied by a precise patient positioning and highly accurate treatment planning. This second operation is performed by the Treatment Planning System

(TPS). These are sophisticated software that provide position, intensity and direction of the beams to the accelerator control system. Between the tumor diagnosis and the treatment delivery, there is a strict procedure of planning, verification and validation where TPS have a fundamental role in several steps:

1. radiation oncologist prescribes the dose to deliver to the tumor and the dose constraints to surrounding healthy tissues;
2. acquiring patient anatomical data from dicom images, generally provided by Computer Tomography (CT), the TPS computes the optimized set of beams to compose the treatment plan aimed to release the planned dose to tumor;
3. the TPS calculates the 3D dose distribution ensuing from the treatment plan;
4. the radiotherapist approves (or not) the plan;
5. the plan is delivered to a water phantom and the measured dose data are compared with dose map computed by TPS recalculating the plan in a water target;
6. the treatment is delivered to the patient.

Two major issues related to Treatment Planning System for particle therapy are the accuracy of the dose calculation and the computational time required. The first one should be maximized as much as possible. The second one has to be minimized in order to not protract too much the interval between the diagnostic examination and the treatment and to not compromise the center efficiency.
Different 3D dose computation techniques are used. Focusing on the active scanning system, the two main types of approaches to evaluate the dose released by each pencil beam to the patient are the *analytical pencil beam algorithm* and the *Monte Carlo simulation*. Both of them have advantages and limitations and study are in progress to improve the efficacy of the software. In the following sections, the two different approaches are described and the main strong and weak points highlighted.

2.4.1 Analytical pencil beam algorithm

Most commercial Treatment Planning Systems used in particle therapy center are based on analytical algorithms. The first step of an analytical algorithm consists of converting the patient morphology obtained from diagnostic examinations into a water-equivalent path length geometry. This means that each grid's spot dimension is re-scaled by a factor equal to the ratio between the density of the tissue and the density of the water. Then, each pencil beam energy and dose profiles are remapped into the new grid.
The dose distribution of each spot is modelled by a single pencil beam and on the transverse plane, it is described with a 2D distribution function. The integral of the function is kept equal to the integrated depth dose given by the database. The dose distribution of a single pencil beam is described both longitudinally and laterally using analytical functions, obtained for each available energy through fits of both MC simulations and experimental data. The lateral dose distribution can be modelized with a single or double Gaussian function, according to the accuracy required.
The point of strength of the analytical algorithm, if compared with full Monte Carlo simulations, is the short computing time required. On the other hand, the accuracy of analytic algorithms is not satisfactory. In particular, for those cases with a large

degree of tissue heterogeneity, a small amount of inaccuracy in dose calculation in pencil-beam algorithms may lead to a significant shift of dose distributions, possibly resulting in underdosage to the tumor and/or overdosage to the critical structures [32].
The main problem of analytical TPS is that they are often not accurate in predicting doses for heterogeneous anatomies. With analytical TPS the geometry of the patient is converted into a water-equivalent grid, in which the tissues sizes are scaled by the density of materials and their mean stopping power, normalized by the respective quantities related to water. In this way, the real atomic composition of tissues is disregarded. Problems correlated to heterogeneities, range uncertainties, uncertainties in nuclear fragmentation cross-sections, uncertainties in RBE, changing from dose-to-water to dose-to-medium reduce the accuracy of the simulations. In active scanning delivery, the uniform and conformal dose distribution are achieved by the superposition of thousands of beams and tails are important because they cover the shadow zone between the beams cores.

2.4.2 Monte Carlo TPS

In order to exceed the limitations of the analytical algorithm related to the accuracy of dose distribution computation, Monte Carlo can be used. It has been demonstrated that the use of MC in PT could lead to a significant reduction in treatment planning margins [33], due to its accurate physical treatment of the interaction of the beam with the patient tissue. The main disadvantage of MC TPSs is their high computational resources needed. As it will be explained in Chapter 3, the standard full-MC dose calculation methods still cannot meet the constraints on computing time needed for the clinical practice. Full-MC is applied only for recalculating treatment plans already computed with a standard analytic algorithm in particularly difficult cases, or for research purposes, because it requires a too large amount of time for routine applications for all patients [34].
The advent of general programming Graphics Processing Units (GPU) has prompted the development of MC codes that can dramatically reduce the plan recalculation time with respect to full-MC codes in CPU hardware [35][36][37][38][39][40][41][42][43][44][45][46][47]. The impressive speed gain compared to CPU-based calculations is due to both algorithmic simplification and hardware acceleration.
Thanks to GPUs high-performance computing the MC simulation time is hugely reduced. In Chapter 3 a detailed description of the differences between full-MC and fast-MC will be given.

2.5 Dose Monitoring

Another important strategy to ensure a high quality treatment in particle therapy is on-line dose monitoring. For proton and ion beams, which end their path inside the body of the patient, it is not possible to monitor the range of the beam, and therefore the actual extension of the pencil beams does release. During the treatment, it is possible to know only the energy of the beam before it penetrated the body and the transverse position of the pencil beam (usually monitored by ionization chambers). Therefore, in order to avoid mainly underdosage to the tumor and also to avoid release of dose in organs at risk close to the treated volume, usually, safety margins are introduced. This margin expands usually the dose release also to tissues that could be spared if the spatial deposition of dose would be monitored.
An on-line dose distribution monitor would allow the possibility of correction of the

plan during the patient irradiation in case of deviation with respect to the planned treatment with a significant improvement of the treatment quality. In PT the techniques for monitoring the dose release are based on the detection of secondary particles produced in the interaction of the beam with the matter that escape the body: prompt photons produced by the de-excitation of the excited nuclei during the interaction between the beam and the target, β^+ emitters (with a consequent annihilation in pairs of photons that are detected) and charged secondary particles, mainly protons, produced by nuclear fragmentation.
In this section, the main techniques used post-treatment and the strategies to have monitoring that allows a response on the treatment during its delivery (on-line) will be addressed.

2.5.1 Monitoring with photons

A post-treatment way to monitor the path of the beam in the body is the use of a Positron Emission Tomography (PET). It is based on the simultaneous detection of two photons emitted in the opposite direction (back to back) of 0.511 MeV produced by the annihilation of a positron and an electron in the medium.

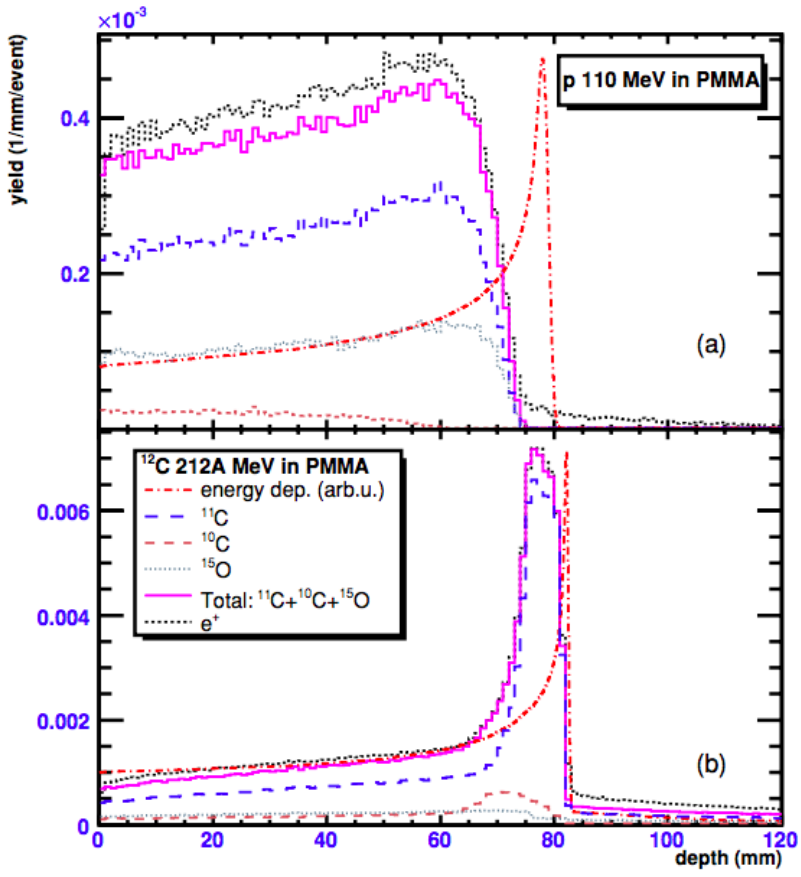

Figure 2.7. Comparison between the distributions of β^+ emitters with the dose profile in the case of 110 MeV proton (top) and 212.12 MeV/u carbon (bottom) beams in a PMMA phantom (predictions with the GEANT MC code [48].

In standard PETs, used for diagnosis of metabolic activity and the presence of tumors, the photons are emitted by the decay of emitter β^+ isotopes that are injected into the patient using a radiotracer.
In particle treatments, this method is based on the detection of the pair of annihilation photons generated by the decay of β^+ emitting isotopes (mainly ions of ^{10}C, ^{11}C, ^{15}O, ^{13}N) produced as a result of the reactions of nuclear fragmentation or excitation between the projectile and the target nuclei of the irradiated tissue. As it is possible to observe in Fig. 2.7, the distribution of the emission position of the β^+ is correlated with the deposited dose and therefore with the range of the beam [49][48].
Considering the space constraints available in a treatment room for the installation of beam control devices and the need to have adequate mechanics and optics of the accelerator machine to optimize the delivery of the beam to the patient, it is not easy the installation of a PET scanner for patient monitoring during treatment. Several procedures have been tried taking PET data after irradiation, in the treatment room (in-room PET) or moving the patient to a standard PET scanner (off-line PET). Finally, PET monitoring procedures during irradiation are under development [50][51]. The off-line approach has been extensively tested [52][53] and intrinsic alignment uncertainties have been reduced with accurate positioning. However, the displacement must occur very quickly since the activated radioisotopes have average lifetimes from 2 min (^{15}O) to 20 min (^{11}C) and the irradiation on the patient can range from a few minutes up to 10 minutes depending on the treatment. A PET monitoring procedures in-room has been tested [54][55] monitoring the patient after the irradiation for several minutes in the same treatment position. A range control accuracy of a few mm and satisfactory control of the daily intersession anatomical changes have been obtained. Despite this, the impact of this procedure on the patient workflow, both for data taking and analysis, causes some limitation on the use in the clinical practice. The intrinsic limitation of this technique is given by the space constraint, the reduced activity produced by the beam with respect to a standard PET activity (up to two orders of magnitude less) and to the long lifetimes of the β^+ emitters with respect to the irradiation time. As it is possible to observe in Fig. 2.7, the isotope emitted with more statistic is the ^{11}C which has a lifetime (20 minutes) not compatible with online monitoring. Moreover, since several isotopes with different lifetimes contribute to the signal, in each moment the observed rates are the sum of several contributions and specific mathematical filtering is required to unfold the dose profile. Another problem is that, after being created, the radioactive isotopes interact with the metabolic system of the body moving to other regions and therefore worsening the image quality.
An innovative strategy under development is to detect prompt photons produced by the de-excitation of the excited nuclei in the interaction between the therapeutic beam and the patient's tissues. A correlation was observed experimentally between the prompt photon emission and the dose release profile [56], as shown in Fig. 2.8. Prompt photons are emitted with typical times of nuclear de-excitation (10^{-16}-10^{-12} s), therefore this method is independent of metabolism.
To detect prompt radiation, the same techniques used for the SPECT (Single Photon Emission Computed Tomography) is used. The other advantage of prompt photons monitoring is that the geometrical limitations are less important than PET monitoring. This is because these detectors, detecting not correlated photons, not required to be positioning in a ring or face to face. At the same time, also in this situation, it is not possible to use a standard SPECT, unless one uses thick collimators, with the consequent limits of dimensions, weight and statistics.
An alternative currently under construction proposed by IBA (Ion Beam Applica-

tions) is the use of a slit camera [57]. This method, shown in Fig. 2.9, consists of a slit collimation system that gives a 1D projection of the emission gamma prompts along the beam path on a scintillation detector.

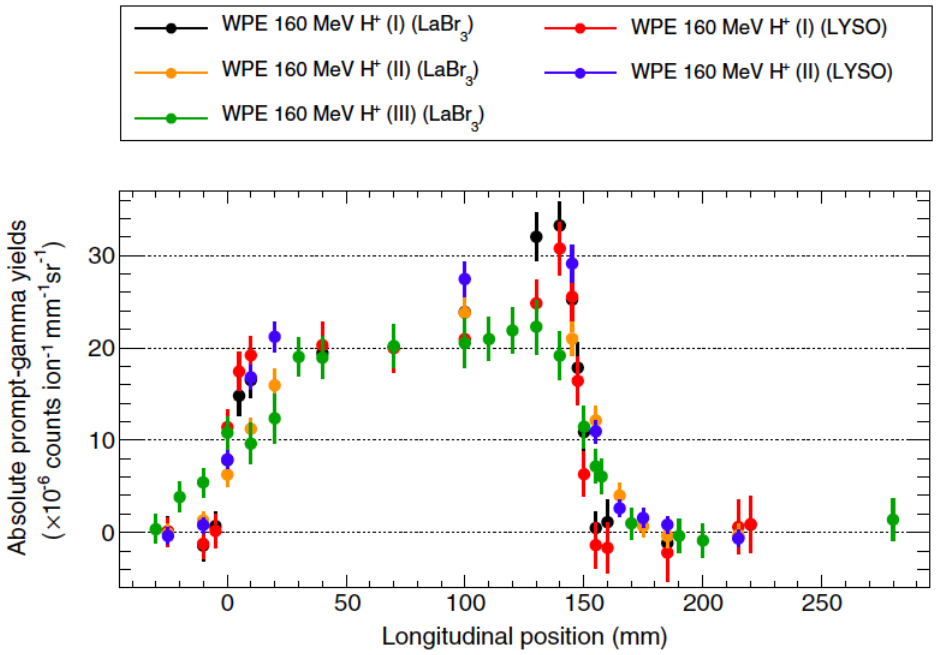

Figure 2.8. Prompt photons produced by the nuclei de-excitation due to the interaction of a 160 MeV proton beam with a PMMA target. At that energy the Bragg peak is expected at 180 mm [56].

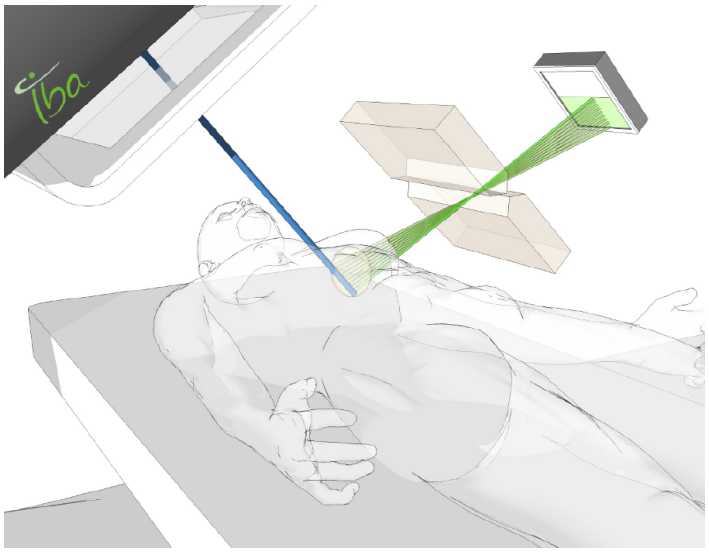

Figure 2.9. Range measurement of a proton beam (blue) through a slit camera. In green the prompt photons, emitted by the beam in its path across the body, are represented [57].

The goal is to measure only the point where the beam stops in the body of the patient and being in one dimension is meant to be used in therapies where only one beam is chosen. It must be noticed that the monitoring that uses secondary photons can be applied only with proton beams since the treatments with helium, carbon and oxygen have such a background level of neutral radiation as to make impossible the monitoring.

2.5.2 Monitoring with charge particles

Another technique exploits secondary charged particle produced during the nuclear fragmentation of ions in the body. Charged particles can be easily tracked with high efficiency with a small amount of background and it is possible to correlate the point of fragments emission with the beam range, as shown in Fig. 2.10.

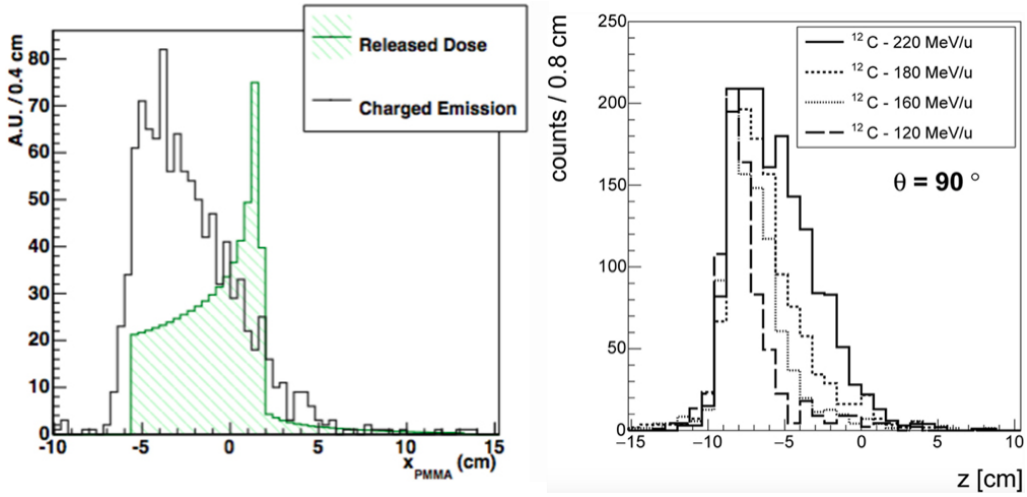

Figure 2.10. Left: FLUKA simulation of comparison between the longitudinal profile (black) of the charged secondary particles detected at 90 degrees and the dose distribution (green) versus the penetration in a PMMA target [58]. Right: emission profile of secondary fragments detected at 90 degrees produced by carbon beams at different energies. The zero of penetration is the position of the Bragg Peak [59].

This technique is however limited by the few statistics of the secondary charged particles exiting the patient. In particular, the higher energetic secondary particles that can easily be detected outside the patient are usually emitted at forwarding angles with respect to the beam direction. The forward peaked secondary gives a worse accuracy in the reconstruction of the emission point (needed to reconstruct the beam track inside the body). Moreover, usually, it is impossible to place a detector in the forward direction in a treatment room. Despite this, it has been demonstrated that at large angles with respect to the beam (60°-90°) the statistic is enough to monitor the beam range [60][61][58][62].
This technique can be applied successfully to carbon therapy since the main source of the charged secondary used is originating by the beam fragmentation, absent with proton beams. The use of a tracker device to exploit the charged particles for monitoring purpose in carbon therapy is under study. The detector (Fig. 2.11) has been built, tested and actually it is at the CNAO for a clinical trial with patients

[63][64][65].

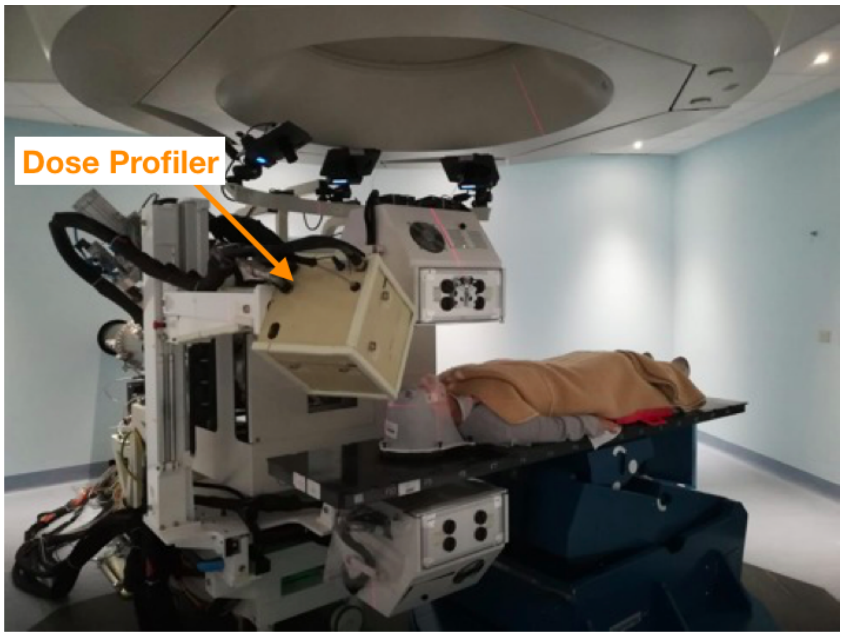

Figure 2.11. Photo of the first clinical trial of the Dose Profiler during a carbon ion treatment of a head tumor at CNAO [63].

Chapter 3

From full-MC to fast-MC

Monte Carlo (MC) calculations are a standard tool in several areas of research, and particularly in physics. This name is used to refer to any technique in which complex models are evaluated by generating random samples in a sequence, and interpreting statistically the global result after numerous iterations.
MC algorithms can be applied in particle therapy to evaluate the dose release in the patient. The simulation software follows the trajectory of a beam particle along its path in the tissue. The interactions are simulated ("happen" in the MC scheme) according to their computed probability. In the generation of these interactions, the patient morphology (geometry and materials) is obtained by the mapping information (usually the CT) and accurately taken into account.
MC codes could be an excellent alternative to analytical methods due to their detailed description of radiation transport and interaction with matter. The suitability of a MC code for the application to particle therapy demands accurate and reliable physical models capable of handling all components of the expected radiation field. This becomes extremely important to correctly predict not only the physical but also the RBE-weighted dose, especially in cases where ions heavier than protons are involved. Furthermore, accurate prediction of emerging secondary radiation is important in innovative areas of research aiming at in vivo treatment monitoring.
MC techniques can be more effective compared to analytical methods for different aspects:

- MC methods take into account more realistically the composition of the human body [66][67][68], with a possible advantage over the water-equivalent approach typically used in analytical TPS;
- MC methods include mixed field description and three-dimensional spread of the particle fluence, reliably describing the transport and the interaction of the primary and secondary particles [69][70];
- In-beam monitoring of the irradiation, described in the previous chapter (Chapter 2.5), can be performed using MC simulations, fully taking into account the complexity of the mixed radiation field and tissue stoichiometry [68][71][72][73].

Despite the gain in accuracy achievable using MC dose calculation, pencil-beam-based algorithms are widely used in clinical practice [74] mainly because of their high computational efficiency. On the other hand, the accuracy of a MC dose calculation is determined by the total number of particles simulated and an enormously large number of particles are usually necessary to yield a desired level of precision. Usually,

to simulate a complete treatment plan, one needs to typically track 10^7-10^9 particles, and a full-MC code could take several days to perform the calculation on a single CPU. Due to such a long computational time, full-MC is applied only to recalculate existing treatment plans for research studies and not to routine applications for patients [34]. Many MC simulation packages have been used as dose computation engines for TPS. In particular, the use of GEANT 4, FLUKA, and MCNP X is quite popular [75][76]. Despite the great efforts devoted to accelerating the full-MC dose calculation process [77][78][79][80], the full-MC dose calculation methods still required too much CPU time for clinical practice.
An alternative is the use of a fast-MC which can run on GPU to have more accuracy than an analytical pencil beam algorithm with less computational time than a full-MC TPS. Fast-MC codes are nowadays used increasingly in clinical routine for photon, electron and proton therapy [81][82].
In this chapter, a comparison between a full-MC code, FLUKA, and a fast-MC code, FRED, will be presented.

3.1 full-MC code: FLUKA

The FLUKA (*FLUkturiende KAskade*) [83] is a general purpose Monte Carlo code simulating the interaction and transport of hadrons, heavy ions, and electromagnetic particles. It is developed by the European Organization for Nuclear Research (CERN) and the Italian Institute for Nuclear Physics (INFN). It is built with the best possible physical models in terms of completeness and accuracy. Its microscopic approach allows giving a solid physical foundation to each step.

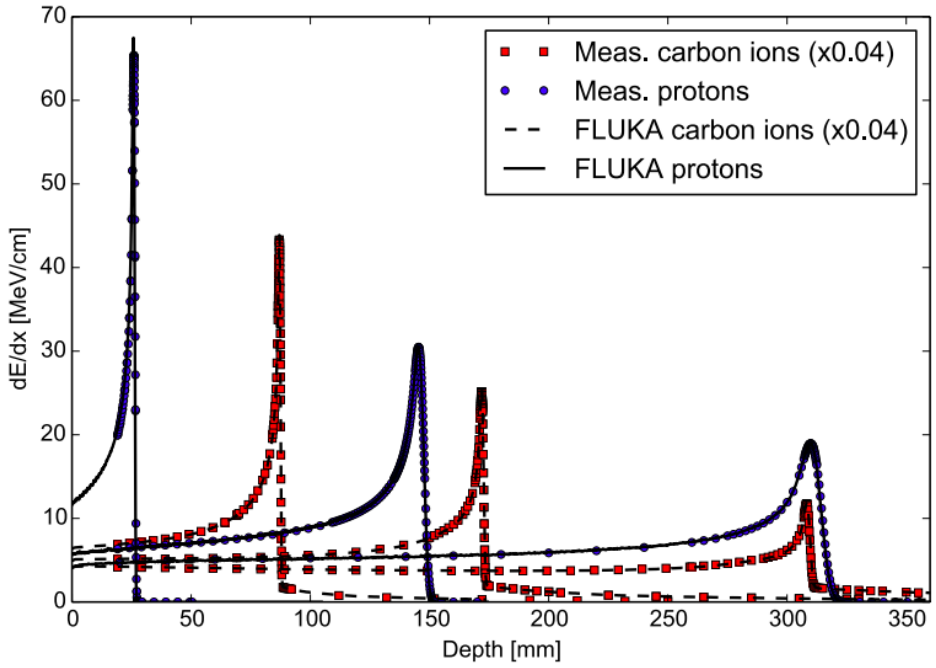

Figure 3.1. FLUKA simulations of depth–dose profiles of protons and carbon ions with therapeutic ranges in comparison with measured data at HIT [84]. The nominal energies before the beamline are 54.19, 142.66, and 221.05 MeV for protons, and 200.28, 299.94, and 430.10 MeV/u for carbon ions [85].

Performance is optimized comparing with particle production data at the single interaction level. No adjustment is made on integral data, such as calorimeter resolutions, thick target yields, etc. Therefore, the final predictions are obtained with a minimum set of free parameters, fixed for all energies and target/projectile combinations. Results in complex cases, as well as scaling laws and properties, emerge naturally from the underlying physical models and the basic conservation laws are fulfilled a priori. Moreover, the microscopic approach preserves correlations within interactions and among the shower components and it provides predictions where no experimental data are directly available.
Physics models of superior quality have extended the use of FLUKA to medical applications. FLUKA is one of the first general-purpose MC codes which translates DICOM files into voxel geometry as part of the combinatorial geometry package of FLUKA. The electromagnetic and nuclear models of FLUKA can reproduce reasonably well measured depth and lateral dose profiles in water for all ions of interest in the therapeutic energy range. For different high-accuracy data sets, FLUKA can reproduce the position of the Bragg peaks of proton and carbon ion beams with a single ionization potential on average within the experimental uncertainties of about 100 μm. The average dose-weighted dose-difference ($\overline{\Delta D/D}$) is below 1% for protons and below 1.5% for carbon ions as reported (Fig. 3.1) [85]. In this way, the code can be chosen for the generation of TPS input data as well as a valuable tool to support the analytical TPS developments of some commercial vendors. Special efforts have been devoted to the improvement of the FLUKA nuclear interaction models, which provide benchmarked and reliable results for interaction cross-sections and particle production by proton and ion beams at therapeutic energies. In particular, they allow describing consistently the transport and interaction of primary particles and all produced fragments, including transport of electromagnetic particles. All reaction generators share the same equilibrium particle emission, thus profiting together from the past and latest developments of the evaporation, fragmentation, and deexcitation models. Low energy nuclear models are of the maximum importance for applications to in vivo monitoring techniques. However, as it will be highlighted in Sec. 3.3, this high accuracy has a high computational cost. For this reason, FLUKA cannot represent at the moment a valid alternative to analytical TPS in clinical practice.

3.2 fast-MC code: FRED

FRED (*Fast paRticle thErapy Dose evaluator*) [1] is a code that runs on GPU originally devoted to the recalculation of proton treatment plans, and it is presently expanded in order to also track light ions, electrons and photons. By rapidly recalculating a complete treatment plan within minutes, instead of hours, it paves the way to many clinical applications where the time factor is important.
In developing the algorithms, the goal is to balance accuracy, calculation time and GPU execution guidelines. To do so, the most effective physical models from the literature have been chosen, avoiding the simulation of all the unnecessary information for the calculation of dose. For many processes, FRED relies on a library of pre-computed look-up tables instead of performing an explicit calculation. This approach performs extremely well on GPU cards where hardware interpolation can be exploited using the so-called texture units.
The simulation domain is the phantom, which can be represented or by a uniform volume of material (for example liquid water or PMMA), or by the 3D reconstruction of a patient based on a series of CT scans. The phantom is divided, through a

uniform cartesian grid, in voxels, each of which stores information on the local density of the medium and on the chemical composition. Conversion of CT values from the Hounsfield Unit (HU) to the density of the material is carried out by using the appropriate conversion tables.
The simulation setup is performed by analyzing an input file or it can be prepared via a series of python scripts that parse the DICOM files containing the patient's CT together with the composition morphology, radiation therapy plans and dose maps calculated by the Treatment Planning System (TPS). Once the full geometry is imported, the primary particles are generated using the treatment plan prescription. Depending on the hardware on which the code runs, the kernel adopts several strategies for distributing the workload between the available computational resources.
The code can transport particles through the 3D voxel grid using a class II MC algorithm [86]. The path of the particle is generated in various steps by combining the continuous interaction models and discrete nuclear interaction models. The continuous processes predict the average energy loss, the energy fluctuation and the average scattering angle. The end of a step corresponds to voxel boundary crossing or the occurrence of a discrete interaction event. In the case of nuclear interaction, the relevant cross-sections are considered and the actual interaction is determined by a sampling procedure. In these nuclear collisions, fragmentation events may occur with the consequent production of secondary particles; the latter are queued for subsequent tracking. A particle is no more tracked when it goes out of the phantom, or when its energy goes below the tracking threshold.

3.2.1 Current status and future perspective of FRED

As far as proton beams are concerned, FRED is already used as a quality assurance tool in the clinical center of Maastricht and Krakow and as a research tool at several clinical and research centers in Europe (Krakow, Trento, Maastricht, Lyon and PSI).
The implemented models and FRED performance were extensively tested versus several measurements in each treatment center that adopted the package. In the following, a comparison between FRED and the full-MC codes FLUKA and Geant4 for protons in liquid water is shown.
In Fig. 3.2 the Dose Depth Distribution (DDD) obtained by FRED, FLUKA and Geant4 simulations for monoenergetic proton beams in a water phantom is shown with the different component of the contributing physical interactions switched on. In order to observe all the curves together, beams had been simulated with different initial energies. To check each interaction model separately, the elastic and inelastic nuclear interactions were switched on and off. Profiles closely overlap for most of the particle range and only near the peak there are slight differences. However, the agreement with FLUKA is within 1.5% of the Bragg peak value for all models in the energy range of PT (50-250 MeV) [1]. In Fig. 3.3 an example of the agreement between FRED and FLUKA simulating a beam of 150 MeV/u is shown in detail.
To be sure to have under control the contribution of long-range lateral tails in the dose distribution, the Field Size Factor (FSF) test has been performed (Fig. 3.4). The test has been performed into homogeneous conditions, placing a Markus chamber inside a liquid water phantom to detect dose. A set of pencil beams with the same energy and fluence is delivered to the phantom, distributing the scan spots on a square grid with constant spacing centered on the detector. The size of the grid is increased and the dose recorded by the detector is scored at several depths in the water. The collected data have been compared with the FRED simulation, showing a very good agreement.

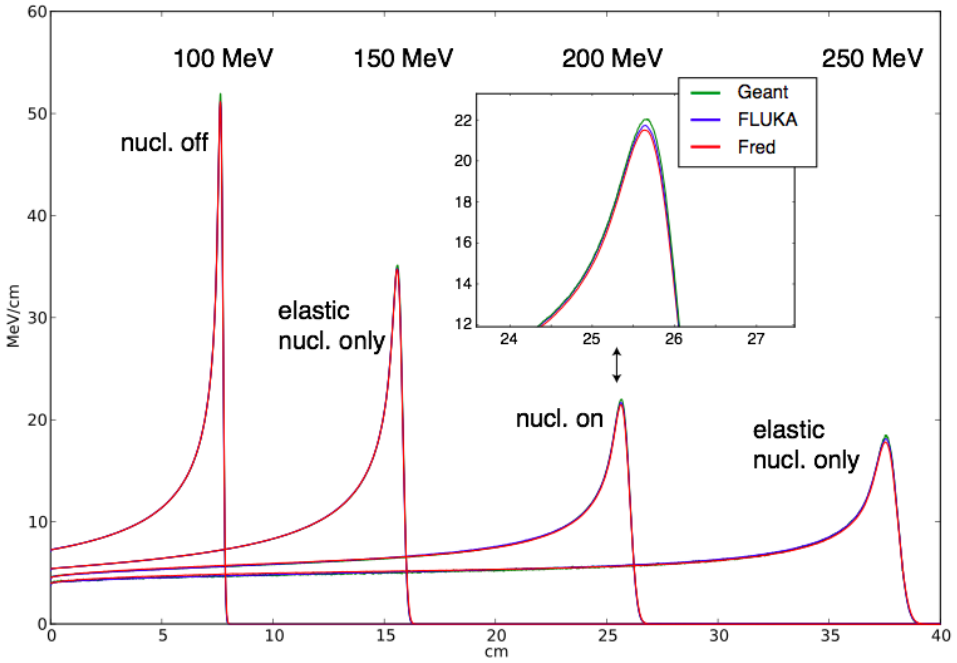

Figure 3.2. Bragg curves for protons in water with different energies. The nuclear interactions were switched on/off to check each model separately, FRED (red), FLUKA (blue) and Geant4 (green) calculations are presented. The zoom shows the peak details for 200 MeV protons with the complete physical model [1].

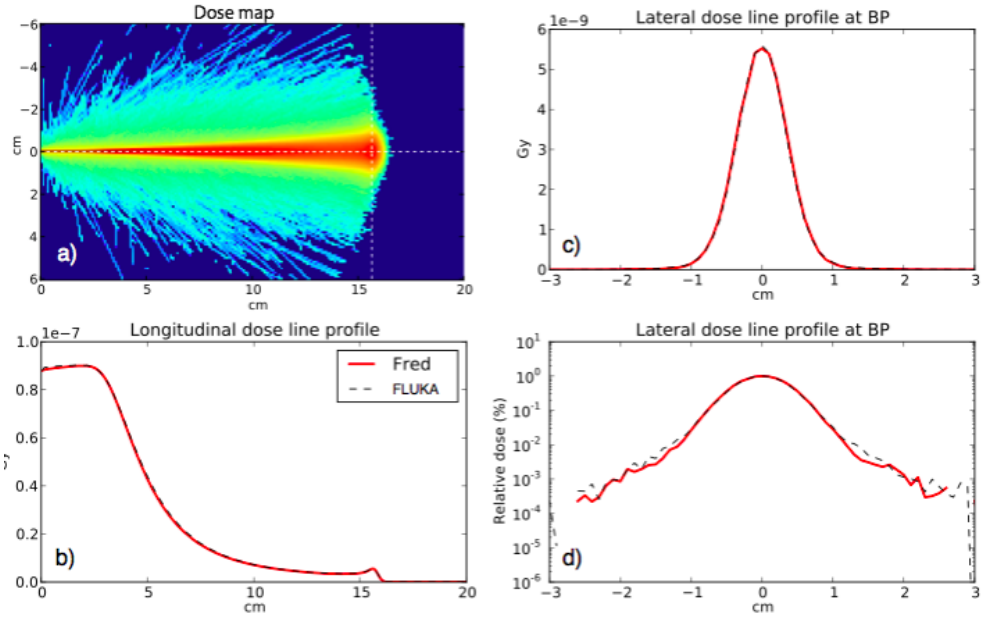

Figure 3.3. Dose in water for a 150 MeV proton beam with 0 FWHM. It is possible to observe: the dose map (a), the central axis profile along beam axis (b), the lateral axis profile at 15.6 cm depth in linear (c) and logarithmic (d) scale [1].

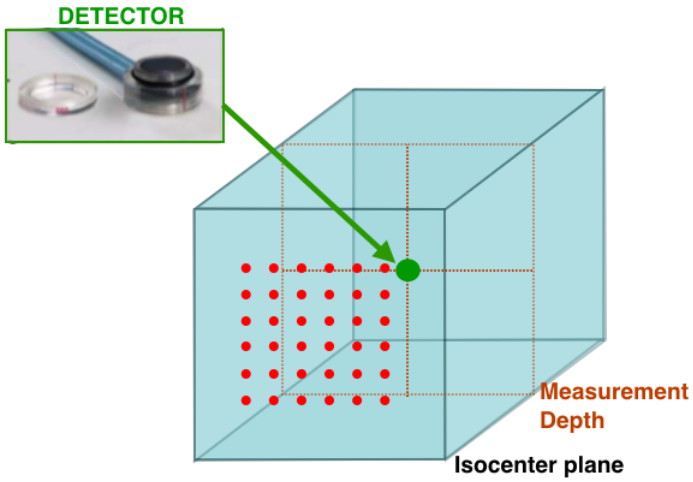

Figure 3.4. The Field Size Factor test. The detector (a Markus chamber) is positioned inside a box of water and its depth can be changed. The beam is shot on a grid configuration with a spot interspacing of 2 mm and a spot intensity of 5×10^7. The measurement has been repeated for different energies, fields size and depths [1].

The FSF test has been used for a series of proton energies in water both with FRED and FLUKA. Fig. 3.5 shows a comparison of the measured dose with FRED. The energy of the beam was 226.61 MeV/n, the detector was at 20 cm of depth and the size of the fields was ranging from 1 to 20 cm.
Computed and collected data points were normalized to their respective value at 10 cm field size. FRED reproduces the experimental data within 2% for the field size up to 20 cm.

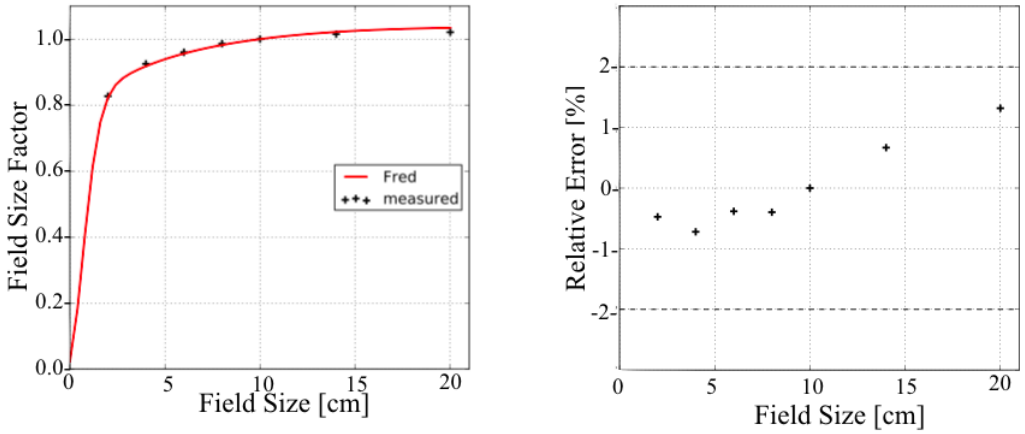

Figure 3.5. FSF test for a 226.62 MeV/n proton beam with the dose detector at a depth of 20 cm in the CNAO water phantom. FSF is normalized to 10 cm size value and computed with FRED and measured data (left), and relative error (right) [1].

Starting from this validated proton beam model, we plan to extend FRED to carbon ion beams and to introduce electron and photon beams. In this way, it will be possible to obtain a fast optimization of the treatment plans also in carbon ion therapy, radiotherapy and IORT (IntraOperative Radiation Therapy). Those

implementations are under development and in this thesis the new data-driven tracking model of carbon ion is described. The ionization energy loss and multiple scattering of ions are analogous to the model used in FRED for protons [1] with some new adjustments, whereas the nuclear model is completely new, and it was originally developed during this Thesis's work. The physical models implemented in the code will be described in Chapter 4.

3.3 Comparison of time performance

The possibility of exploiting the computing power of multiple GPU cards opened up the way to bring MC simulations into the treatment planning itself. The new hardware demanded a new bottom-up development of a tracing kernel to balance the speed of calculation with the accuracy of implemented physical models. The FRED code has reached a considerable speed-up in the plan recalculation, namely a typical run of about 72 h/core [87] can now be delivered in less than 2 min on a GPU-fitted workstation. The code can run on a variety of hardware configurations, and it can be used as a standalone application or it can be driven as an external library.
In Table 3.1 the time performance of FRED for different hardware architectures is presented in comparison with the same simulation performed with the full-MC code (FLUKA). Running on GPU, there is a gain in time of more than 300x compared to execution on a single CPU. It is also important to notice that, in the same conditions (CPU hardware), FRED is 20x faster than FLUKA. This is possible since FRED is a "fast" Monte Carlo. It means that the physics models implemented in the code are simplified, simulating only what is needed for an accurate dose deposition in particle therapy. For MC simulations an important point is that sophisticated models, even if existing, are generally too complex and slow to be integrated into MC codes and, at least for full-MCs, look-up tables are not an option.
All in all, the speed-up in calculation time for FRED with respect to standard full-MC codes can be typically of the order of 1000x.

Table 3.1. FRED performance in comparison with FLUKA and different hardware simulating the same proton beam in a water target.

MC	**Hardware**	**primary/s**	**μs/primary**
`FLUKA`	single CPU core	0.75 k	1340
`FRED`	single CPU core	15 k	68
`FRED`	single GPU card	5000 k	0.2

Chapter 4

Physical model implemented in the code for carbon ion therapy

Charged particle interactions can be classified as continuous and discrete processes. Energy loss due to the Bethe-Bloch mechanism and multiple scattering are continuous processes and their effect can be averaged over a particle step in MC simulation. The discrete processes, as nuclear interactions, are characterized by short-range hard interactions that can be also catastrophic events where the original particles cease to exist. In the model, each discrete process is statistically independent of the others and each one contributes to the total macroscopic cross-section. The interaction probability and related cross-section are computed at each tracking step and it depends on the particle type, energy and medium composition.
The ionization energy loss and multiple scattering of ions are analogous with the model used in FRED for protons [1] with some adjustments that will be described in this chapter. The nuclear model, completely new, has been developed parameterizing existent data. In particular, elastic cross-section has been obtained from *ENDF/B-VII* data [88] while data used for the calculation of the non-elastic, or reaction, cross-section are those of the papers of *Tacheki* [89], *Zhang* [90] and *Kox* [91][92]. Data used for the choice of the combination of fragments emitted, energy and angle distributions, in particular the differential cross-section with respect of angle and energy for the production of different fragments in hard nuclear interactions, are those obtained from the experiment at Ganil (laboratory of CAEN, France), where the fragmentation of carbon ions on thin targets (H, C, O, Al and Ti) has been studied [93][94][95]. The experiment provided data about the angular and energy cross-section of a carbon beam of 95 and 50 MeV/u and with detection angles in the range [-43°; 43°]. To have the possibility to simulate all the energies of interest for carbon ion therapy (50-400 MeV/u), an algorithm to scale the energy and angle distribution as a function of the incident particle energy has been developed. A comparison between FRED and the full-MC FLUKA has been used to fill the gaps in the experimental data. The model was not based directly on FLUKA because we felt it was more correct to have an experimental basis. FLUKA itself is based, where possible, on data. By starting directly from the data and choosing how to use the information available in the literature there is more direct control of the model. Furthermore, by building it with look-up tables obtained from experimental data, it will be possible to update the model when there will be results from new experiments. For example, we are waiting for the FOOT experiment [96][97][98][99][100] focusing on the study of nuclear fragmentation. Moreover, by comparing the results of FRED, obtained from data, with the full-MC FLUKA, already clinically validated, there is

a double check on the accuracy of the model.
Another important aspect that has to be taken into account in particle therapy is the Relative Biological Effectiveness (Par. 1.2.7) since, for dose prescription, the increased effectiveness has to be taken into account in treatment planning. For this purpose, the biophysical LEM I (Local Effect Model) approach has been implemented in the FRED code. This approach, which is in excellent agreement with the GPU cards, is already implemented in other MC used in clinical practice (FLUKA [69] and TOPAS [101][102]).
All those models of FRED have been developed to balance accuracy, calculation time and GPU execution guidelines.

4.1 Ionization energy loss

As observed in Sec. 1.1, the most important process through which light ions lose energy in matter is the ionisation/excitation of the medium. Particles interact with the electrons of matter ionizing or exciting them. Electrons absorb energy from the projectile, which consequently loses a little fraction of energy, and keeps on travelling until it comes to rest. The mean energy loss value is well reproduced by the Bethe-Bloch formula (Eq. 1.1) for ions with energy $E \geq 10$ MeV/u. At low energy, when the velocity of the particle becomes comparable to the velocity of electrons in matter, the stopping power significantly departs from the Bethe theory. In passage through matter, the charged particle interacts stochastically with atoms and electrons: this causes statistical fluctuations around the expected value of energy release. The energy loss fluctuations are described by the energy straggling theory and depend on particle energy and material properties. In a thick absorber, corresponding to a large number of ionization events, the straggling distribution is a Gaussian function. For thin absorbers, the distribution is not Gaussian anymore and it becomes skewed with a large tail towards high energy loss events. To distinguish the energy straggling regime, the k parameter (Eq. 1.6) is used.
In particular, as described in Sec. 1.1.2, a Gaussian approximation (thick absorber regime) is used for $k \geq 10$. In the thin absorber regime, for $0.01 \leq k < 10$ the distribution of energy loss is generated by sampling the Vavilov distribution [6]. For $k < 0.01$ the Landau distribution is sampled [5].

4.2 Multiple Coulomb Scattering

In its passage through a medium, a charged particle undergoes many small-angle deflections. This deflection is mostly due to Coulomb scattering from medium nuclei. The overall deflection angle is well-represented by the theory of Moliére of multiple Coulomb scattering [8]. If one considers the small-angle deflection approximation, which holds for most of the particle trajectory in the case of protons and heavier ions, the angle distribution can be considered nearly Gaussian, with zero mean.
The distribution used in the code, as described in *Schiavi* [1], can be derived from the first approximation of the Moliére formula (Eq. 1.35 and Eq. 1.36) already discussed in Sec. 1.1.4.
The single Gaussian is an excellent approximation for a single pencil beam, reproducing 98% of the angular distribution. The tails in scattering angle distribution are typically dominated by the deflections caused by nuclear interactions. Hence the single Gaussian approximation is a valid solution for dosimetric applications when a Monte Carlo tracking algorithm is used. Following *Fippel and Soukup* [78] approach, the standard deviation θ_0 was multiplied by a scaling factor f_{mcs} . This factor was

obtained by comparing FRED and FLUKA simulations of a single pencil beam in water in the mid of the therapeutic energy range and with nuclear interactions switched off. The best match in the region close to the Bragg peak was found by setting $f_{mcs} = 0.987$ for protons, and $f_{mcs} = 1.381$ for all other light ions. In Fig. 4.1 it is possible to observe as the comparison FLUKA-FRED of the lateral distribution at the Bragg peak is worst without the scaling factor f_{mcs}.

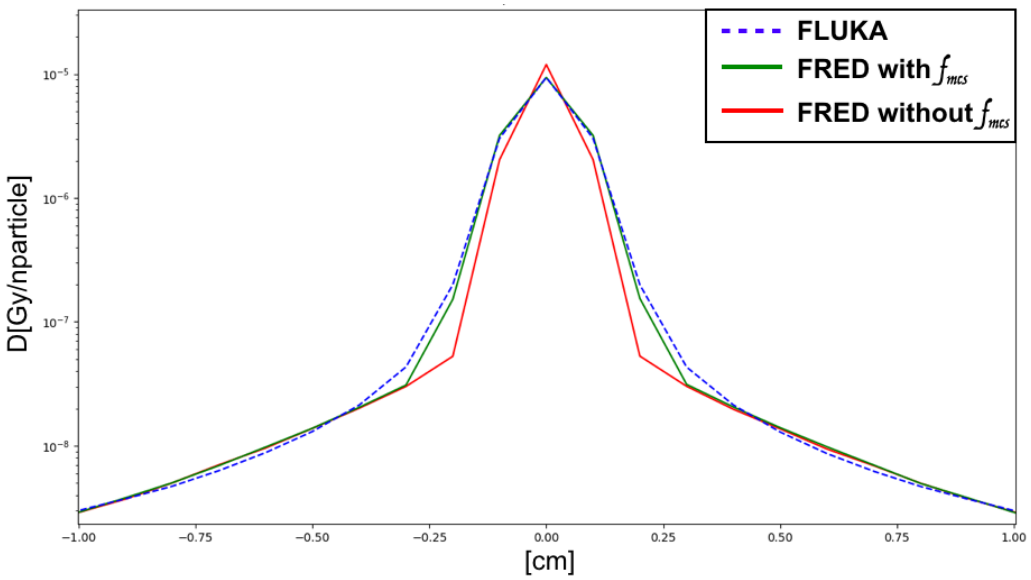

Figure 4.1. Transverse profile at the Bragg peak (8.6 cm of depth) of a 200 MeV/u carbon ion beam in water. In blu dot line the distribution obtained with FLUKA, in green and in red the distribution obtained with FRED respectively with and without the scaling factor f_{mcs}.

4.3 Nuclear Model

Nuclear interactions are handled in two separate steps. First, the probability that a nuclear event happens is sampled. It depends on the mass attenuation coefficient given by the formula:

$$\frac{\mu}{\rho} = \sum_i \frac{N_A w_i \sigma_t^i}{A_i}, \tag{4.1}$$

where the sum is over all the elements of the target compound, μ is the coefficient of attenuation, ρ is the density of the material, N_A is the number of Avogadro, w_i, A_i and σ_t^i are respectively the mass weight, the atomic mass and the total cross-section of nucleus-nucleus interactions of the i-th element of the target.
The total cross-section (Fig. 4.2) is defined as the sum:

$$\sigma_t^i = \sigma_e^i + \sigma_n^i, \tag{4.2}$$

where σ_e^i and σ_n^i are respectively the elastic and non-elastic cross-section.
As explained in Section 1.1.5, the kinetic energy and the momentum are conserved in the elastic event, while for a non-elastic event the total kinetic energy is not

conserved. If there is an elastic event, the new energy and direction of the projectile and the target are sampled. On the other hand, if there is a non-elastic event, the carbon ion disappeared and new fragments are sampled and generated in the simulation.
In the next sections, the procedure to calculate the cross-section and the models used for the nuclear event is described.

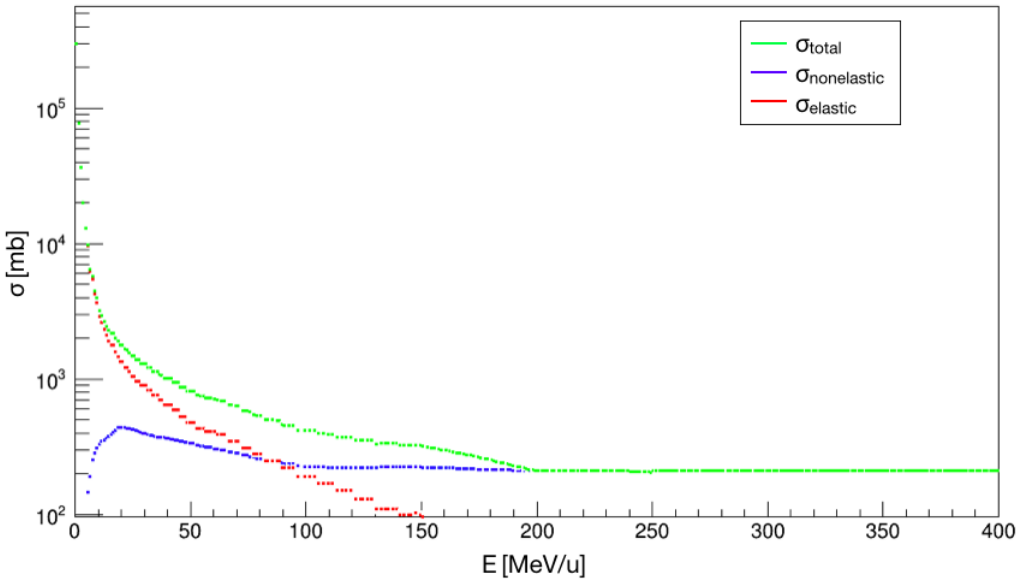

Figure 4.2. Total, elastic and non-elastic cross-sections of a beam of carbon ion on a water targets obtained with FRED. Elastic cross-section is a step function since it is obtained reading a look-up table with a variable energy binning.

4.3.1 Elastic cross-section

The elastic cross-section (Fig. 4.3) is not negligible, when compared to the non-elastic, only if the carbon ion projectile interacts with a hydrogen target. In the center of the mass reference system, an elastic event of a carbon ion on a proton target is not distinguishable from an incident proton on a carbon ion (Fig. 4.4).
For this reason, to sample the elastic cross-section, the latter configuration, which is more described in the literature, has been used (*ENDF/B-VII Incident-Proton Data* [88]). The evaluation of the database of ENDF is based on nuclear model calculations that have been benchmarked to experimental data [103][104].

4.3.2 Elastic event

An elastic collision of a carbon ion on a proton causes the deflection of the ion which gives part of its energy to the proton. The total kinetic energy and the linear momentum are conserved. As it is possible to observe in Fig. 4.4, in the center of mass system, the magnitude of the velocity of the proton and the one of carbon ion before and after the collision are the same and their directions are parallel and opposite.

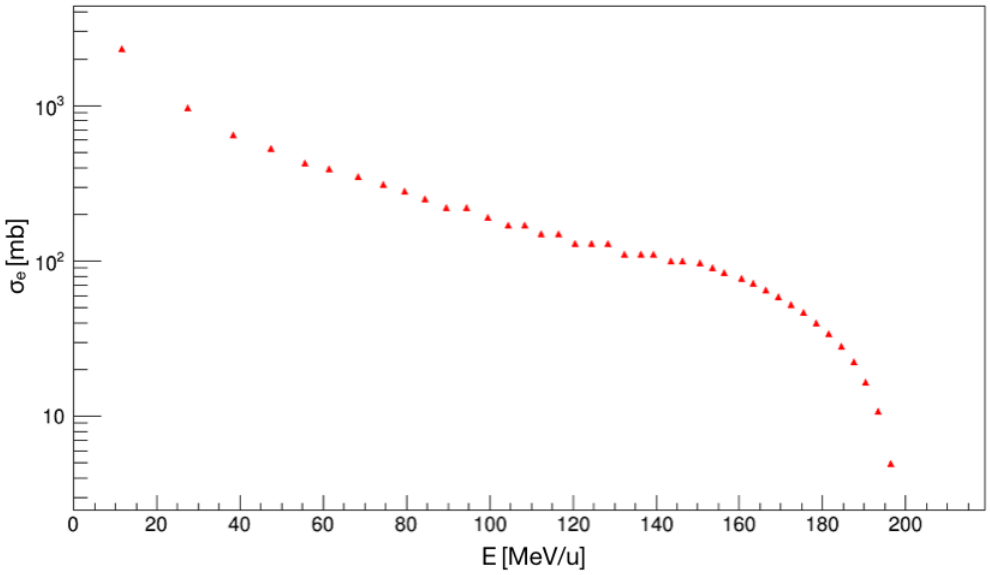

Figure 4.3. Elastic cross-sections of a beam of carbon ion on hydrogen targets obtained with FRED interpolating data of incident-proton on carbon target [88].

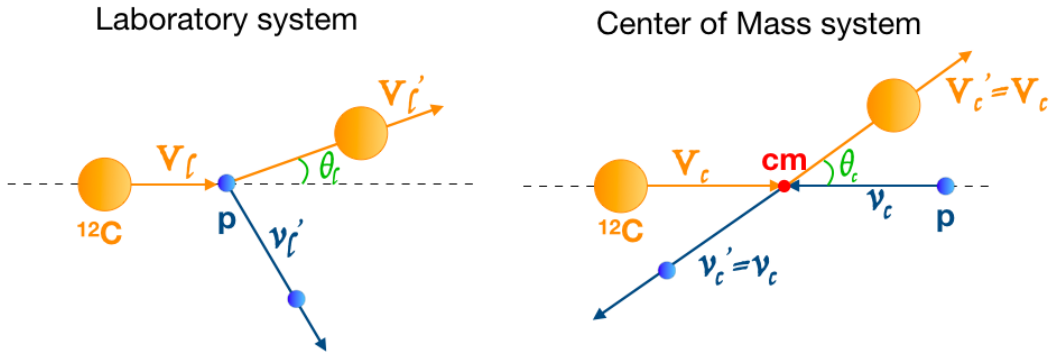

Figure 4.4. Schematic view of the collision between a carbon ion and a proton from the point of view of the laboratory and of the center of mass.

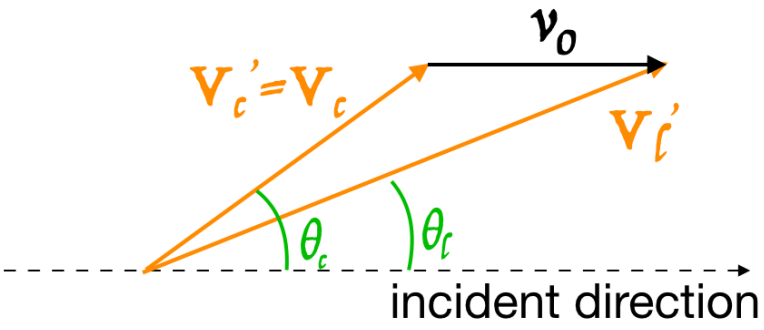

Figure 4.5. Velocity vector diagram after the collision.

It is possible to find the relationship between the carbon ion scattering angles in the center of mass and in the laboratory starting from the velocity vector diagram after the collision (Fig. 4.5):

$$\vec{V}_l' = \vec{V}_c' + \vec{v}_0, \tag{4.3}$$

where $\vec{V}_l'$, $\vec{V}_c'$ and $\vec{v}_0$ are respectively the velocity of the carbon ion before the collision in the laboratory system and in the center of mass system and the velocity of the center of mass.
Making a projection on the axis:

$$V_l' sin\theta_l = V_c' sin\theta_c, \tag{4.4}$$

$$V_l' cos\theta_l = V_c' cos\theta_c + v_0. \tag{4.5}$$

Starting from Eq. 4.5 and applying the rules of the cosine at the angle $V_c' v_0$ in the triangle $V_c' V_l' v_0$:

$$V_l'^2 = V_c'^2 + v_0^2 + 2V_c' v_0 cos\theta_l, \tag{4.6}$$

one obtains:

$$cos\theta_l = \frac{V_c' cos\theta_c + v_0}{\sqrt{V_c'^2 + v_0^2 + 2V_c v_0 cos\theta_c}}. \tag{4.7}$$

To obtain this expression with a dependence just on the angle in the center of mass, it is possible to write v_0 as:

$$v_0 = \frac{mv_l + MV_l}{m + M}, \tag{4.8}$$

where m and M are the proton and carbon ion mass which can be approximated to their atomic number (1 and A), $v_l = 0$, and $V_c = V_c' = V_l - v_0$. So the cosine in the laboratory can be written as:

$$cos\theta_l = \frac{A + cos\theta_c}{\sqrt{A^2 + 2Acos\theta_c + 1}}. \tag{4.9}$$

With this expression it is possible to obtain the angle of diffusion of the carbon ion extracting a random angle in the center of mass. The distribution of projectile and target in the center of mass is isotropic.
Integrating Eq. 4.9, it is possible to obtain the mean angle of deflection in the laboratory:

$$< cos\theta_l >= 1 - \frac{1}{3A^2} = 0.9977, \tag{4.10}$$

which correspond at $\bar{\theta}_l \simeq 3°$. The mean angle of deflection depends only to the atomic mass of the projectile.
With the same procedure it is possible to calculate also the cosine of deflection of the proton target:

$$cos\phi_l = \frac{1 + cos\theta_c}{\sqrt{2(1 + cos\theta_c)}}. \tag{4.11}$$

A comparison of the different distribution obtained for carbon ion and proton is shown in Fig. 4.6.
The other parameter necessary for the description of the elastic event is the new energy of the projectile and the target element. At this aim, it is possible to start again from Eq. 4.6 and to substitute the value of $v_0 = \frac{A}{A+1} V_l'$ and $V_c' = V_l - v_0$:

$$V_l'^2 = \frac{A^2 + 1 + 2Acos\theta_c}{(A+1)^2} V_l^2. \tag{4.12}$$

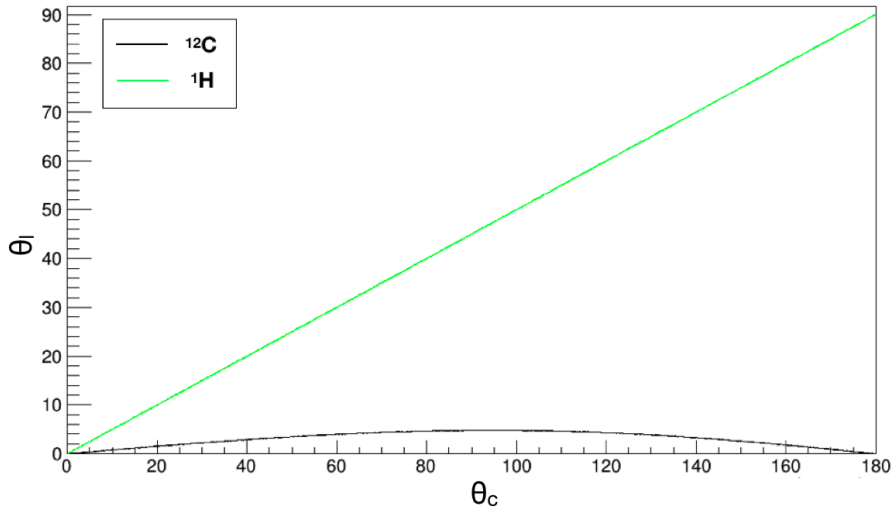

Figure 4.6. Distribution of the angle of scattering, θ_l, of the proton and of the carbon in the laboratory system versus the angle in the center of mass, θ_c.

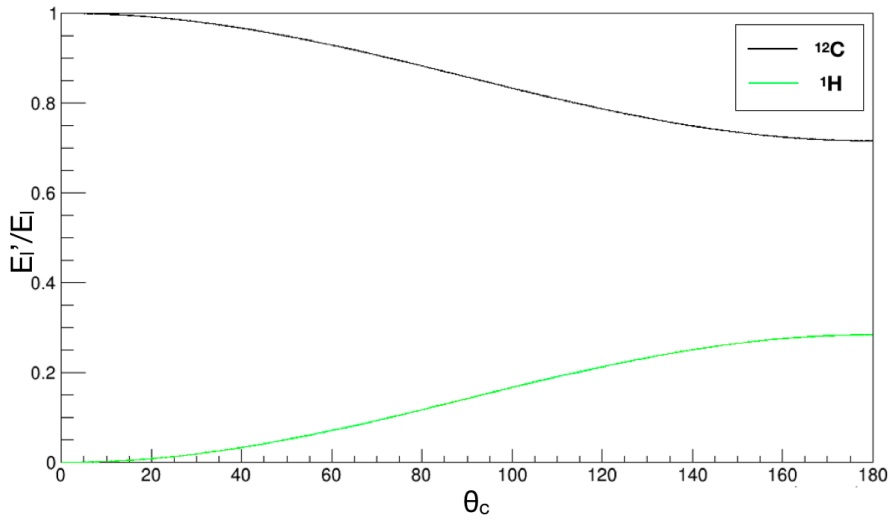

Figure 4.7. Distribution of the fraction of energy lost and gain after the elastic event, respectively by the carbon ion and by the proton in the laboratory system versus the angle in the center of mass, θ_c.

Since the kinetic energy, E, depends on the mass of the ion and its square velocity, this equation is equivalent to write:

$$E'_l = \frac{A^2 + 1 + 2Acos\theta_c}{(A+1)^2} E_l = \frac{1}{2}[(1+\alpha) + (1-\alpha)cos\theta_c]E_l, \tag{4.13}$$

where $\alpha = \frac{(A-1)^2}{(A+1)^2}$. The mean energy of the carbon ion after the collision is:

$$\bar{E}'_l = \frac{1}{2}E_l(1+\alpha) \simeq 0.86E_l. \tag{4.14}$$

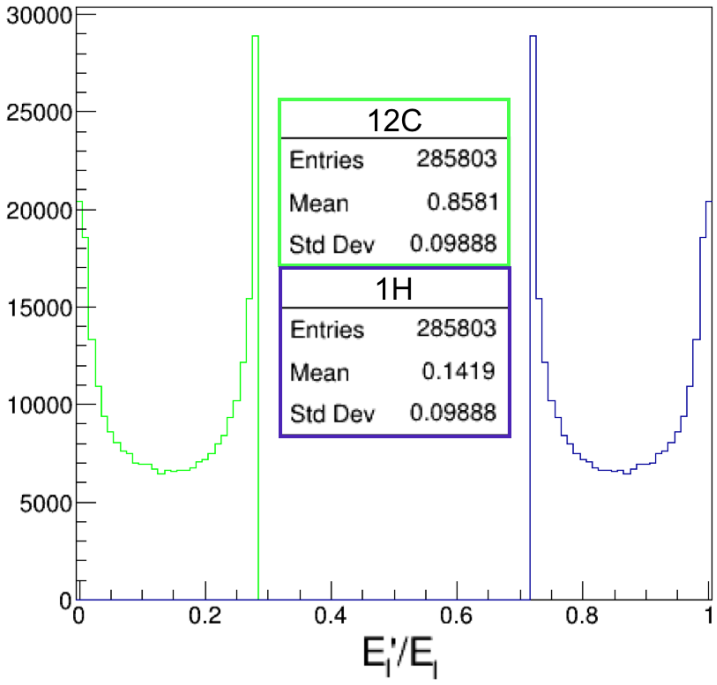

Figure 4.8. Fraction of energy loss and gain by the proton (green) and the carbon ion (blue) respectively. The result has been obtained by observing particles escaping from a thin target of hydrogen crossed by a carbon ion beam in a FRED simulation with the non-elastic event switched off. Primary carbon ions which were not affected by the elastic event have not been represented in the plot.

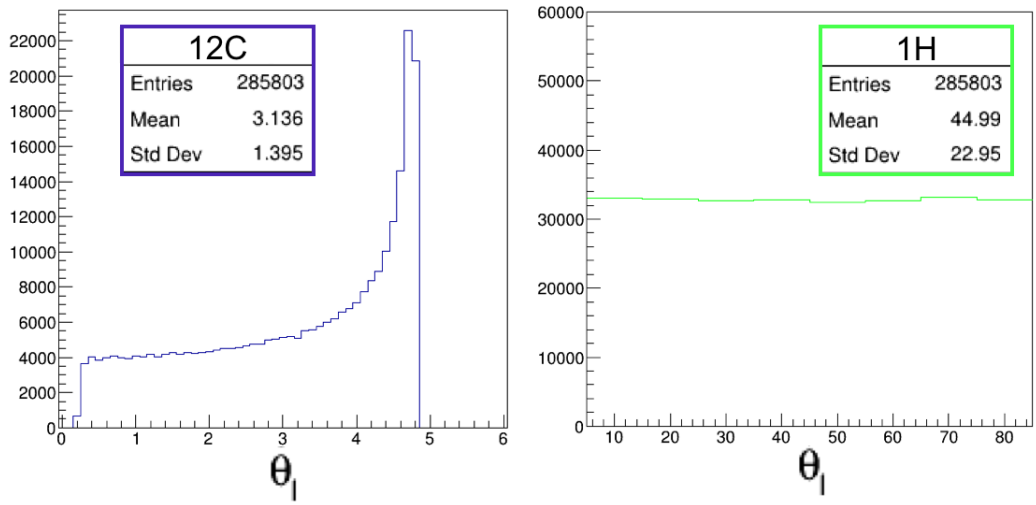

Figure 4.9. Scattering angle due to an elastic event for the proton (right) and the carbon ion (left) respectively. The result has been obtained by observing particles escaping from a thin target of hydrogen crossed by a carbon ion beam in a FRED simulation with the non-elastic event switched off. Primary carbon ions which were not affected by the elastic event have not been represented in the plot.

Similarly, in the laboratory system the energy of the new proton, E_l^p, scattered due the collusion is:

$$E_l^p = \frac{2AE_l}{(A+1)^2}(1 - cos\theta_c), \tag{4.15}$$

with a mean of $\bar{E}_p = 0.14E_l$. As it is possible to observe in Fig. 4.7, the energy lost by the carbon ion is given to the proton.
In Fig. 4.8 and Fig. 4.9, the angle and energy distributions of protons and carbon ion simulated with the FRED code and escaping from a thin hydrogen target is shown. The carbon ions not scattered are not considered in the plot.
Those distributions are in agreement with the model described. In particular, the distributions of the fraction of energy loss and gain by the proton and the carbon ion, respectively, are symmetric. The mean value is 0.14 for protons and 0.86 for carbon ions as expected. The mean of the angle of scattering of the carbon ion is 3° while the angle distribution of new protons is flat from 0 to 90 degrees.

4.3.3 Non-elastic cross-section

The non-elastic cross-section depends on the crossed material and on the type and energy incident particle. The cross-section of a nucleus projectile N_p (Fig. 4.10) interacting with a nucleus target N_t is obtained from a fit on existent data (papers of *Takechi* [89], *Zhang* [90] and *Kox* [91][92], Fig. 4.11) of carbon-carbon interaction and then scaled if the target is not carbon:

$$\sigma(N_p, N_t, E) = K(N_p, N_t, E)(1 - e^{\frac{E}{E_c}})(p_0 + p_1 E + e^{p_2 - p_3 E)}), \tag{4.16}$$

where E_c, p_0, p_1, p_2 and p_3 have been obtained from the fit and they are respectively 30 MeV, 762 mb, 1.4×10^{-3} mb MeV^{-1}, 6.719 and 1.34×10^{-3} MeV^{-1}.
$K(A_p, A_t, E)$ is the factor which is necessary to take in account different projectiles and different targets. In particular, the scaling has been obtained using the energy-dependent Kox formula [105][106] of total cross-section σ_K for nucleus-nucleus reactions:

$$K(N_p, N_t, E_{cm}) = \frac{\sigma_K(N_p, N_t, E_{cm})}{\sigma_K(^{12}C, ^{12}C, E_{cm})}. \tag{4.17}$$

Where $\sigma_K(^{12}C, ^{12}C, E_{cm})$ is Kox's cross-section considering a projectile of carbon ion and a carbon target, while $\sigma_K(N_p, N_t, E_{cm})$ is the Kox's cross-section for a nucleus projectile N_p on a nucleus target N_t.
The Kox formula is based on the strong absorption model and it expresses the total reaction cross-section in terms of the interaction radius R_{int}, the nucleus-nucleus interaction barrier B_c and the center-of-mass energy of the colliding system E_{cm}:

$$\sigma_K(N_p, N_t, E_{cm}) = \pi R_{int}^2 \left[1 - \frac{B_c}{E_{cm}}\right], \tag{4.18}$$

where the Coulomb barrier B_c of the projectile-target system is given by:

$$B_c = \frac{Z_t Z_p e^2}{r_c(A_t^{1/3} + A_p^{1/3})}, \tag{4.19}$$

where $r_c = 1.3$ fm, e is the electron charge and A_t, A_p, Z_t and Z_p are the mass and atomic numbers of the target and of the projectile nuclei.

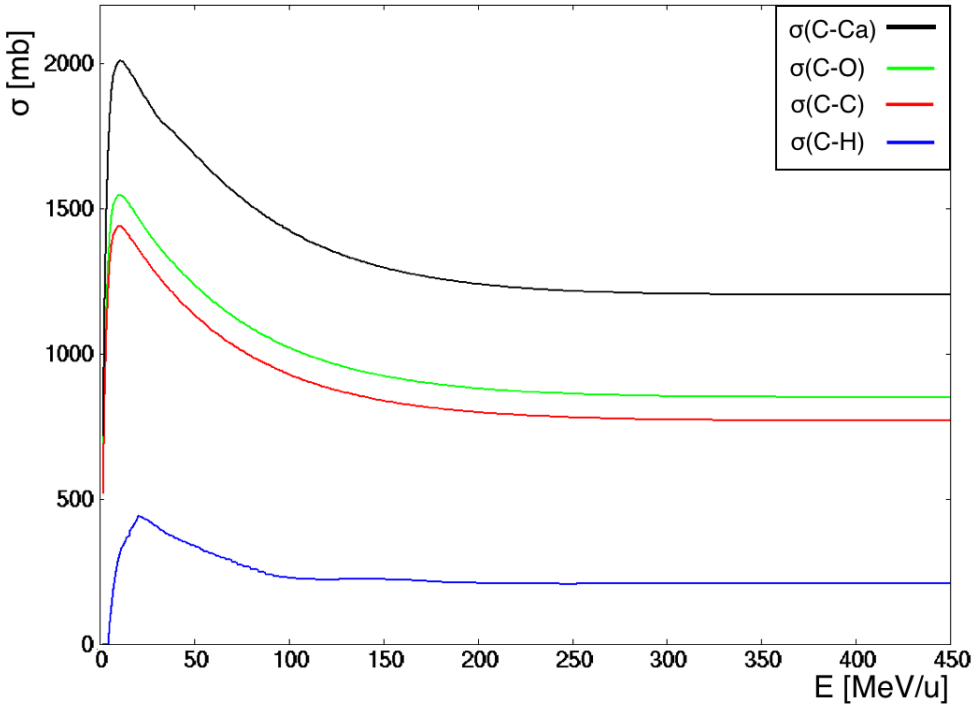

Figure 4.10. Cross-sections of a beam of carbon ion on different targets: calcium (black), oxygen (green), carbon (red), hydrogen (blue). Each cross-section has been obtained as described by Eq. 4.16 with the excepiton of the hydrogen target (Fig. 4.12).

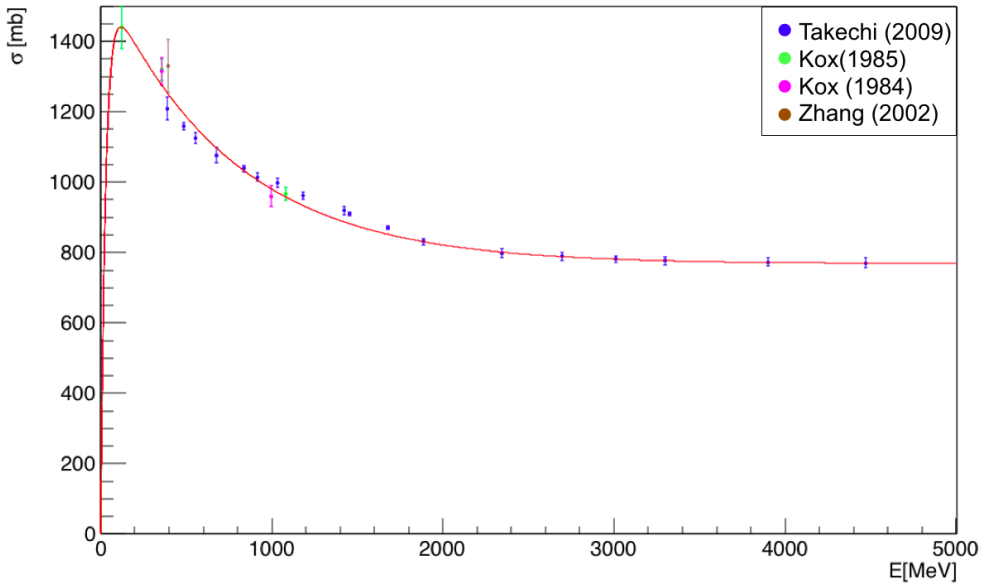

Figure 4.11. Cross-section of fragmentation of a carbon-carbon interaction in the energy range of interest for hadron therapy. In red the fit on data from papers of *Takechi* [89], *Zhang* [90] and *Kox* [91][92].

The interaction radius R_{int} is divided in a volume and a surface terms:

$$R_{int} = R_{vol} + R_{surf}, \tag{4.20}$$

$$R_{vol} = r_0(A_t^{1/3} + A_p^{1/3}), \tag{4.21}$$

$$R_{surf} = r_0 \left[a \frac{A_t^{1/3} A_p^{1/3}}{A_t^{1/3} + A_p^{1/3}} - c \right] + D. \tag{4.22}$$

$r_0 = 1.1$ fm and $a = 1.85$. The energy dependent term c is calculated using the analytical function:

$$c = -\frac{10}{x^5} + 2.0, \quad \text{if} \quad x \geq 1.5; \tag{4.23}$$

$$c = (-\frac{10}{x^5} + 2.0) \times \left(\frac{x}{1.5}\right)^3, \quad \text{if} \quad x < 1.5;$$

$$x = \log_{10}(E_k),$$

where E_k is the projectile kinetic energy in MeV/u in the laboratory system.

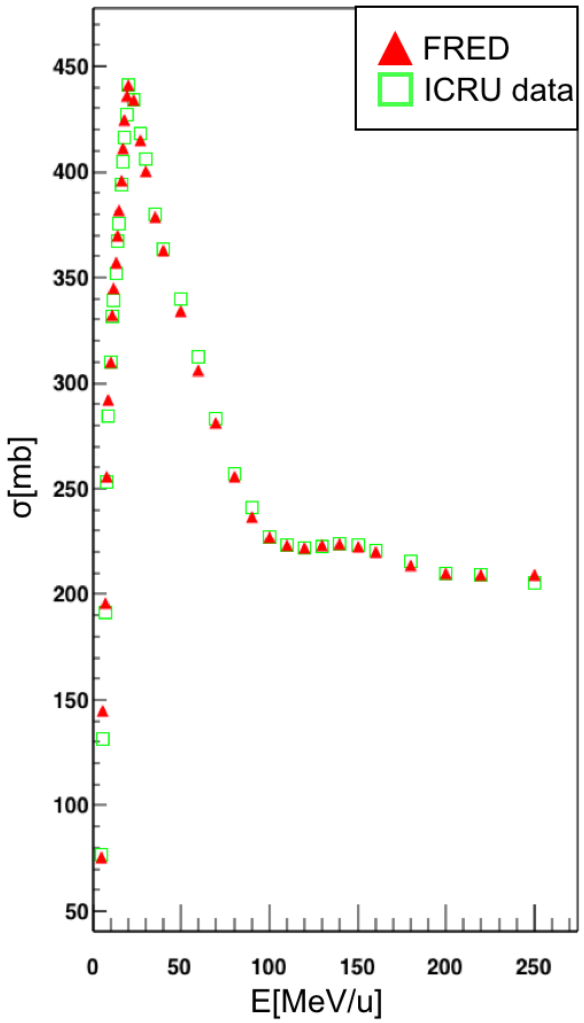

Figure 4.12. Cross-section of fragmentation of a carbon-hydrogen interaction in the energy range of interest for hadron therapy. With the red triangles, the cross-section obtained with FRED through a fit on data (green squares) is shown [107].

The neutron-excess D is given by the formula:

$$D = \frac{5(A_t - 2Z_t)Z_p}{A_p A_t}. \tag{4.24}$$

This scaling law is used for every nucleus of the target except for carbon and hydrogen. For hydrogen target the cross-section has been computed using data from ICRU (*International Commission on Radiation Units & Measurements*) [107]. The comparison between data and FRED is shown in Fig. 4.12.
The difference between using directly the Kox's formula or using it just to correct the cross-section of the carbon target has been estimated within the 1.5% in the energy range of interest as can be observed in Fig. 4.13.

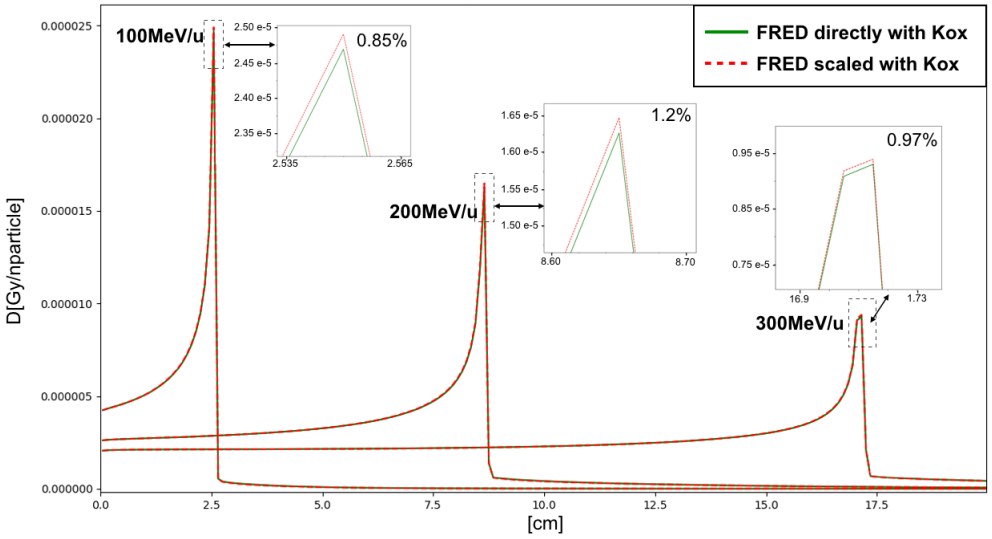

Figure 4.13. Longitudinal integrated dose for carbon ion beams in water at different energies. The dose is relative to one primary particle but the simulation has been run with statistics of about 10^6 histories. Comparison between using directly Kox formula (green) and using it just to correct the mass attenuation of C-C (red), with the same scoring grid, and the same statistic is presented. The inserts show the peak details and the value of the percent difference.

The fragmentation of secondary particles has been also implemented. Their cross-section is computed directly using the Kox formula (Eq. 4.18).

4.3.4 Fragmentation model

The nuclear fragmentation process is not yet well understood from a theoretical perspective. Interactions between a projectile and atoms of the target are ultimately described by quantum electrodynamics (QED). Furthermore, nuclear interactions with fragmentation are many-body problems that defy present-day calculational methods at the most fundamental level. The particles that participate in nuclear interactions are themselves composites (nuclei contain nucleons, and nucleons contain quarks and gluons), and the fundamental theory that describes these interactions is quantum chromodynamics (QCD), which is only tractable in the limit of interactions

with large momentum transfers. QCD has not yet been successfully applied to nucleus-nucleus collisions at the energies of interest in medical physics. The lack of a fundamental theory has led to the development of many semi-empirical models to describe nucleus-nucleus interactions, and considerable effort continues to be put into the development of these models and benchmarking them against the limited set of available pertinent data.
The model developed for the FRED code will be described in this paragraph and it is represented by the flowchart of Fig. 4.14.

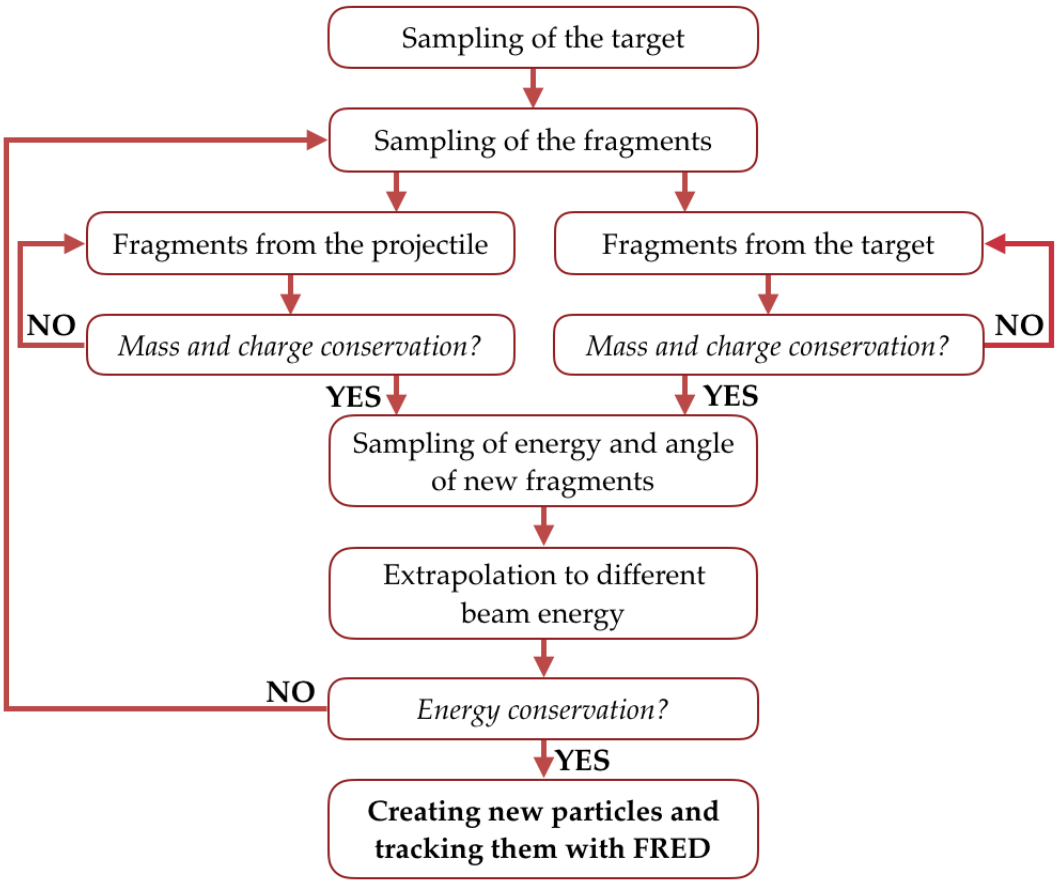

Figure 4.14. Flowchart of the fragmentation model in FRED.

After having sampled the target with which the projectile interacts, in the case of composite material, the fragments produced by the projectile and target fragmentation are sampled. Then, the first sampling of energy and angle of the secondaries is obtained using cumulative distributions and double differential cross-section in energy and angle from data of Ganil experiments [93][94][95]. Since those cumulative distributions have been obtained using a 95 MeV/u beam, the energies and angles of fragments have been scaled to consider each possible energy of incident particles. Mass, charge and energy conservation is checked during this procedure.
The fragmentation of secondary particles has been implemented too. The Kox's cross-section has been used for the total cross-section and the sampling of angle and energy is analogous to the one used for carbon fragmentation.

Sampling of the target

The first step to simulate the fragmentation process in a given medium made of many materials is the choice of the element of the target on which the fragmentation happens. FRED takes information from tables where a cumulative distribution is associated with each target used in the Ganil experiment and to each possible fragments emitted. So, to choose which combination of fragments will be emitted, it is necessary to know the exact target hit by the carbon ion.
To choose the target, again Kox's cross-section (Eq. 4.18) is used to construct a cumulative distribution in the following way:

$$P^i = \frac{n^i \sigma_K^i}{\sigma^{tot}}, \tag{4.25}$$

$$\sigma^{tot} = \sum_{j=0}^{j=N-1} n^j \sigma_K^j. \tag{4.26}$$

σ_K^{tot} is the sum of the cross-section of all the N elements of the phantom considering also the occurrence n of each element. For what concern hydrogen and carbon target, their cross-section from data is used. For example, for a water target it is:

$$P(H) = \frac{2\sigma_{data}^H}{\sigma^{tot}}, P(O) = \frac{\sigma_K^O}{\sigma^{tot}}, \tag{4.27}$$

$$\sigma^{tot} = 2\sigma_{data}^H + \sigma_K^O, \tag{4.28}$$

where σ_{data}^H and σ_K^O are respectively the cross-section of a hydrogen target, which is calculated through fit on data (Fig. 4.12), and Kox cross-section of an oxygen target, calculated using Eq. 4.18. The Kox cross-section can be represented as the probability that an incident particle has an interaction with a specific nucleus of the matter crossed. The code extracts a random number [0,1] to compare with the cumulative distributions in order to choose the target of the event.

Sampling of the fragments

After the choice of the target, the code reads tables containing the probabilities of emission for each possible fragment. Possible isotopes produced are: neutrons, ^{1}H, ^{2}H, ^{3}H,^{3}He, ^{4}He, ^{6}He, ^{6}Li, ^{7}Li, ^{7}Be, ^{9}Be, ^{10}Be, ^{8}B, ^{10}B, ^{11}B, ^{10}C, ^{11}C and ^{12}C. The probability tables have been obtained using an iterative formalism to have the same generating probability of the Ganil experiment. If the Ganil probabilities would be used directly for the fragments sampling, after the sampling procedure that will be described, the mass, charge and energy would not be conserved and the final fragments' distribution will be different from that one measured by Ganil. Considering N possible fragments that could be produced in the fragmentation, the probability of sampling a fragment, S_i, has been expressed as C^α with the constraint:

$$\sum_{i=0}^{N-1} S_i = \sum_{i=0}^{N-1} C^{\alpha_i} = 1, \tag{4.29}$$

$$\vec{\alpha} = log\vec{S}. \tag{4.30}$$

The same notation for the probability of sampling obtained in the Ganil experiment, P^{exp}, is:

$$\vec{Y}^{exp} = log\vec{P}^{exp}. \tag{4.31}$$

The sampling process has been considered as a function which, starting from the sampling probability S_i, produces generation probabilities Y_i at the end of the procedure:

$$\vec{Y} = f(\vec{\alpha}). \tag{4.32}$$

Of course the sampling procedure is statistical in nature. The Eq. 4.32 is related to the probabilities obtained after averaging on a sufficient number of the sampling procedure. The $\vec{Y}$ obtained should be equal to $\vec{Y}^{exp}$. It is possible to require that the equality between $\vec{Y}$ and $\vec{Y}^{exp}$ satisfied "as closely as possible" by minimizing the χ^2 statistic:

$$\chi^2 = \sum_{k=1}^{k=N} \frac{(Y_k^{exp} - Y_k)^2}{\sigma_k^2} = \sum_{k=1}^{k=N} \frac{(Y_k^{exp} - f_k(\alpha))^2}{\sigma_k^2}, \tag{4.33}$$

where N is the number of fragments. The values of α_i must be chosen so as to minimize χ^2.
It is possible to obtain σ_k, which is the uncertainty relative to Y_k^{exp}, looking Eq. 4.31 from which:

$$\sigma_k = \frac{\partial Y_k^{exp}}{\partial P_k^{exp}} \sigma_k^{exp}, \tag{4.34}$$

where σ_k^{exp} are the experimental uncertainties associated to the probability of producing a fragment k measured by the Ganil experiment. Knowing that $\partial Y_k^{exp}/P_k^{exp} = 1/P_k^{exp}$, Eq. 4.34 can be express also as:

$$\sigma_k = \frac{\sigma_k^{exp}}{P_k^{exp}}. \tag{4.35}$$

The requirement that the χ^2 function be at a minimum is usually guaranteed by:

$$\frac{\partial \chi^2}{\partial \alpha_i} = 0. \tag{4.36}$$

Unfortunately, no general method exists for solving these equations since $f_k(\alpha)$ and its first derivatives can, in general, be highly nonlinear functions of the parameters α_i. So, to minimize χ^2, it is necessary to define two matrices and expand to first order the function $f(\alpha)$. The first matrix is the matrix of coefficients:

$$A_{ij} = \frac{\partial Y_i}{\partial \alpha_j}, \tag{4.37}$$

which describes as the logarithm of the generation probability changes with the logarithm of the sampling probability. The matrix A_{ij} has been calculated by a MC code, increasing by $\partial\alpha$ the parameters $\vec{\alpha}$ and evaluating the variation of $\vec{dY}$ observing values of $\vec{Y}$. A critical part in computing this derivative matrix with MC evaluation is chosen an adequate statistic. We took care that the minimization results remain stable with respect to the statistic used to compute the A derivative matrix.

The second matrix is the inverse of the measurement covariance matrix, called weight matrix:

$$V_{ij}^{-1} = \frac{1}{\sigma_{ij}^2}. \tag{4.38}$$

The functions $\vec{Y} = f(\vec{\alpha})$ vary slowly enough so that one can expand to first order about an approximate solution:

$$\vec{Y}_{i+1} = \vec{Y}_i + \vec{A}\vec{\eta}_i, \tag{4.39}$$

where $\eta_i = \alpha_i - \alpha_{iA}$. Under this approximation, the χ^2 function can be written as:

$$\chi^2 = (\Delta\vec{Y} - \vec{A}\vec{\eta})^T \vec{V}_y^{-1} (\Delta\vec{Y} - \vec{A}\vec{\eta}). \tag{4.40}$$

It can be proved that the parameters η_i obtained by minimizing χ^2 function are unbiased and have minimum variance σ_i^2.
Taking the partial derivative with respect to the parameters η one obtains the equations:

$$\vec{A}^T \vec{V}_y^{-1} (\Delta\vec{Y} - \vec{A}\vec{\eta}) = 0, \tag{4.41}$$

which can be written as:

$$\vec{A}^T \vec{V}_y^{-1} \vec{A}\vec{\eta} = \vec{A}^T \vec{V}_y^{-1} \Delta\vec{Y}. \tag{4.42}$$

Defining $\vec{V}_A = (\vec{A}^T \vec{V}_y^{-1} \vec{A})^{-1}$, it is possible to express the $\vec{\eta}$ equations as:

$$\vec{\eta} = \vec{V}_A \vec{A}^T \vec{V}_y^{-1} \Delta\vec{Y}. \tag{4.43}$$

The parameters α, used for built the input cumulative for the code, have been determined from the equation $\alpha = \alpha_A + \eta$.
In Tab. 4.1, results of the iterative procedure, per isotope and for each elemental target, are shown in comparison with the probabilities obtained in the Ganil experiment. The iterative procedure has been used for all the targets of Ganil except for the hydrogen target.
As it is possible to observe in the table, considering a hydrogen target in the Ganil experiment, there is no information about the distributions for fragments heavier than ^{7}Be. For this reason, the code uses for the carbon ion fragmentation on hydrogen target cumulatives obtained from a FLUKA simulation. Moreover, in FRED also the probability of obtaining a neutron, absent in the Ganil data, has been computed.
Outgoing particles from a heavy-ion fragmentation reaction are typically described as either "projectile" fragments or "target" fragments. In the Ganil experiment, both types of fragments have been detected and it was impossible to distinguish them. So both phenomena have to be taken into consideration using the cumulative distributions. For the carbon ion projectile fragmentation, the probabilities are scaled to avoid the ^{12}C isotope as projectile's product since it would be only a scattered projectile. Regarding hydrogen target fragmentation there is only the production of a single proton.
For each event, FRED extracts random numbers to choose, through the cumulative distributions previously described, fragments produced by the projectile until the sum of mass and charge of all fragments is equal to the mass and the charge of the projectile. The same procedure is used for the target fragmentation, this time conserving the mass and the charge of the target. As highlighted before, if the target is a hydrogen ion, the fragmentation of the target will have as a product only a

proton.
In Fig. 4.15, the flowchart of the sampling of projectile's and target's fragments is shown. Once having the complete set of fragments, the energy and angle sampling is computed as described in the following sections. If the sum of the energy of all projectile's and target's fragments is greater than the energy of the projectile, the code extracts a new set of fragments until mass, charge and energy are conserved. The most frequent fragments are neutrons, protons, deuterium and Helium-4 followed by the lighter fragments. Some of those isotopes are unstable but actually, the β^+ decay is not yet considered in the code but it will be implemented in FRED in the near future.

Table 4.1. Production probabilities per isotope and for each elemental target reported in the Ganil experiment [93] and built for the code FRED.

	Probabilities [%] Target					
Frag.	**(Ganil) H**	**(Fred) H**	**(Ganil) C**	**(Fred) C**	**(Ganil) O**	**(Fred) O**
n	-	13.8	-	65.3	-	59.8
^{1}H	52(8)	37.6	35(2)	10.2	38(4)	15.8
^{2}H	9(2)	5.0	16.3(0.8)	7.5	17(1)	8.8
^{3}H	2.0(0.4)	1.3	6.6(0.4)	6.1	6.5(0.7)	5.1
^{3}He	5.2(0.5)	3.0	7(1)	1.2	7.2(0.9)	1.7
^{4}He	25(10)	25.8	25(6)	6.4	22(7)	6.3
^{6}He	1.3(0.1)	$3.6\cdot10^{-2}$	1.0(0.2)	1.7	1.0(0.4)	1.0
^{6}Li	1.5(0.8)	2.3	1.4(0.2)	$2.5\cdot10^{-1}$	1.3(0.3)	$2.8\cdot10^{-1}$
^{7}Li	1.0(0.2)	$9.3\cdot10^{-1}$	1.2(0.2)	$4.1\cdot10^{-1}$	1.2(0.3)	$3.9\cdot10^{-1}$
^{7}Be	2.0(0.4)	1.6	1.0(0.2)	$8.3\cdot10^{-2}$	1.0(0.2)	$1.2\cdot10^{-1}$
^{9}Be	-	$2.5\cdot10^{-1}$	$4(1)\cdot10^{-1}$	$1.1\cdot10^{-1}$	$3.4(0.7)\cdot10^{-1}$	$7.9\cdot10^{-2}$
^{10}Be	-	$1.0\cdot10^{-4}$	$1.8(0.4)\cdot10^{-1}$	$2.4\cdot10^{-1}$	$1.9(0.5)\cdot10^{-1}$	$1.0\cdot10^{-1}$
^{8}B	-	$1.5\cdot10^{-1}$	$1.3(0.4)\cdot10^{-1}$	$1.3\cdot10^{-2}$	$1.2(0.5)\cdot10^{-1}$	$1.4\cdot10^{-2}$
^{10}B	-	1.3	$10(3)\cdot10^{-1}$	$8.9\cdot10^{-2}$	$9(6)\cdot10^{-1}$	$8.6\cdot10^{-2}$
^{11}B	-	2.1	1.2(0.5)	$2.0\cdot10^{-1}$	1(1)	$1.8\cdot10^{-1}$
^{10}C	-	$1.9\cdot10^{-1}$	$1.7(0.6)\cdot10^{-1}$	$1.7\cdot10^{-2}$	$1.5(0.9)\cdot10^{-1}$	$1.6\cdot10^{-2}$
^{11}C	-	3.9	1.1(0.4)	$5.5\cdot10^{-2}$	1.0(0.7)	$7.1\cdot10^{-2}$
^{12}C	-	$5.9\cdot10^{-1}$	1.6(0.9)	$4.3\cdot10^{-2}$	1.5(0.9)	$7.9\cdot10^{-2}$

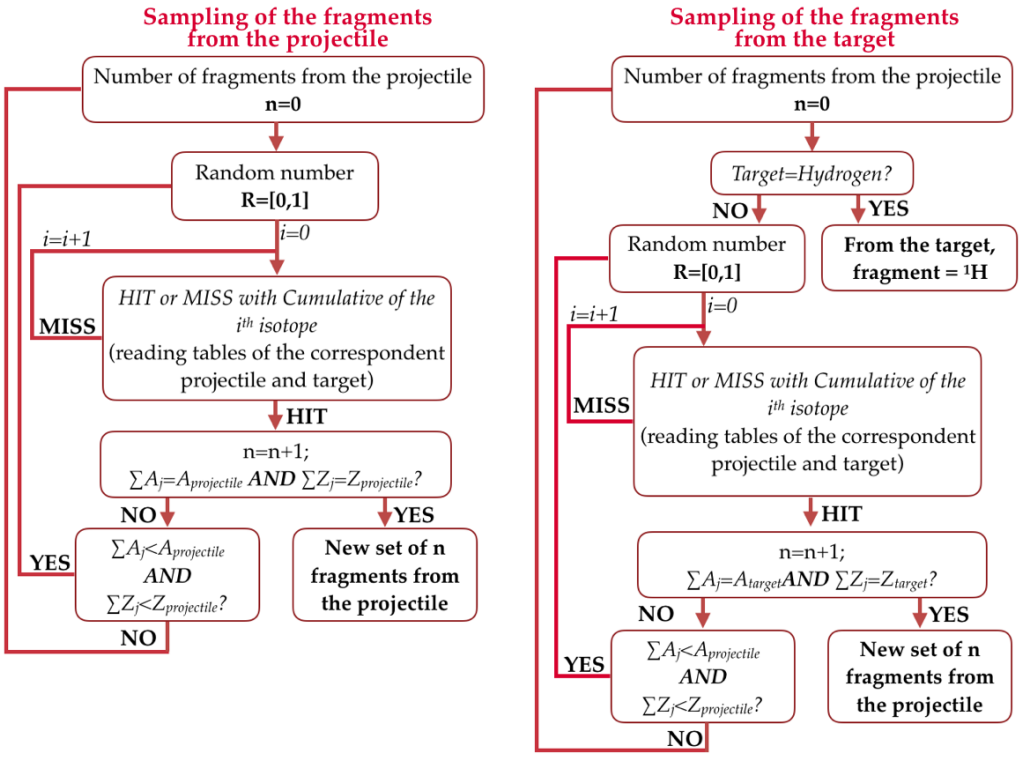

Figure 4.15. Flowchart of the fragments' sampling in FRED. $\sum A_j$ and $\sum Z_j$ are respectively the sum of the mass and the charge of the fragments already extracted in the event.

Lorentz transformation for projectile and target fragmentation

When a projectile particle with a velocity v interacts with a fixed target, fragments of the projectile and the target have different angular and energy distributions. The first has almost the same energy per nucleons of the projectile and is emitted forward mostly with small angles. The fragments of the target have low energies and their distributions in the space are more isotropic. As already observed, in the Ganil data there are no distinctions between those fragments. However, to understand how to correctly simulated the fragmentation of projectile and target using existent data, it is possible to make some relativistic considerations in the kinematic.
The projectile particles employed in particle therapy proceed at relativistic velocities and, consequently, the interaction with the target takes place in the same relativistic condition. Using the inverse kinematics approach it is possible to switch from the laboratory reference system to the one of the projectile. In this system, the projectile is fixed and it observes the target moving in its direction with the same energy as the projectile in the laboratory system. Projectile and target are switched and, in this reference system, the target's fragments will have the same energy and angle distributions as the projectile's fragments in the laboratory system. To switch from the laboratory system to the projectile system, Lorentz transformation is needed as shown in Fig. 4.16.
Golovkov and Matsufuji [108][109] observed that, to describe the energy and angular distribution of secondary fragments, a Gaussian and exponential distribution are needed. The first can describes the nature of fragments produced by the projectile,

while the exponential distribution is the representation of particles produced by the target fragmentation.
As proof of this double nature of the distribution, it has been observed that taking the Gaussian component of the energy distribution and applying a Lorentz transformation, an exponential distribution is obtained.

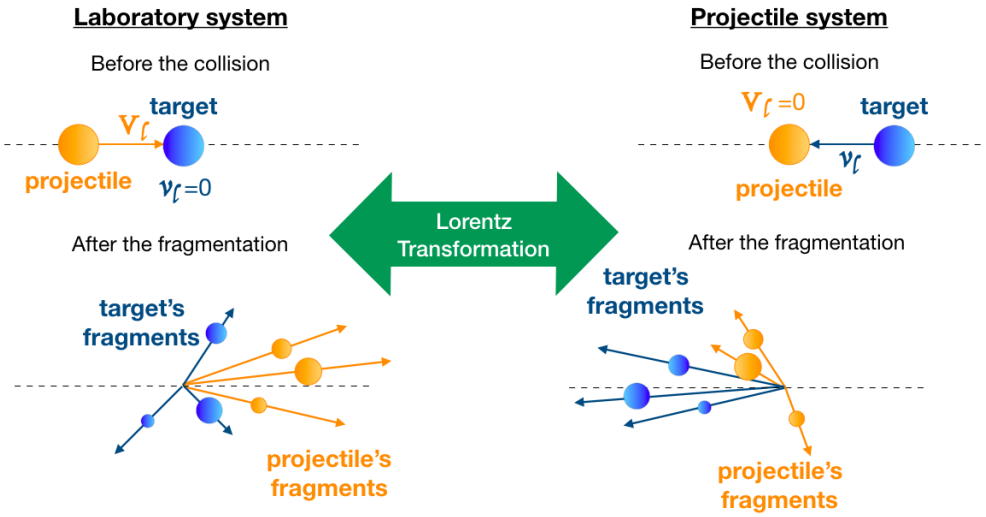

Figure 4.16. Schematic view of the collision (top) and fragmentation (bottom) between a projectile and a fixed target from the point of view of the laboratory (left) and of the projectile (right).

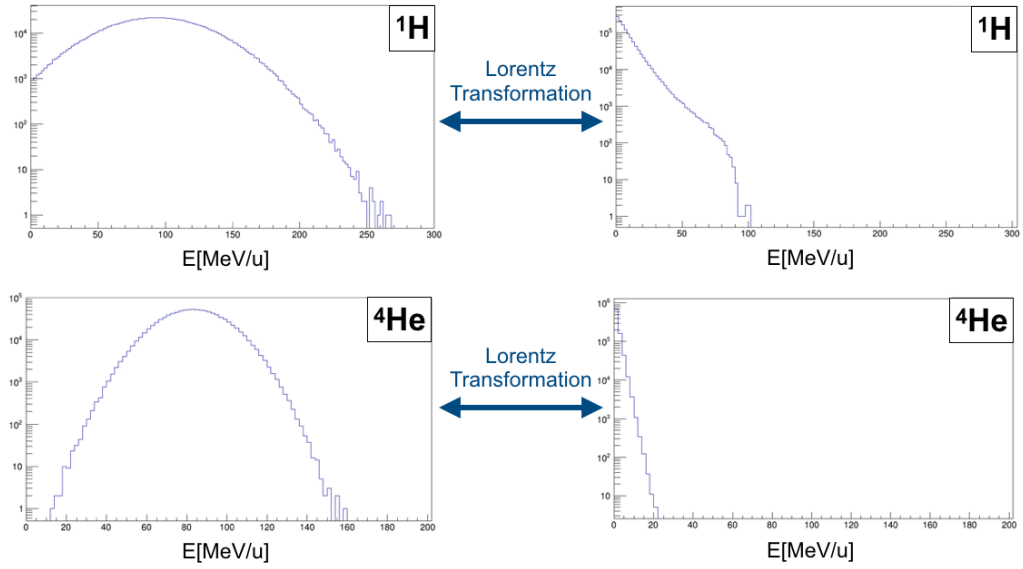

Figure 4.17. Gaussian distribution of kinetic energy of ^{1}H (top, left) and ^{4}He (bottom, left) fragments extrapolated by Ganil data is shown. Applying a Lorentz transformation to shift from the laboratory reference system to the one of the projectile, exponential distributions (right) are obtained.

In Fig. 4.17 an example of the application of the Lorentz transformation on Ganil data is shown. It has been applied to the Gaussian distribution of hydrogen and 4-helium fragments extrapolated from Ganil data. The results are exponential distributions, as expected. This is in agreement with considering the fragmentation of the target as if it were the fragmentation of the incident particle in the reference system of the projectile.

Sampling of energy and angular distribution

As observed in the previous section, to sample angle and energy of emission it is necessary to treat the projectile and target fragmentation separately. Projectile fragments approximately keep the direction and velocity of the incident particle. Target fragments are instead emitted more or less isotropically in the laboratory frame, and have relatively low energies, on the order of tens of MeV or less. In Fig. 4.18, Fig. 4.19 and Fig. 4.20, it is possible to observe an example of energy and angle distribution, in linear and logarithmic scale, of six types of fragments, hydrogen, helium-4, lithium-6, beryllium-7, boron-11 and carbon-11, detected in the Ganil experiment after the interaction of a carbon ion with a hydrogen, carbon and oxygen target respectively.
In the experiment, the detection angle was between 4° and 43° and energy threshold was fragment-dependent (from 4 MeV for ^{1}H to 86.9 MeV for ^{12}C).
As expected, bidimensional fits show that the distribution is composed of a Gaussian and an exponential function:

$$f(E,\theta) = A_1 e^{\alpha_E E + \alpha_\theta \theta} + A_2 e^{-\left(\frac{(E-<E>)^2}{2\sigma_E} + \frac{(\theta-<\theta>)^2}{2\sigma_\theta}\right)}, \tag{4.44}$$

where A_1, A_2, α_E, α_θ, σ_E, σ_θ, $< E >$ and $< \theta >$ are the parameters described in Tab. 4.2, Tab. 4.3 and Tab. 4.4 for hydrogen, carbon and oxygen target respectively. This double nature has been already described in the previous section and proved to apply a Lorentz transformation to the Gaussian component obtaining the exponential one.
The Gaussian distribution is due to the fragments produced by the projectile. The produced fragments have energy per nucleon on average equal to the projectile (in this case 95 MeV/u) and their direction is peaked at zero degrees. The exponential distribution, on the other hand, is the representation of detected particles produced by the target fragmentation. Their angular distribution is almost isotropic and the energy is smaller than the energy of the projectile fragments. The heavier the fragments are, the more important the contribution of the Gaussian term is.
Since the fragments hydrogen (^{1}H, ^{2}H and ^{3}H) have no strong difference from the Gaussian and the exponential distribution, for those particles the energy and the angle of emission are extracted directly by Eq. 4.44. All other fragments are extracted by the Gaussian and the exponential distribution in case of a projectile and target fragmentation respectively.
For hydrogen target (Fig. 4.18 and Tab. 4.2), with the exception of the fragment ^{1}H, all the distributions are predominately Gaussian. This is because the target fragmentation has as a product only a proton. There is also a small exponential contribution because the double cross-section of hydrogen target has been obtained by combining the cross-sections of CH_2 and C targets.
The fit parameters for each produced fragment and each target have been collected in files read by the code. The distribution fitted in the experimental angular range [4°;43°] is extrapolated to the [0°;180°] range in the angular sampling.

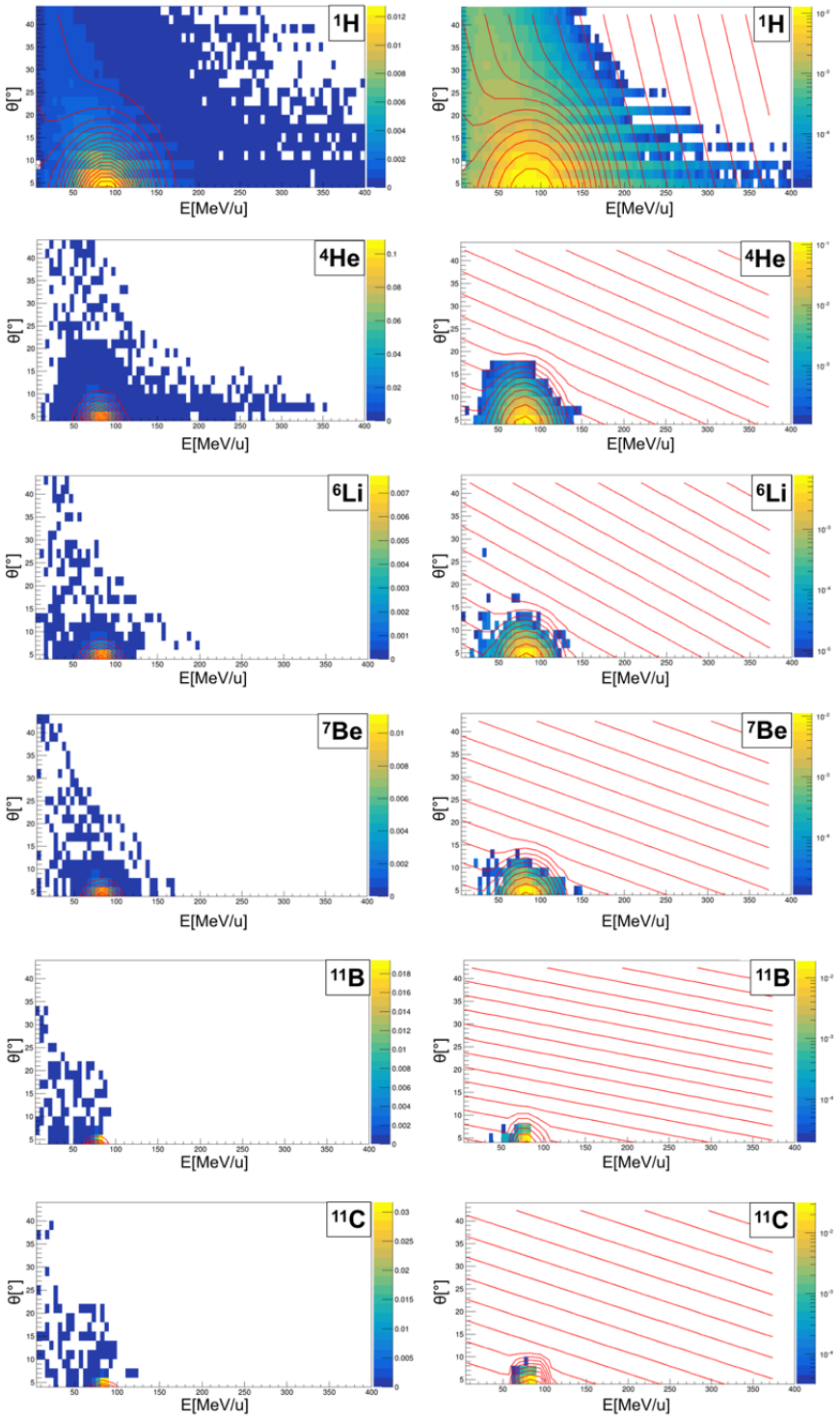

Figure 4.18. Bidimensional fits on energy and angular distribution of different fragments produced by a carbon ion beam interacting with an **hydrogen target**. The color maps represent data taken from the Ganil experiment in linear (left) and logarithmic (right) scale.

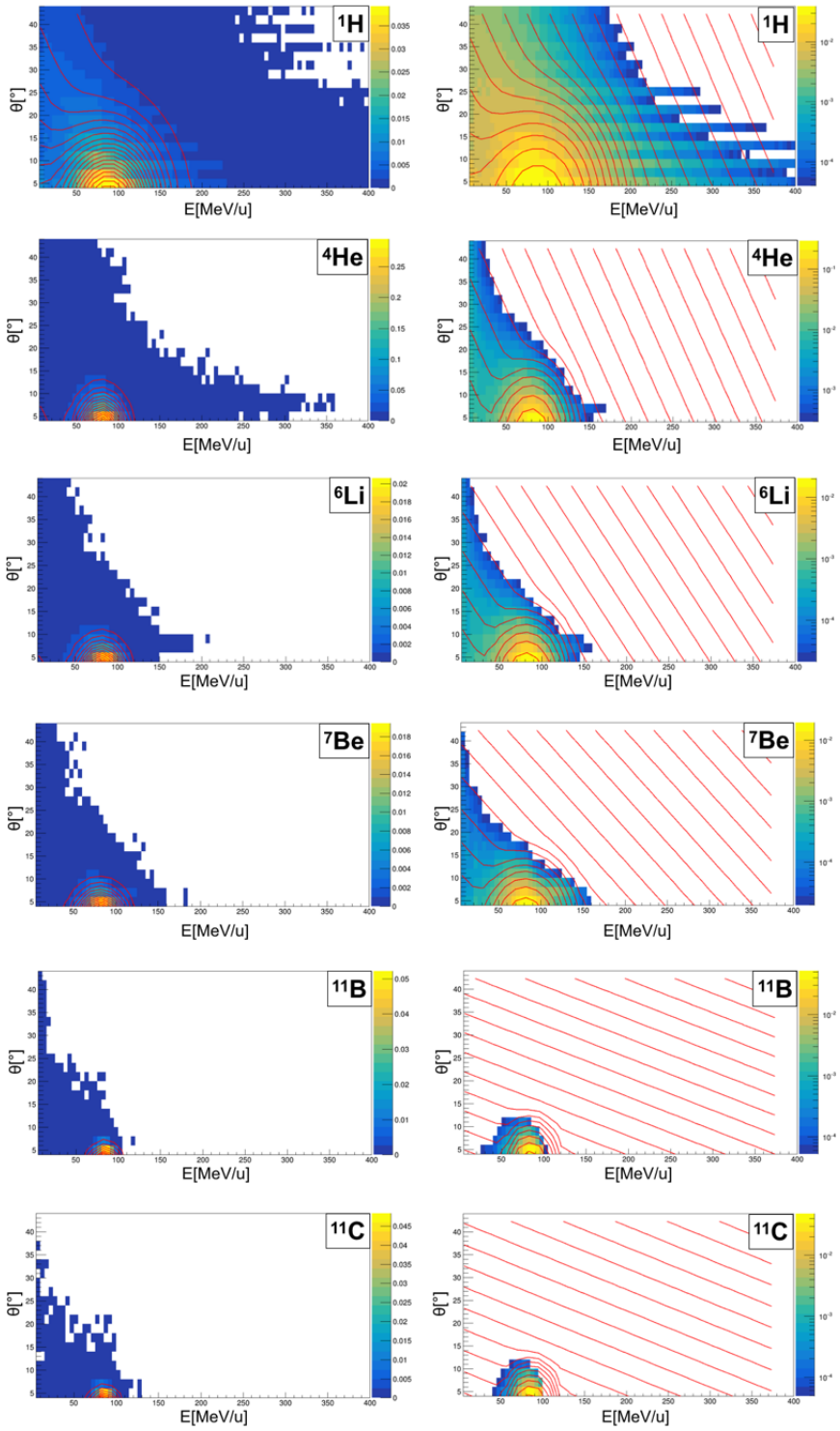

Figure 4.19. Bidimensional fits on energy and angular distribution of different fragments produced by a carbon ion beam interacting with an **carbon target**. The color maps represent data taken from the Ganil experiment in linear (left) and logarithmic (right) scale.

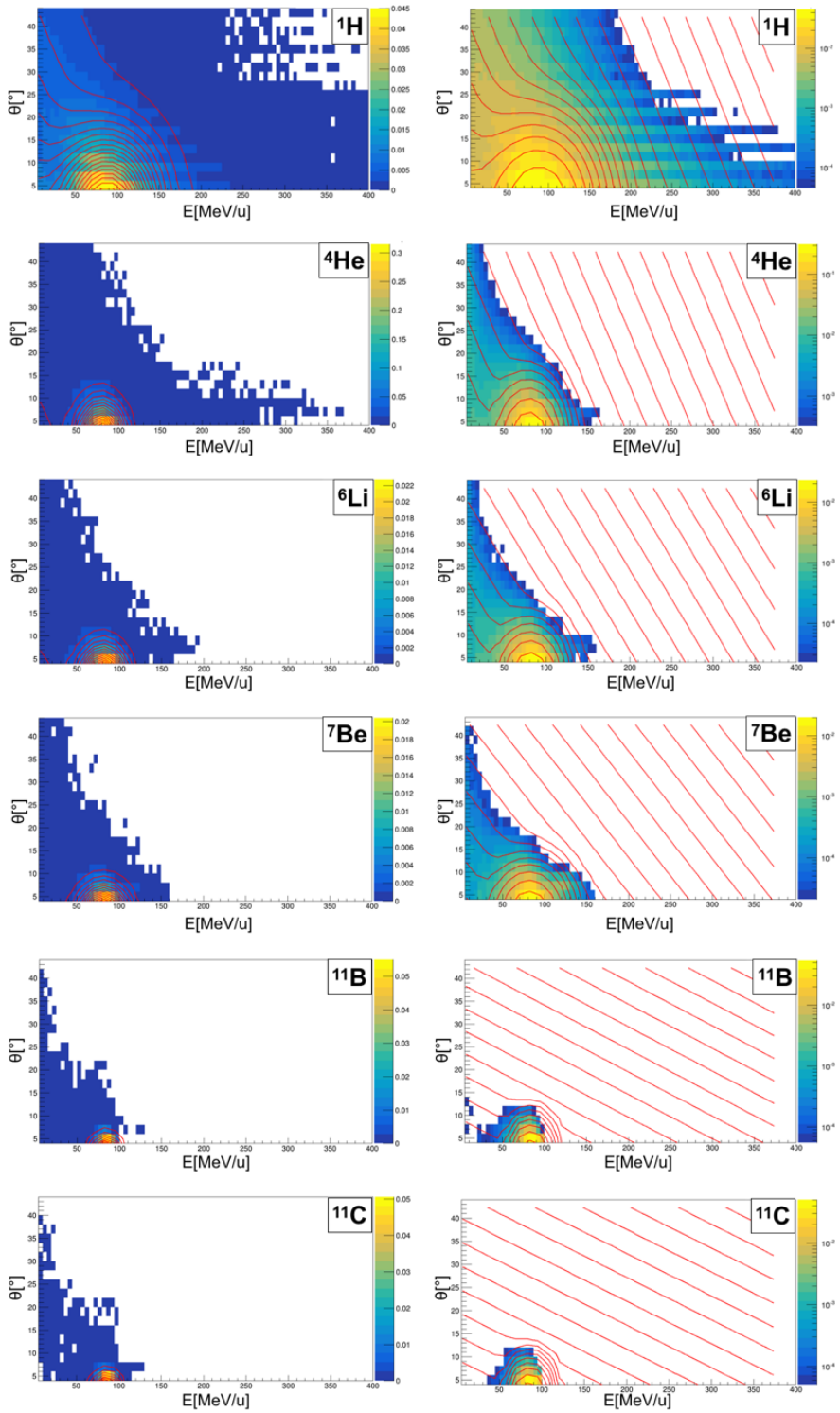

Figure 4.20. Bidimensional fits on energy and angular distribution of different fragments produced by a carbon ion beam interacting with an **oxygen target**. The color maps represent data taken from the Ganil experiment in linear (left) and logarithmic (right) scale.

Table 4.2. Parameters of Eq. 4.44 considering a ^{1}**H target**. Parameters relative to the energy, E, are expressed in MeV/u while the one of the angle, θ, in degrees.

Frag.	A_1	A_2	$< E >$	σ_E	$< \theta >$	σ_θ	α_E	α_θ
n	0.5409	48.6946	93.3897	33.1828	0.0	9.7138	0.0124	0.0248
^{1}H	0.5409	48.6946	93.3897	33.1828	0.0	9.7138	0.0124	0.0248
^{2}H	0.2033	7.5260	81.2426	23.4388	0.0	8.1707	0.0217	0.0651
^{3}H	0.0778	2.7494	76.2226	22.3735	0.0	6.8534	0.0187	0.1789
^{3}He	0.0221	7.6324	96.3748	27.32723	0.0	6.2396	0.0184	0.1021
^{4}He	0.0098	56.2280	84.2701	12.5399	0.0	4.3505	0.0146	0.1806
^{6}He	0.0307	2.9958	78.1432	14.1271	0.0	4.0472	0.0265	0.2677
^{6}Li	0.0080	4.5023	83.9703	11.0424	0.0	3.3969	0.0189	0.2046
^{7}Li	0.0189	3.3570	79.4284	8.6018	0.0	3.2167	0.0206	0.2673
^{7}Be	0.0036	6.6109	85.3822	10.8934	0.0	3.1464	0.0174	0.2061
^{9}Be	0.0244	1.2818	81.9535	7.2637	0.0	3.0079	0.0228	0.2702
^{10}Be	0.0708	0.3859	79.3767	5.3369	0.0	3.1237	0.0243	0.3191
^{8}B	0.6343	0.0083	88.7019	13.3256	0.0	3.1867	0.0219	0.1591
^{10}B	0.0035	12.75	83.4003	6.4979	0.0	2.4278	0.0192	0.3752
^{11}B	0.0113	12.7649	83.0822	4.5976	0.0	2.1625	0.0185	0.5795
^{10}C	0.0012	3.6813	88.1944	7.1769	0.0	2.3438	0.0178	0.2128
^{11}C	0.0005	38.7737	84.4791	4.7855	0.0	2.0613	0.0167	0.2982
^{12}C	0.0005	93.2853	83.3388	3.4748	0.0	0.9169	0.01000	0.2053

Table 4.3. Parameters of Eq. 4.44 considering a ^{12}**C target**. Parameters relative to the energy, E, are expressed in MeV/u while the one of the angle, θ, in degrees.

Frag.	A_1	A_2	$< E >$	σ_E	$< \theta >$	σ_θ	α_E	α_θ
n	0.2821	105.6752	93.3816	36.6146	0.0	10.1856	0.0126	0.0256
^{1}H	0.2821	105.6752	93.3816	36.6146	0.0	10.1856	0.0126	0.0256
^{2}H	0.2670	54.0336	81.3329	25.7878	0.0	8.9456	0.0257	0.0313
^{3}H	0.2562	24.7267	73.2173	18.3609	0.0	7.5951	0.0316	0.0575
^{3}He	0.1485	36.5737	91.7603	29.3516	0.0	7.0407	0.0312	0.0473
^{4}He	0.0740	194.4721	83.1849	15.0985	0.0	5.2059	0.0286	0.0802
^{6}He	0.0812	10.1259	78.5499	17.0086	0.0	5.3707	0.0302	0.1549
^{6}Li	0.0696	13.4980	84.0736	14.5693	0.0	4.4146	0.0275	0.1091
^{7}Li	0.0614	13.3967	78.9078	12.8347	0.0	4.2399	0.0308	0.1227
^{7}Be	0.0374	12.0704	83.5043	16.2560	0.0	4.2313	0.0257	0.1246
^{9}Be	0.0364	5.6999	83.2770	11.0779	0.0	3.7140	0.0253	0.2147
^{10}Be	0.0481	3.0387	82.1235	9.2828	0.0	3.6425	0.0241	0.2687
^{8}B	0.0182	1.9248	88.4255	17.5519	0.0	3.9833	0.0286	0.1526
^{10}B	0.0077	18.7790	84.7712	9.2654	0.0	3.1890	0.0228	0.2079
^{11}B	0.0084	39.2743	84.5340	7.2697	0.0	2.8620	0.0202	0.3036
^{10}C	0.0059	3.5367	87.8897	9.4666	0.0	3.0738	0.0194	0.2146
^{11}C	0.0034	30.2834	85.9259	7.1506	0.0	2.7119	0.0188	0.2608
^{12}C	0.0035	65.1373	87.8291	4.9251	0.0	2.3254	0.0157	0.2768

Table 4.4. Parameters of Eq. 4.44 considering a ^{16}**O target**. Parameters relative to the energy, E, are expressed in MeV/u while the one of the angle, θ, in degrees.

Frag.	A_1	A_2	$< E >$	σ_E	$< \theta >$	σ_θ	α_E	α_θ
n	0.2960	126.4974	93.5978	37.2839	0.0	10.2876	0.0127	0.0242
^{1}H	0.2960	126.4974	93.5978	37.2839	0.0	10.2876	0.0127	0.0242
^{2}H	0.2763	63.4900	81.7012	25.6455	0.0	9.1688	0.0256	0.0304
^{3}H	0.2656	28.0921	72.7876	18.0416	0.0	7.8953	0.0317	0.0564
^{3}He	0.1473	42.1474	91.3621	29.3215	0.0	7.3130	0.0291	0.0435
^{4}He	0.0834	211.4976	83.2973	15.0659	0.0	5.2933	0.0291	0.0784
^{6}He	0.0811	11.2261	78.9145	17.2059	0.0	5.4690	0.0292	0.1422
^{6}Li	0.0788	14.7060	84.0483	14.4436	0.0	4.5345	0.0279	0.1050
^{7}Li	0.0632	14.3089	78.8127	12.9602	0.0	4.4134	0.0315	0.1117
^{7}Be	0.0395	13.1862	83.5408	16.4800	0.0	4.3163	0.0269	0.1148
^{9}Be	0.0309	6.0120	83.2026	11.7219	0.0	3.8931	0.0271	0.1769
^{10}Be	0.0550	3.2259	82.4304	8.7710	0.0	3.7101	0.0244	0.2381
^{8}B	0.0225	2.0825	88.6345	17.4132	0.0	4.0802	0.0289	0.1439
^{10}B	0.0077	19.1589	84.4614	9.3189	0.0	3.3192	0.0259	0.1733
^{11}B	0.0080	30.8750	84.7540	7.1413	0.0	2.9092	0.0215	0.2465
^{10}C	0.0088	3.5361	88.2696	9.1944	0.0	3.1870	0.0227	0.2054
^{11}C	0.0034	29.8018	86.0085	7.1328	0.0	2.8063	0.0197	0.2277
^{12}C	0.0034	62.2619	87.0351	4.7576	0.0	2.4033	0.0167	0.3032

Extrapolation to different beam energy

The angular and energy distributions, described in the previous Section, correspond to fragments emitted by a beam of 95 MeV/u. To consider every possible energy of the projectile, a scale factor is needed.
The energy of emission of an i-th fragment is scaled in the following way:

$$E^i = E^i_{95\text{MeV/u}} \frac{E_{proj}[\text{MeV/u}]}{95}(1-k), \tag{4.45}$$

where $E^i_{95\text{MeV/u}}$ is the energy extracted from the Gaussian distribution of the Ganil experiment. This formula respects the properties that the fragment's energy per nucleon is on average the same as the projectile E_p, so it increases linearly with it. To take into account that the energy of fragments from the same event is correlated and that the total energy of all fragments from the same event must not exceed the energy of the projectile, a correlation factor, c, has been added in the following way:

$$k = c(1-R), \tag{4.46}$$

where R, for each i-th fragments, depends on the energy of the previous i-1 fragments:

$$R = \frac{E^i_{nucl}}{E_p}, \tag{4.47}$$

$$E^i_{nucl} = \frac{\sum_{j=0}^{j=i} E_j A_j}{\sum_{j=0}^{j=i} A_j}, \tag{4.48}$$

where E_j and A_j are the energy and the atomic number of the previously generated fragments in the current event.
The conservation of energy is preserved and the computational time is reduced since the code does not discard combinations of possible fragments due to their energy. Energies are extracted from a range in agreement with the conservation of the energy. The sampling of the energy released to the target fragments is analogous to the one of the projectile but $E^i_{95\mathrm{MeV/u}}$ is extracted from the exponential distribution without any correlation factors.

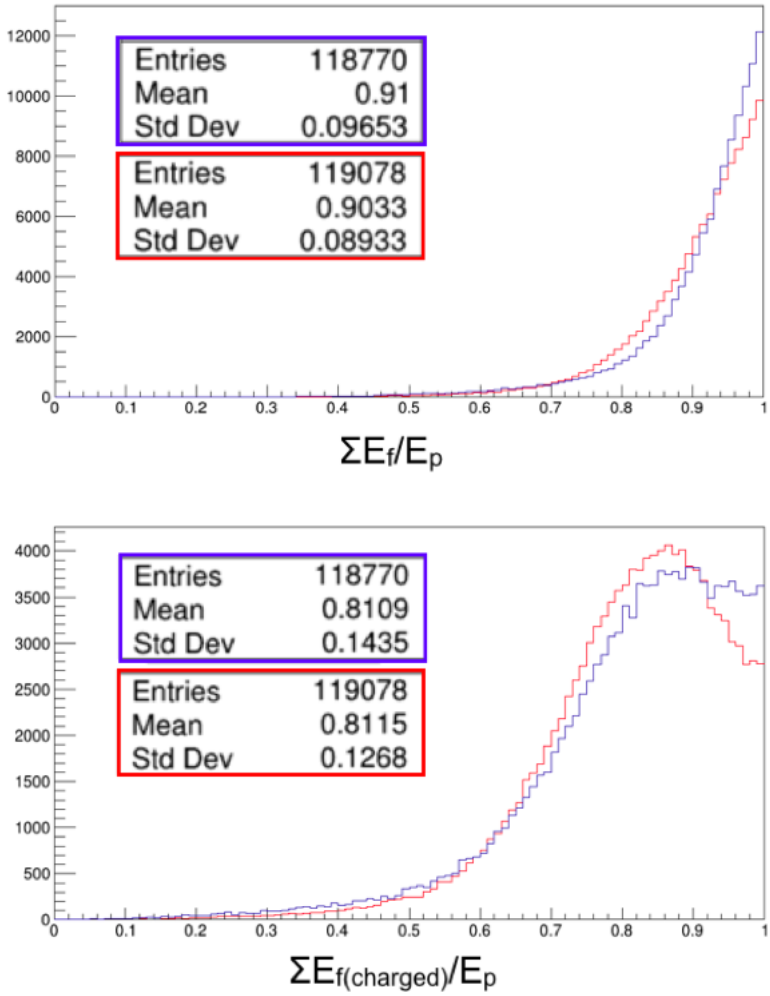

Figure 4.21. Top, the sum of energy of all fragments emitted in an event over the energy of the incident particle is shown. Bottom, the contribution of charged fragments is represented. In blue is the result of the FRED simulation using the correlation factor, in red without using it.

In Fig. 4.21 it is shown a comparison between the fraction of energy assigned to fragments during an event with and without using the correlation factor. The fraction of the total fragments' energy in an event, with the introduction of this factor, increases its mean only from ~ 0.90 to ~ 0.91 for what concerns all fragments. However, its distribution becomes more narrow. Also, the mean energy assigned to charged fragments increases. The gain in energy efficiency is not significant but it reduces the computational time. Actually, the user can set the value of c in the input files. In this thesis, it has been set as 0.4 since with this value it has been observed the best agreement between FRED and FLUKA.
The scaling factor for an angle of emission of an i-th fragment, θ^i, can be deduce starting from te relation:

$$|\vec{p}|sin\theta = p_{\perp}, \tag{4.49}$$

where $|\vec{p}|$ and $p_{\perp}$ are the magnitude of momentum and the transverse momentum of the fragment and θ is the angle described by $\vec{p}$ with respect to the beam trajectory. Considering that the angles of emission are small, it is possible to write:

$$\theta \sim sin\theta = \frac{p_{\perp}}{|\vec{p}|}. \tag{4.50}$$

The transverse momentum does not depend on the projectile energy, whom momentum is parallel to the direction of the beam. As a consequence, the dependence of the angle on the beam energy is due only to the denominator of Eq. 4.50:

$$\frac{\theta}{\theta_{95\mathrm{MeV/u}}} = \frac{|\vec{p}_{95\mathrm{MeV/u}}|}{|\vec{p}|}, \tag{4.51}$$

where $\theta_{95\mathrm{MeV/u}}$ is the angle extracted from the Gaussian distribution of the Ganil experiment and $|\vec{p}_{95\mathrm{MeV/u}}|$ the correspondent momentum.
Making explicit $|\vec{p}|$ in function of the kinetic energy of the fragment, the equation becomes:

$$\frac{\theta}{\theta_{95\mathrm{MeV/u}}} = \frac{\sqrt{E_{95\mathrm{MeV/u}}}}{\sqrt{E}}, \tag{4.52}$$

where $E_{95\mathrm{MeV/u}}$ and E are the kinetic energy of the fragments of the Ganil experiment and of the one of the fragment emitted from a generic energy of the beam. Knowing the scaling factor of the energy of the fragment (Eq. 4.45), the relation between an angle of emission θ^i produced by a beam of energy E_{proj} and the angle of Ganil data, $\theta^i_{95MeV/u}$, is:

$$\theta^i = \theta^i_{95\mathrm{MeV/u}}\sqrt{\frac{95}{E_{proj}[\mathrm{MeV/u}]}}. \tag{4.53}$$

It is possible to observe that, as physically expected, the angle decreases with the energy of the beam.
This scaling is not used for protons and neutrons since, checking the angular dependence with FLUKA, it has been observed that for those particles the angle of emission is energy-independent.
The same scaling factor is also used for the angle of the target fragmentation with the exception of fragmentation due to projectiles with more than 160 MeV/u. In this case, the energies of fragments heavier than helium are set to zero.

4.4 Relative Biological Effectiveness

In Par. 1.2.7, the RBE has been defined as the ratio of the dose of x-ray radiation to the dose of the ion radiation needed to produce the same biological effect. This means that it is necessary to compare doses with the same survival rate.
While for protons the RBE is usually assumed to be 1.1 in clinical practice, for heavier charged particles its calculation is more complex. At the Lawrence Berkeley Laboratory (Berkely, USA) the RBE was described as a function of dose-averaged LET to estimate the biologically effective dose, using a linear-quadratic model to calculate a uniform biological effect along the SOBP [110]. At the Japanese facilities in Chiba (HIMAC) and Hyogo (HIBMC), biological treatment planning is based on cell survival levels which are calculated using a linear-quadratic model as well. Here, starting from mono-energetic beams, the dose-averaged coefficients α and β for a mixed field have been calculated. For patient planning, human salivary gland tumour cells have been used to obtain the RBE distribution as a function of depth. All RBE values are scaled according to the RBE observed in clinical studies with neutrons depending on the position in the SOPB showing the same RBE for cell survival as neutrons [111][112]. At GSI (Darmstadt, Germany) the biophysical Local Effect Model (LEM I) approach is used. It is based on the knowledge of charged particle track structure in combination with the response of the cells or tissues under consideration to conventional photon radiation [113][114][115][116][117].
The LEM I model, already present in MC used in clinical practice (FLUKA and GEANT4), has been implemented in the FRED code. The model, which performs extremely well on GPU cards, and its implementation in the code are described in this paragraph.

4.4.1 Local Effect Model I

The principal assumption of the LEM I is that the local biological effect, such as the biological damage in a small volume of the cell nucleus, is independent of the particular radiation type leading to that energy deposition while is determined only by the expectation value of the energy deposition in that volume. The different spatial energy deposition pattern of charged particles compared to photon radiation is the reason for the differences in the biological action. Moreover, for a given radiation type, differences in the photon dose response curve for different biological objects or tissues should also lead to corresponding differences in the RBE.
To determine the biological effects the dose of the photon has been used as a reference. The cellular inactivation is the consequence of lethal effects and the fraction of cells without lethal events is:

$$S = e^{-\overline{N^{lethal}}}, \tag{4.54}$$

where $\overline{N^{lethal}}$ is the mean number of lethal events. The Poisson distribution S is also the survival probability. The density of lethal events in a cellular nucleus due to a photon radiation is:

$$\nu_x(D) = \frac{\overline{N_x^{lethal}}}{V_{nucleus}} = -\frac{ln(S_x(D))}{V_{nucleus}}, \tag{4.55}$$

where $V_{nucleus}$ is the volume of the cell nucleus and D is the dose. The number of lethal events for a ion beams can be obtained integrating the density of local events ν_{ion}:

$$\overline{N_{ion}^{lethal}(D)} = \int \nu_{ion}(d(x,y,z))dV_{nucleus}, \tag{4.56}$$

where $d(x, y, z)$ is the local dose in the position (x, y, z). Since in the LEM I the principal assumption is that the local biological effects are determined by the local dose independently from the type of radiations, $\nu_{ion}(d)$ is equal to $\nu_x(d)$ (Eq. 4.55) and so from Eq. 4.54 and Eq. 4.56 it is possible to obtain:

$$\overline{N_{ion}^{lethal}(D)} = -\overline{ln(S_{ion}(D))} = \int \frac{-ln(S_x(d(x,y,z)))}{V_{nucleus}} dV_{nucleus}. \tag{4.57}$$

The differences due to the radiation are hidden by the inhomogeneity of the local dose.
As already observe in Eq. 1.47, the most used model for the cell survival function is the linear-quadratic $S = e^{-(\alpha D + \beta D^2)}$. A modified version of the linear quadratic model approach for the photon dose response curve is used, since for many biological objects at high doses a transition from the shouldered to an exponential shape is observed. This transition is described by a parameter D_{cut}, representing the transition dose to exponential shape with slope $S_{max} = \alpha + 2\beta D_{cut}$, so that the dose response is determined by:

$$-ln(S) = \begin{cases} \alpha D + \beta D^2 & if\ D \leq D_{cut} \\ \alpha D_{cut} + \beta D_{cut}^2 + S_{max}(D - D_{cut}) & if\ D > D_{cut} \end{cases}, \tag{4.58}$$

where α and β are two parameters specific for each particle and energy.
Eq. 4.58 is true for a single radiation but, during particle therapy, in a single cell more particles, primary or secondary, release energy. The total number of lesions is higher than the sum of the lesions produced by a single component. If the yield (Y) of lesions follows, as experimentally investigated in the case of chromosome aberrations, a linear-quadratic formula [118] :

$$Y = \alpha D + \beta D^2, \tag{4.59}$$

the sequential exposure to two doses D_1 and D_2 of two different radiation types, gives the following yield of lesions:

$$Y(D_1, D_2) = \alpha_1 D_1 + \beta_1 D_1^2 + \alpha_2 D_2 + \beta_2 D_2^2 + 2\sqrt{\beta_1 \beta_2} D_1 D_2. \tag{4.60}$$

The method can be generalised to n doses from different radiation types, each one characterized by a certain value of the parameters α_i and β_i:

$$Y(D_1, D_2, ..., D_n) = \sum_{i=1}^{n} \alpha_i D_i + \left(\sum_{i=1}^{n} \sqrt{\beta_i} D_i \right)^2. \tag{4.61}$$

Within this formalism the average parameters for a mixed field can be calculated as:

$$\begin{aligned} \bar{\alpha} &= \frac{\sum_{i=1}^{n} \alpha_i D_i}{\sum_{i=1}^{n} D_i}, \\ \bar{\beta} &= \left(\frac{\sum_{i=1}^{n} \sqrt{\beta_i} D_i}{\sum_{i=1}^{n} D_i} \right)^2. \end{aligned} \tag{4.62}$$

Finally the biological effect $-ln(S)$ and RBE-weighted dose, D_{RBE}, are calculated as:

$$-ln(S) = \begin{cases} (\bar{\beta} D_{abs} + \bar{\alpha}) D_{abs} & if\ D_{abs} \leq D_{cut} \\ (\bar{\beta} D_{cut} + \bar{\alpha}) D_{cut} + S_{max}(D_{abs} - D_{cut}) & if\ D_{cut} > D_{cut} \end{cases}, \tag{4.63}$$

$$D_{RBE} = \begin{cases} \sqrt{\frac{-ln(S)}{\beta_x} + \left(\frac{\alpha_x}{2\beta_x}\right)^2} - \frac{\alpha_x}{2\beta_x} & if \ -ln(S) \leq -ln(S_{cut}), \\ \frac{-ln(S)+ln(S_{cut})}{S_{max}} + D_{cut} & if \ -ln(S) > -ln(S_{cut}), \end{cases} , \tag{4.64}$$

where D_{abs} is the absorbed dose, $ln(S_{cut})$ id the biological effect calculated for $D_{abs} = D_{cut}$, α_x and β_x are constant parameters of a photon radiation and S_{max} is defined as:

$$S_{max} = \bar{\alpha} + 2\bar{\beta}D_{cut}. \tag{4.65}$$

4.4.2 Implementation of LEM I in FRED

The Local Effect Model implementation in FRED is summarized in the flowchart of Fig. 4.22.

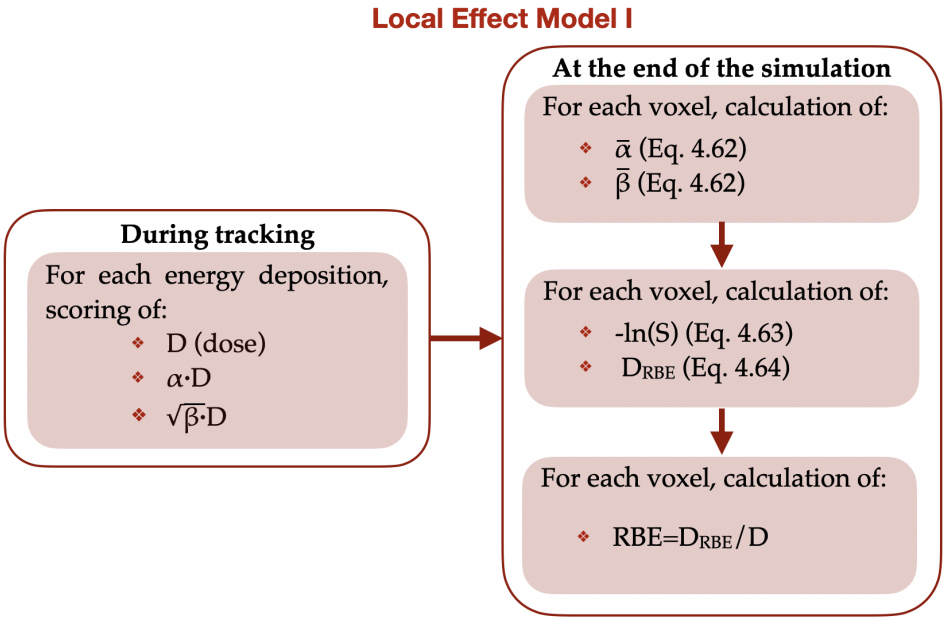

Figure 4.22. Flowchart of the Local Effect Model in FRED. Parameters α and β are the one used in Topas (Fig. 4.23).

While FRED tracks primary and secondary particles, every time that energy is deposited in the target, FRED scores in a map, with the same dimension of the phantom, values which are necessary for the calculation of RBE-weighted dose: D(dose), αD and $\sqrt{\beta}D$. Values of α and β are dependent on the type of particle and its energy. Fred reads those values from a texture file. This file is user-configurable and, in particular, TOPAS parameters for the cell line V79, plotted in Fig. 4.23, has been used in this thesis.
Once all particles have been simulated, for each voxel, FRED calculates the mean value of α and β using Eq. 4.62 and values saved during the tracking.
At this point, setting the threshold dose D_{cut} as 30 MeV/u and parameters of photon radiation α_x and β_x constants ($\alpha_x = 0.0722$ Gy^{-1} and $\beta_x = 0.0502$ Gy^{-2}), it is possible to obtain values of the biological effects (Eq. 4.63) and of the RBE-weighted dose (Eq. 4.64) for each voxel.

Finally the RBE values in the i-th voxel can be obtain:

$$RBE^i = \frac{D^i_{RBE}}{D^i}. \tag{4.66}$$

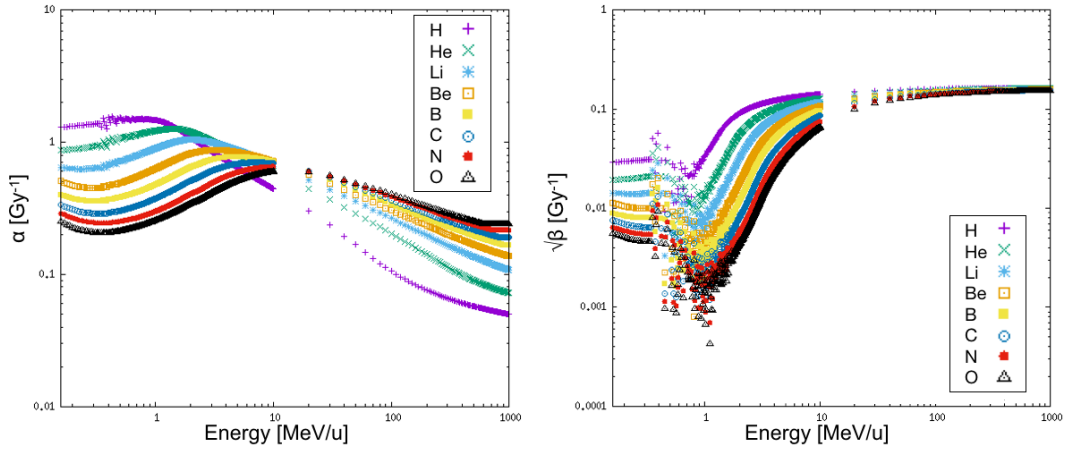

Figure 4.23. Plot of TOPAS parameters α (left) and $\sqrt{\beta}$ (right) as a function of energy deposited by different particles for the cell line V79.

Chapter 5

Results

In this chapter, the results obtained with the implementation of models described in Chapter 4 are compared with a full-MC, FLUKA, that is commonly used in particle therapy. As observed in Par. 3.1, FLUKA can reproduce the position of the Bragg peaks of carbon ion beams on average within the experimental uncertainties of about 100 μm and the average dose-weighted dose-difference ($\overline{\Delta D/D}$) is below 1.5%. Furthermore, in the chapter, a comparison with experimental data is shown as well.

5.1 Comparison with full-MC codes

The implemented nuclear models of FRED were tested against the full-MC code FLUKA. In particular, the longitudinal and lateral dose of different beams in a water phantom has been simulated and compared in different configurations and with different projectiles.
In Par. 5.1.1, single pencil-beams of ^{12}C ions on water target has been simulated both with FLUKA and FRED comparing the longitudinal and lateral distribution for 3 different energies in the therapeutic energy range. To observe the ability of the code to simulate also the secondary particles emitted during the path of ions in the target, the dose distribution of beams of ^{4}He, ^{6}Li, ^{7}B and ^{10}B have been studied.
In Par. 5.1.2 a SOBP composed of 14 slices from 186.57 to 223.56 MeV/u has been simulated. Not only longitudinal and lateral integrate dose has been compared but also the dose maps have been studied observing the gamma-index pass-rate test.
Finally, in Par. 5.1.3, a comparison between the RBE-weighted dose and the RBE obtained with FRED and FLUKA is shown.

5.1.1 Single Pencil-Beams

A first study on a single pencil-beam is necessary to understand if FRED can be used as an alternative to a full-MC code and to highlight possible inaccuracy of the model. Fig. 5.1 shows depth–dose profiles simulated by FRED for carbon ions in the therapeutic energy range (100-300 MeV/u), compared to a FLUKA simulation. In particular, the curves correspond to a single pencil-beam of mono-energetic carbon ions on a water phantom ($10 \times 10 \times 40$ cm^3). The dose per primary is presented, while the code has been run with a statistic of about 10^8 histories to minimize the statistical fluctuations. The profiles closely overlap and, in particular, the agreement at the peak is very good at 100 and 200 MeV/u, 0.05% and 1.4% respectively, and get worse at 300, where it is 4.8%. The agreement with the FLUKA predictions is always within

2.5% of the integral dose deposited over the whole depth in the 100-300 MeV/u energy range, with the best agreement at 100 MeV/u where the difference is only 0.05%.

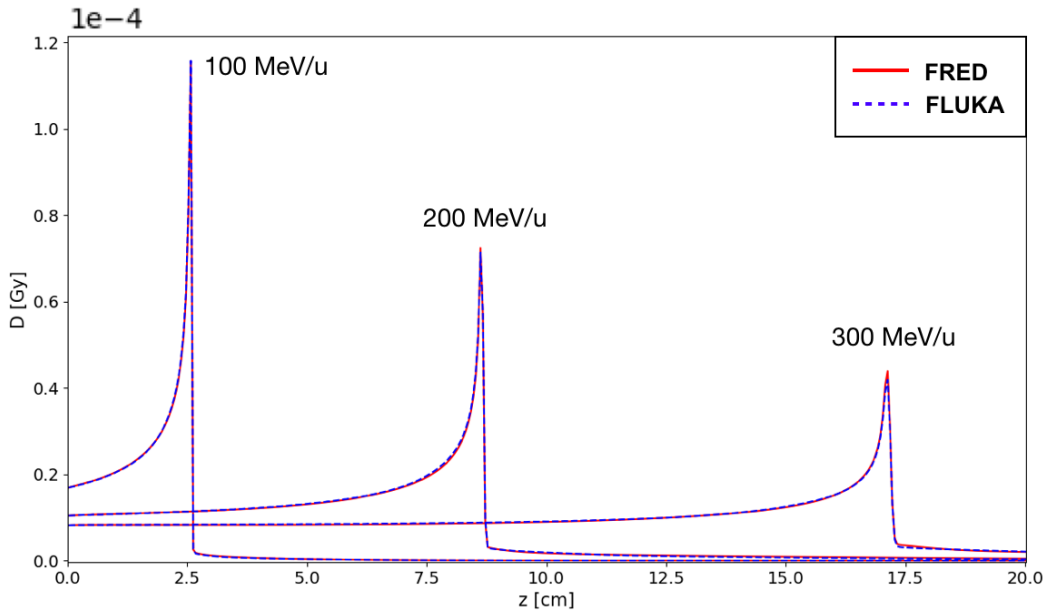

Figure 5.1. Longitudinal integrated dose for carbon ion beams in water at different energies. The dose is relative to one primary particle but the simulation has been run with a statistic of about 10^8 histories. Comparison between FRED (red) and FLUKA (blue) simulation, with the same scoring grid, and the same statistics is presented.

Fig. 5.2, Fig. 5.3 and Fig. 5.4 show the dose line profile for a single pencil beam of 100, 200 and 300 MeV/u along the beam axis (longitudinal) and at the Bragg peak position (lateral). The lateral transverse profiles show in linear and logarithmic scale the tails of the distribution, mainly due to nuclear interactions. Comparison with FLUKA simulation, with the same scoring grid and the same statistics, shows good agreement in lateral dose distribution too. From this comparison, it is possible to deduce that the multiple Coulomb scattering, the elastic scattering and the angular distribution of secondary fragments have been implemented correctly. Also, the axis profile of the dose in the central voxel shows an overlap in almost all the particle range.
Considering that the fragmentation of secondary fragments has been implemented in the code, also the distribution of dose in the water of possible products of fragmentation has been studied. In Fig. 5.5, Fig. 5.6, Fig. 5.7 and Fig. 5.8 it is possible to observe the dose of some of the isotopes usually produced by a carbon ion in water, respectively ^{4}He, ^{6}Li, ^{7}Be and ^{10}B. Except for helium, the distributions are in good agreement with FLUKA both in longitudinal and lateral dose. The differences between FRED and FLUKA in the ^{4}He distributions are because the total cross-section of secondary fragments is obtained directly from the Kox formula which is not appropriate for this isotope. In the future, this cross-section will be adjusted to correctly describe the helium fragmentation. However, the contribution to the total dose of secondary fragmentation of helium is negligible for this thesis.

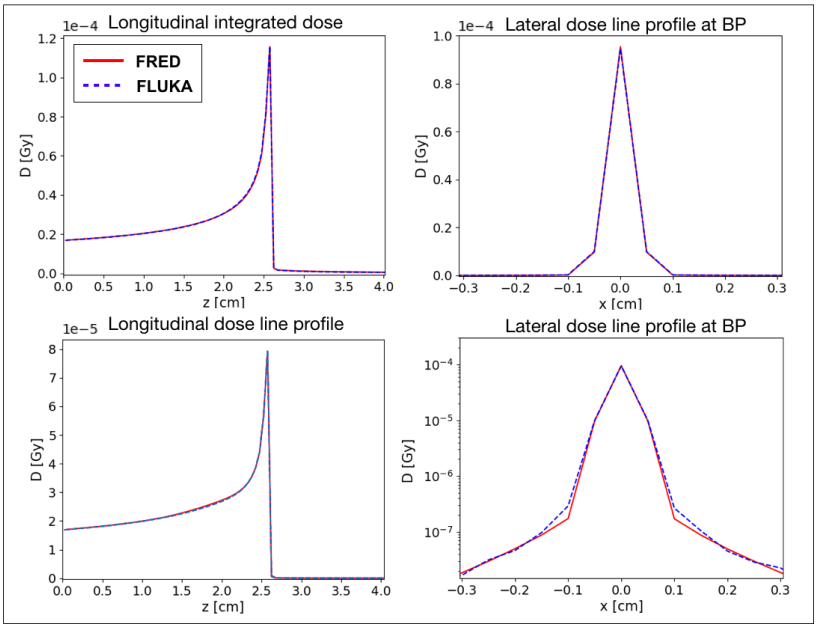

Figure 5.2. Dose in water for a 100 MeV/u carbon ion beam simulated with FRED (red continuous line) and FLUKA (blue dotted line) with the same scoring grid and the same statistics. Integrated longitudinal dose (top left), central axis profile along beam axis (bottom left), lateral axis profile at the Bragg Peak, 2.6 cm, depth in linear scale (top right) and logarithmic (bottom right) scale.

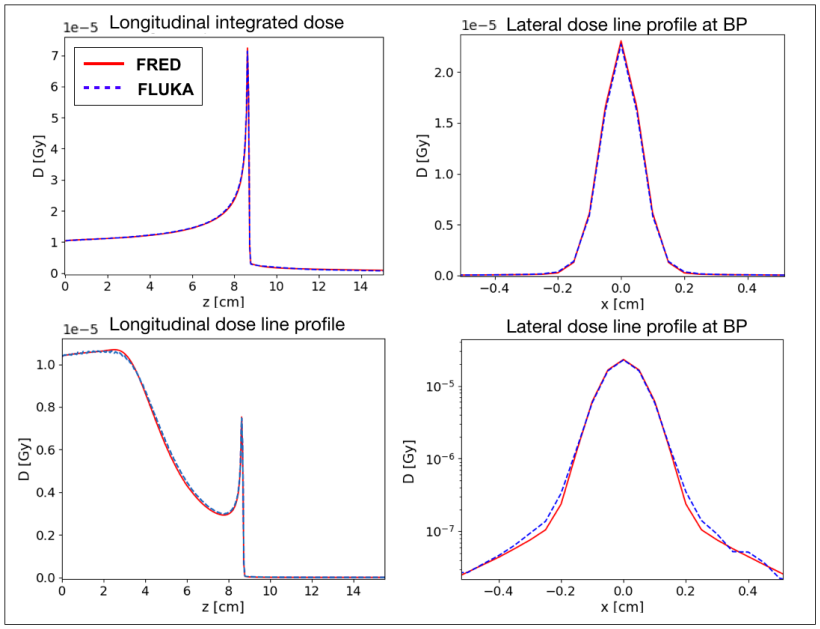

Figure 5.3. Dose in water for a 200 MeV/u carbon ion beam simulated with FRED (red continuous line) and FLUKA (blue dotted line) with the same scoring grid and the same statistics. Integrated longitudinal dose (top left), central axis profile along beam axis (bottom left), lateral axis profile at the Bragg Peak, 8.6 cm, depth in linear scale (top right) and logarithmic (bottom right) scale.

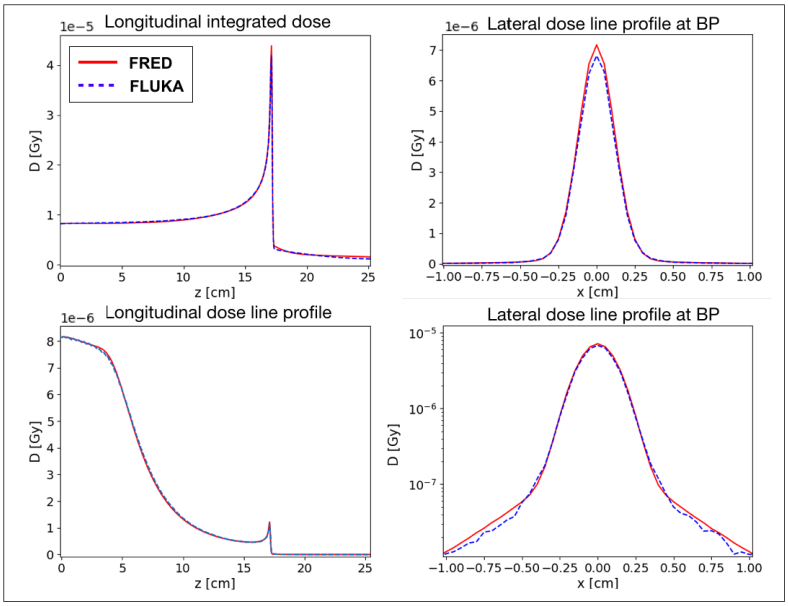

Figure 5.4. Dose in water for a 300 MeV/u carbon ion beam simulated with FRED (red continuous line) and FLUKA (blue dotted line) with the same scoring grid and the same statistics. Integrated longitudinal dose (top left), central axis profile along beam axis (bottom left), lateral axis profile at the Bragg Peak, 17.1 cm, depth in linear scale (top right) and logarithmic (bottom right) scale.

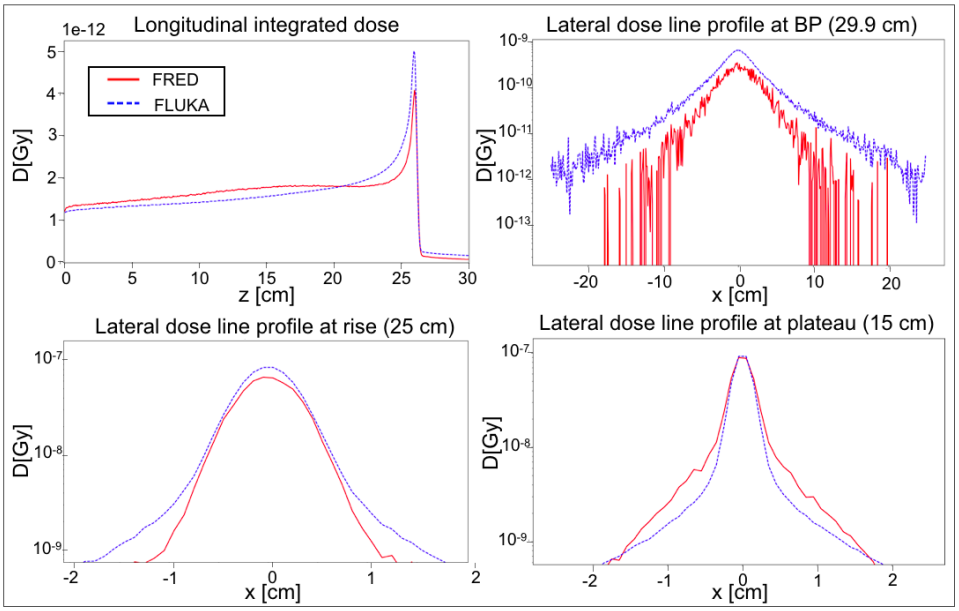

Figure 5.5. Dose in water for a 200 MeV/u ^{4}He beam simulated with FRED (red continuous line) and FLUKA (blue dotted line) with the same scoring grid and the same statistic. Integrated longitudinal dose (top left), lateral axis profile at Bragg Peak, 29.9 cm depth (top right), lateral axis profile at rise, 25 cm depth (bottom left), lateral axis profile at plateau, 15 cm depth (bottom right).

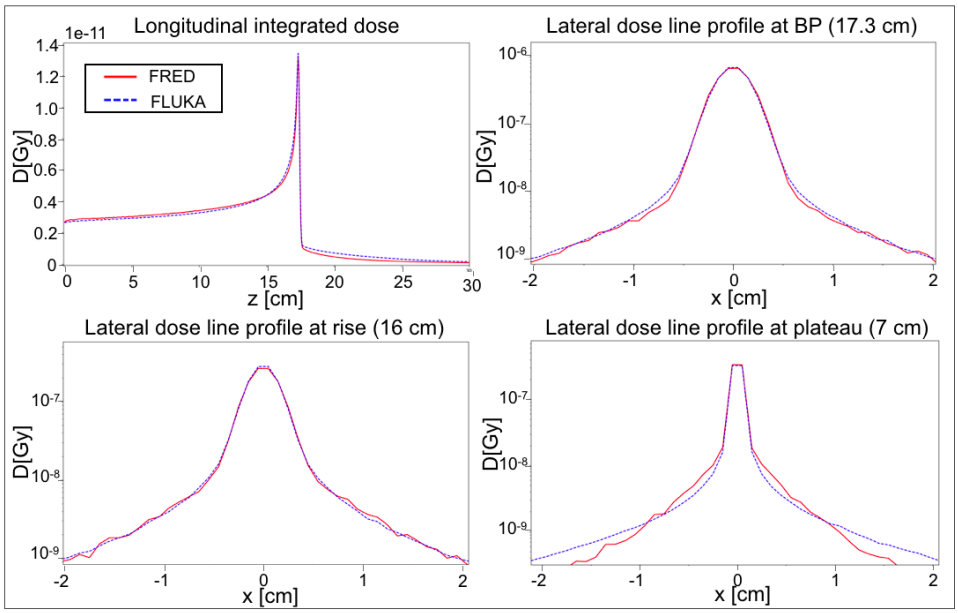

Figure 5.6. Dose in water for a 200 MeV/u ^{6}Li beam simulated with FRED (red continuous line) and FLUKA (blue dotted line) with the same scoring grid and the same statistic. Integrated longitudinal dose (top left), lateral axis profile at Bragg Peak, 17.3 cm depth (top right), lateral axis profile at rise, 16 cm depth (bottom left), lateral axis profile at plateau, 7 cm depth (bottom right).

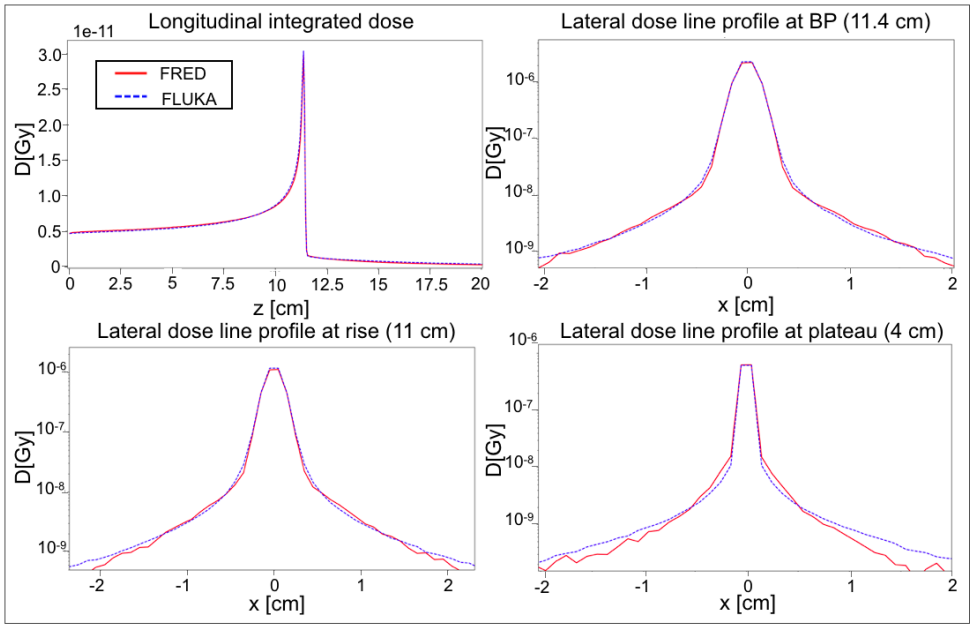

Figure 5.7. Dose in water for a 200 MeV/u ^{7}Be beam simulated with FRED (red continuous line) and FLUKA (blue dotted line) with the same scoring grid and the same statistic. Integrated longitudinal dose (top left), lateral axis profile at Bragg Peak, 11.4 cm depth (top right), lateral axis profile at rise, 11 cm depth (bottom left), lateral axis profile at plateau, 4 cm depth (bottom right).

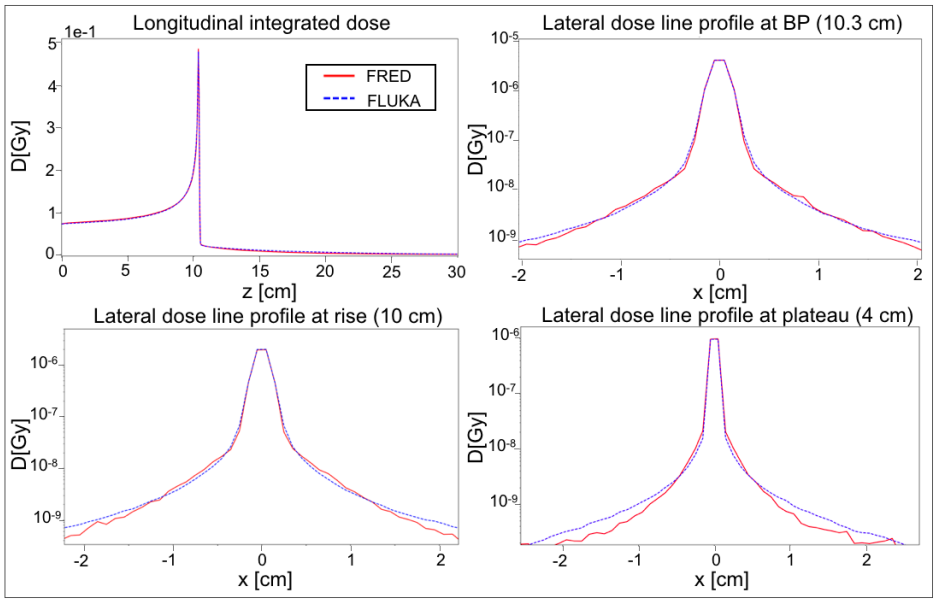

Figure 5.8. Dose in water for a 200 MeV/u ^{10}B beam simulated with FRED (red continuous line) and FLUKA (blue dotted line) with the same scoring grid and the same statistic. Integrated longitudinal dose (top left), lateral axis profile at Bragg Peak, 10.3 cm depth (top right), lateral axis profile at rise, 10 cm depth (bottom left), lateral axis profile at plateau, 4 cm depth (bottom right).

5.1.2 SOBP

After having studied the behavior of a single pencil beam, the next step was to observe if the agreement is the same also considering a SOBP (Sec. 1.2.2) composed of more pencil-beams of different energies.

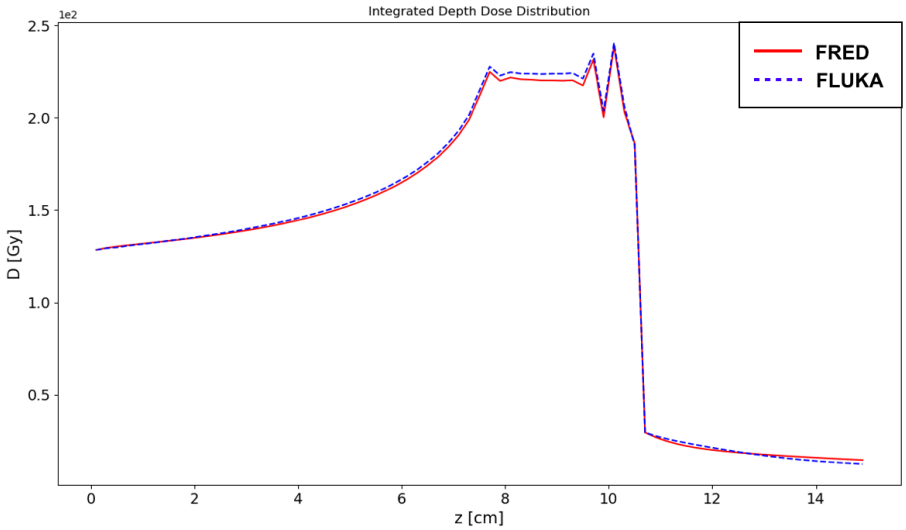

Figure 5.9. Longitudinal integrated dose for a SOBP in water. Comparison between FRED (red) and FLUKA (blue) simulation, with the same scoring grid, and the same statistics is presented.

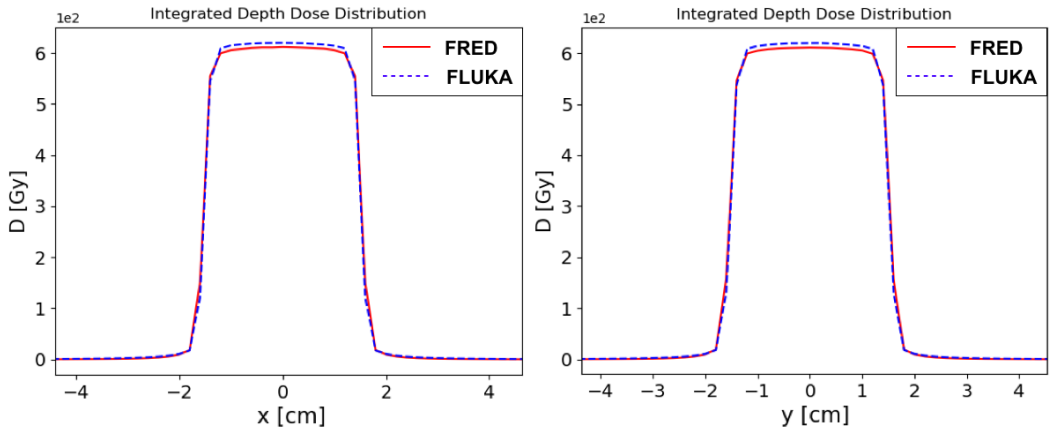

Figure 5.10. Lateral integrated dose (in the overall depth extension) for a SOBP in water. Comparison between FRED (red) and FLUKA (blue) simulation, with the same scoring grid, and the same statistics is presented.

This is a more realistic simulation considering the purpose of the code. In particular, a cube of $3 \times 3 \times 3$ cm^3 starting at a depth of 7 cm with 1 Gy of physical dose in the cube has been simulated in a water phantom ($15 \times 15 \times 15$ cm^3) both with FLUKA and FRED. The spatial resolution is the same given by the CT and so used in the clinical context: 2 mm for all the directions. To obtain the cube, 14 slices from 186.57 to 223.56 MeV/u, with 225 beams for slice, have been simulated with a total of $\sim 2 \times 10^8$ particles. In Fig. 5.9 and Fig. 5.10, the longitudinal and lateral distribution of the SOBP is shown.

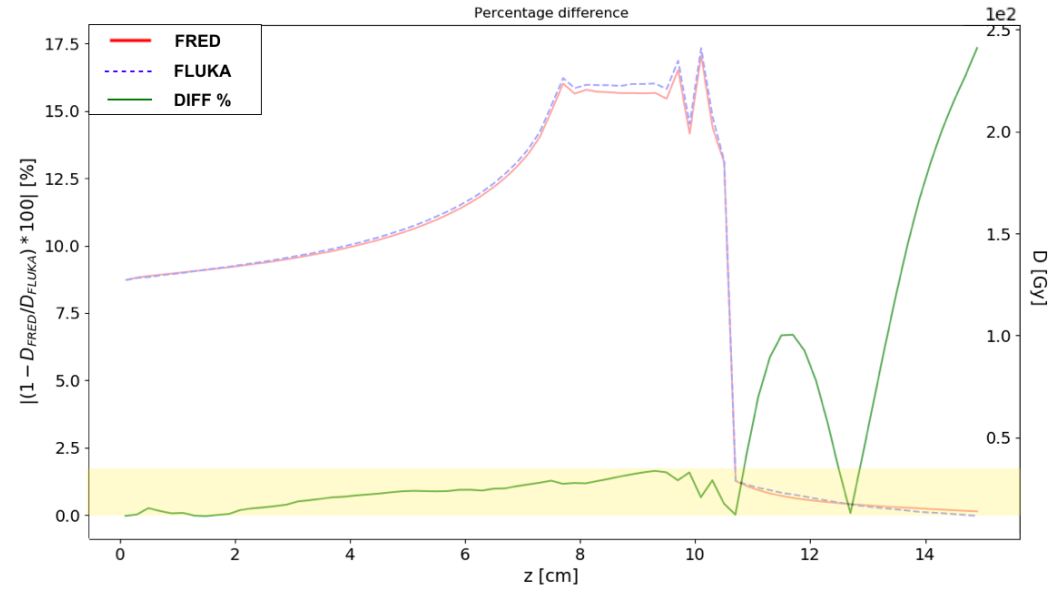

Figure 5.11. Longitudinal integrated dose for a SOBP in water (right scale) superimpose with the percent difference between FRED and FLUKA (left scale). The SOBP is the same of the one represented in Fig. 5.9 and in yellow the difference between 1.7% is highlighted.

How it is possible to observe in Fig. 5.11, in the most significant region of the SOBP the agreement is within the 1.7%. In the tail of the distribution, the difference between FRED and FLUKA increases because there is a small difference in dose in a region where a small amount of dose is released. The agreement with the FLUKA predictions is within 0.8% of the total dose deposited.
To guarantee a high-quality treatment, another important aspect to be carefully taken into consideration is the comparison between dose maps. An efficient and quantitative method of dose map comparison usually used is the γ-index pass-rate test. The reference distribution could be a 3D dose map computed with a simulation software or a simple point set experimentally determined, for example with an ionization chamber. In this specific situation, the reference distribution has been computed with FLUKA. While the evaluated dose map is the dose distribution obtained by FRED.
The gamma-test is based on a generalized "distance" between corresponding points of the two distributions. The parameter computed distance is extended in both space and dose dimensions. The generalized distance, Γ, is the Euclidean distance in a dose-distance space, where both axes are normalized concerning a maximum tolerance both for dose and distance. Given a point $\vec{r}_e$ in the map to be evaluated, the Γ function is:

$$\Gamma(\vec{r}_e, \vec{r}_r) = \sqrt{\frac{|\vec{r}_e - \vec{r}_r|^2}{\Delta d^2} + \frac{[D_e(\vec{r}_e) - D_r(\vec{r}_r)]^2}{\Delta D^2}}, \tag{5.1}$$

where $\vec{r}_r$ runs on all the points of the reference map, $D_e(\vec{r}_e)$ and $D_r(\vec{r}_r)$ are the evaluated and the reference doses, and Δd and ΔD are the dose difference (DD) and the distance to agreement (DTA) criteria. The DD value is expressed in % and it corresponds to the percentage of the max dose of the dose distribution. The DTA value is expressed in mm and it corresponds to the maximum distance from the specific point.

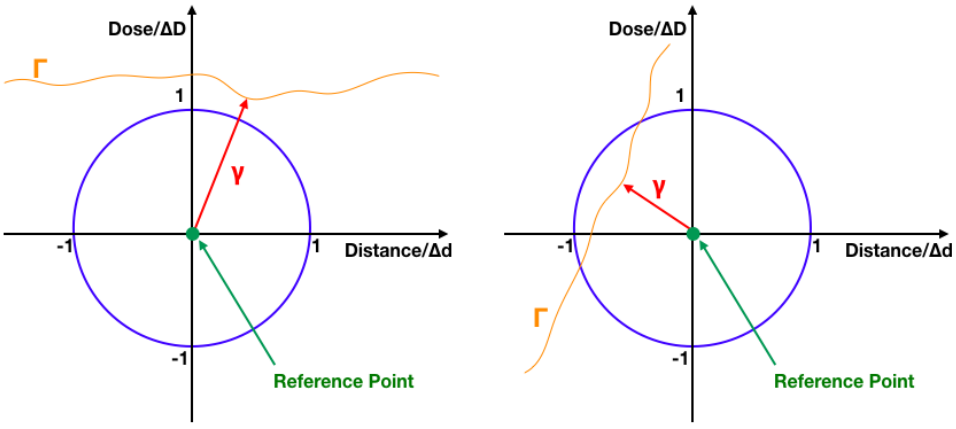

Figure 5.12. Graphic description of the meaning of the Γ function. The orange line represents the evaluated distribution. The blue circle defines the pass-fail criteria. If the line is external to the circle the test is not passed (left) otherwise it is passed (right).

Γ function depends on the position in the dose-distance space of both reference and evaluated points. The quantity which determines if the test is passed is the minimum value of Γ related to a single reference point:

$$\gamma(\vec{r}_r) = min\{\Gamma(\vec{r}_e, \vec{r}_r)\} \forall \vec{r}_e \leq 1. \tag{5.2}$$

From a pictorial point of view, $\gamma(\vec{r}_r)$ is the minimum distance between the two distributions in the dose-spatial distance space. The origin of the plane is placed at the reference point position and the axes are dimensionless because the spatial and dose distances are normalized with the DTA and DD criteria, respectively (Fig. 5.12). When the spatial and dose distances are equal to the related criteria the value of Γ is equal to 1, so one can define a unit circle in the above-described space. Such a unit circle defines the region inside which the value of Γ is less than 1. In the dose-spatial distance space, the evaluated distribution is represented as a line, a sheet or a hyper-sheet according to evaluated distribution dimensions. The test passing or failing of each reference point is determined by the intersection (or not) of the evaluated distribution with the unit circle.
In Fig. 5.12, two examples of calculations are represented. On the left, the figure refers to a distribution that has not passed the test. It can be observed that the dose is nearly constant in the proximity of the reference point. On the right an example of a passed test. The evaluated distribution line has a high "slope" that testifies the rapid change of dose near the reference point.

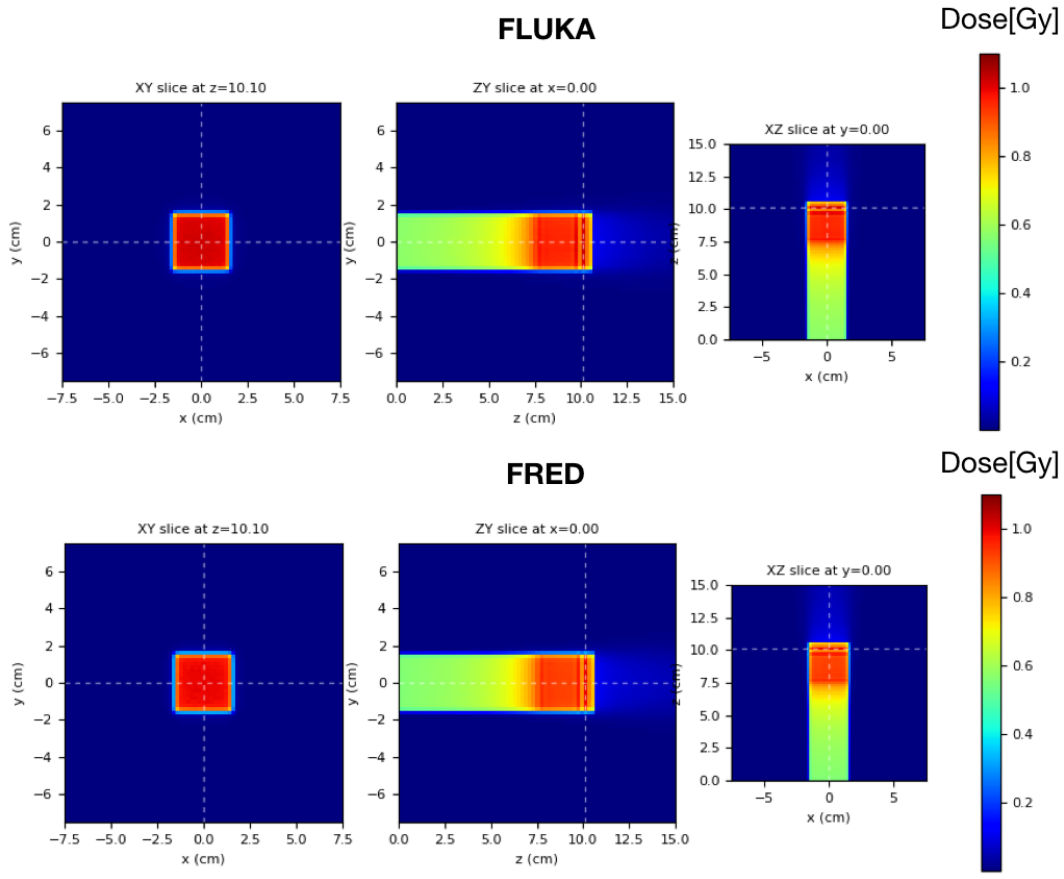

Figure 5.13. Map dose for a SOBP in water simulated with FLUKA (top) and FRED (bottom). It is composed of 14 slices from 186.57 to 223.56 MeV/u, with 225 carbon ion beams for slice. The total dose is $\sim 2 \times 10^8$ and the total number of primary is 2×10^8. The xy slice (left) shows the dose distribution at z=10.1 cm, which is in the peak region of the SOBP, while the other slices (center and right) are centered in x and y.

In Fig. 5.13 it is possible to observe the map of dose obtained with FLUKA and with FRED and in Fig. 5.14 the corresponding γ-index test. Eq. 5.1 and Eq. 5.2 are strongly dependent to the statistical uncertainty, inherent to MC, which may (artificially) improve the γ pass-rate. However, it has been observed that 2×10^8 primary are enough to consider the statistical uncertainty negligible. 10 different simulations, with different seeds, have been obtained both with FRED and FLUKA. The γ-index 2mm/3% between one of the FRED simulation and the others is always 100%. Moreover, the standard deviation on the maximum value of the dose is 0.002 Gy, which is significantly smaller than the DD criteria of 3% (0.03 Gy for the SOBP and 0.1 for the RBE-weighted dose described in Sec. 5.1.3). The same results have been obtained with FLUKA.
It is possible to notice that, as already observed in Fig. 5.9, the dose deposited in FRED is slightly smaller than the one of FLUKA. However, the γ-index 2mm/3% pass-rate is 93.3% considering only voxel with a dose higher than the 1% of the maximum. This result is excellent since usually the spacing used for TPS is 2 mm and shows a possible use of FRED in clinical practice.

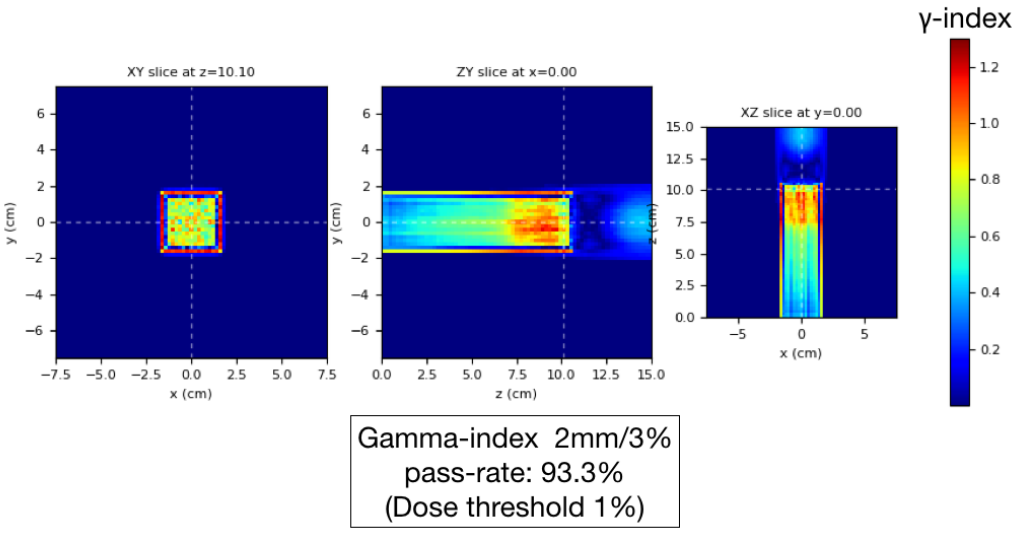

Figure 5.14. The γ-index distribution of the two map of Fig. 5.13. The γ-index 2mm/3% pass rate is 93.3%. The maximum value of the γ-index is 1.2, while the mean is 0.4. The xy slice (left) shows the dose distribution at z=10.1 cm, which is in the peak region of the SOBP, while the other slices (center and right) are centred in x and y.

5.1.3 RBE and RBE-weighted dose

The last comparison done with FLUKA has been focused on the implementation of the calculation of RBE and RBE-weighted dose in FRED. The same tables of α and β, described in Par. 4.4.2, have been considered for the LEM I model both in FRED and in FLUKA. FLUKA has already been tested comparing it with the NIRS (National Institute for Radiological Sciences, Japan) clinical RBE-weighted dose obtaining a γ-index 2mm/3% always more than 90% [119]. The same configurations of Par. 5.1.1 and Par. 5.1.2 (single pencil beams of 100, 200 and 300 MeV/u and cube of dose in water phantoms) have been used for the simulation.
The central axis profile of the RBE-weighted dose for single pencil beams of 100, 200 and 300 MeV/u is shown in Fig. 5.15, Fig. 5.17 and Fig. 5.19 respectively. The

agreement between FRED and FLUKA is excellent for beams of 100 MeV/u and 200 MeV/u, within the 1.7% and 2% respectively. As expected from previous tests, the result is different for a beam of 300 MeV/u where the agreement is within the 2% in the first part of the curve (until $\sim$ 13 cm) and then get worse with a maximum of 6% at the Bragg peak.

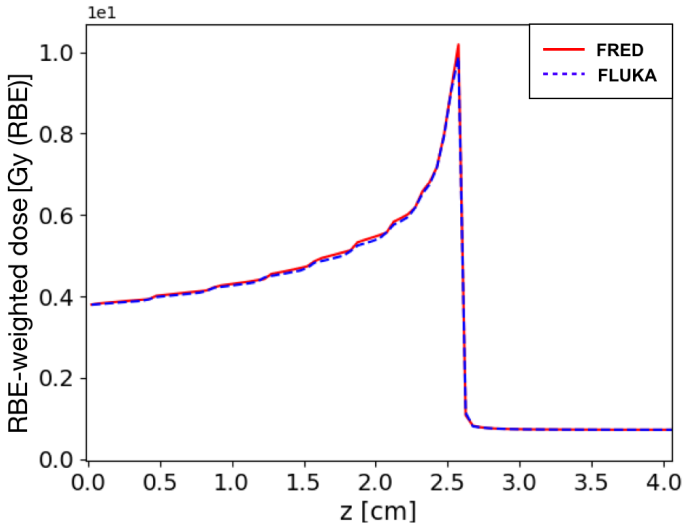

Figure 5.15. Longitudinal central axis profile of the RBE-weighted dose for a 100 MeV/u carbon ion beam in water. The dose is relative to 10^5 primary particles but the simulation has been run with a statistic of about 10^6 histories. Comparison between FRED (red) and FLUKA (blue) simulation, with the same scoring grid, and the same statistics is presented.

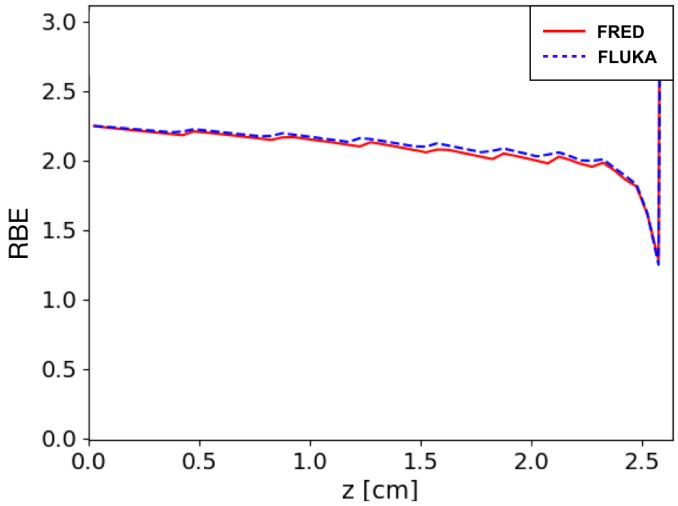

Figure 5.16. Longitudinal central axis profile of the RBE for a 100 MeV/u carbon ion beam in water. The RBE is relative to the RBE-weighted dose represented in Fig. 5.15 for FRED (red) and FLUKA (blue) simulations.

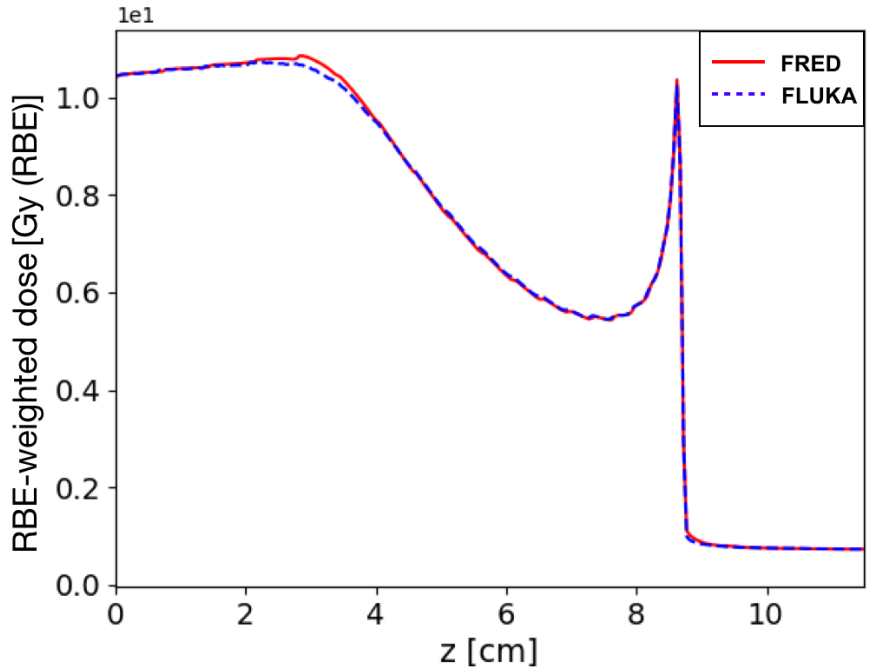

Figure 5.17. Longitudinal central axis profile of the RBE-weighted dose for a 200 MeV/u carbon ion beam in water. The dose is relative to 10^6 primary particles and the simulation has been run with the same statistic. Comparison between FRED (red) and FLUKA (blue) simulation, with the same scoring grid, and the same statistics is presented.

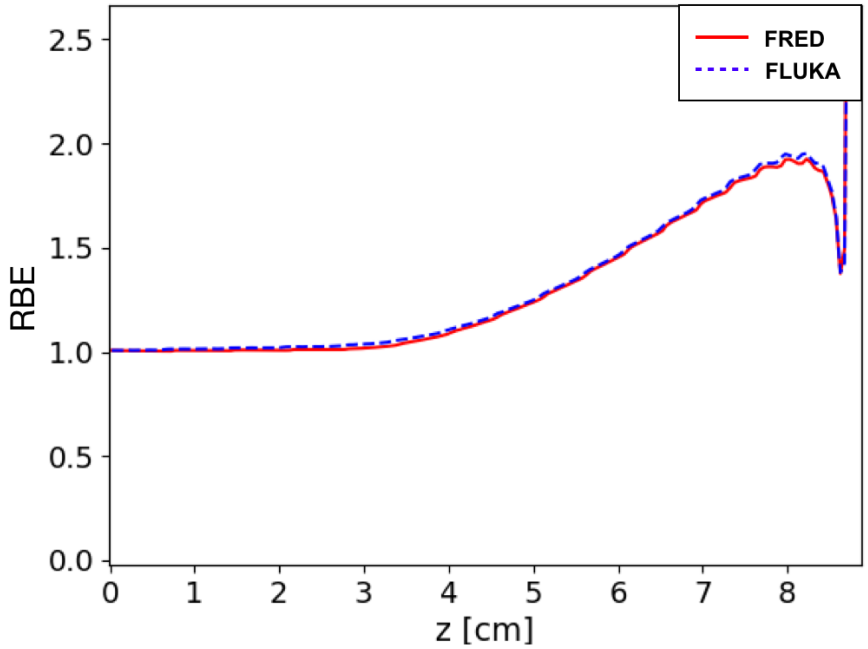

Figure 5.18. Longitudinal central axis profile of the RBE for a 200 MeV/u carbon ion beam in water. The RBE is relative to the RBE-weighted dose represented in Fig. 5.17 for FRED (red) and FLUKA (blue) simulations.

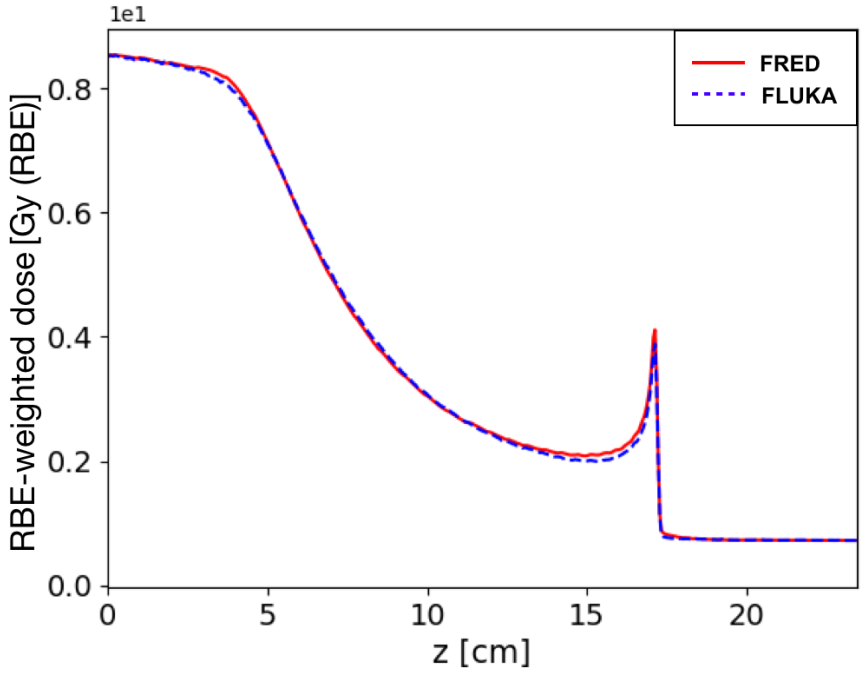

Figure 5.19. Longitudinal central axis profile of the RBE-weighted dose for a 300 MeV/u carbon ion beam in water. The dose is relative to 10^6 primary particles and the simulation has been run with the same statistic. Comparison between FRED (red) and FLUKA (blue) simulation, with the same scoring grid, and the same statistics is presented.

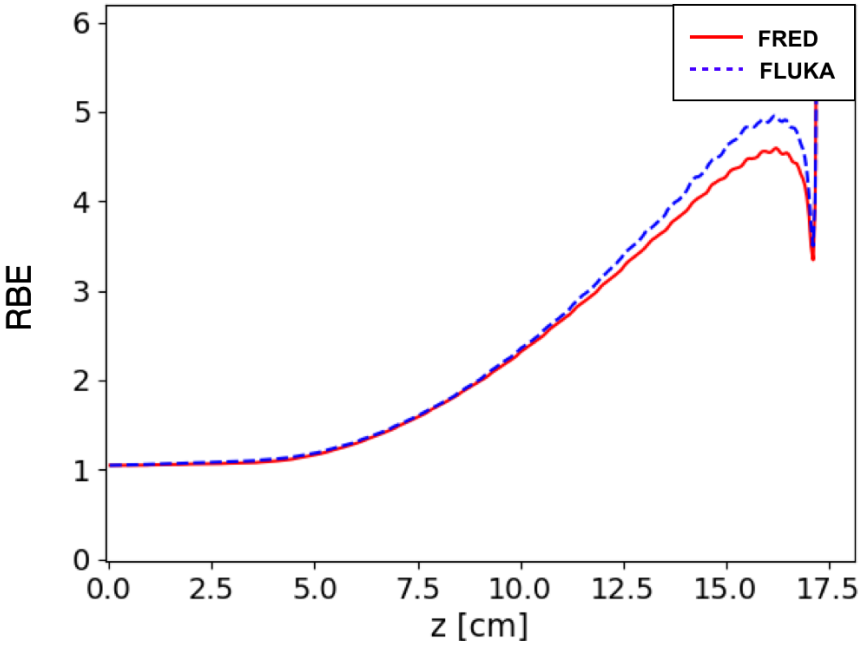

Figure 5.20. Longitudinal central axis profile of the RBE for a 300 MeV/u carbon ion beam in water. The RBE is relative to the RBE-weighted dose represented in Fig. 5.19 for FRED (red) and FLUKA (blue) simulations.

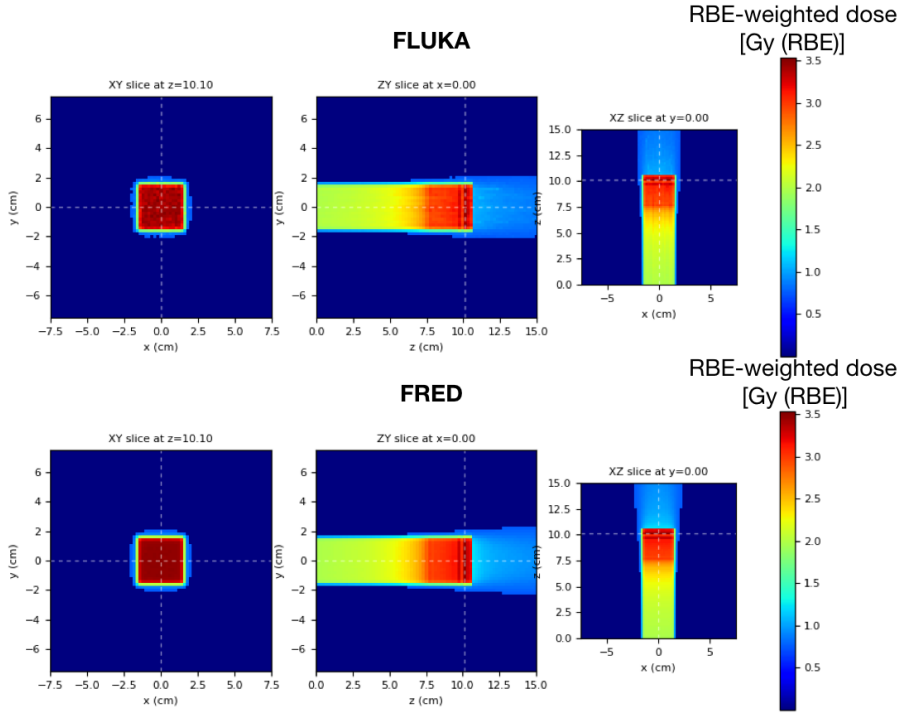

Figure 5.21. Map of RBE-weighted dose for a SOBP in water simulated with FLUKA (top) and FRED(bottom). The simulation has been run with a statistic of 2×10^8 histories. The dose due to the carbon beams is the same of Fig. 5.13 of Par. 5.1.2. The RBE-weighted dose has been obtained only in voxel where the dose in higher than the 1% of the maximum dose. The xy slice (left) shows the dose distribution at z=10.1 cm, which is in the peak region of the SOBP, while the other slices (center and right) are centered in x and y.

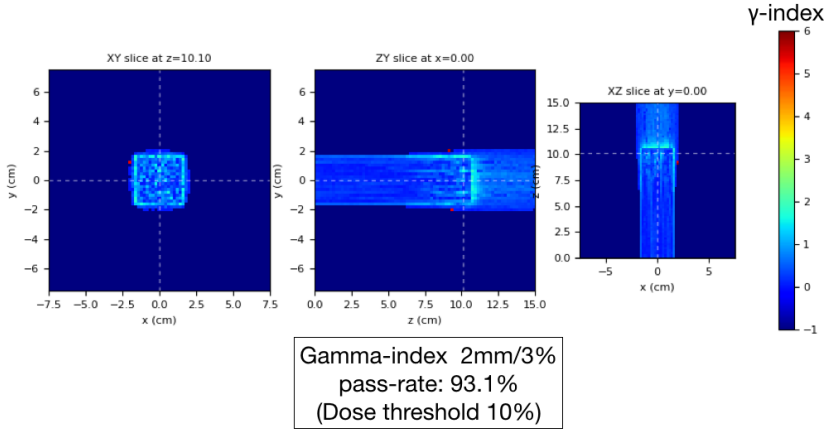

Figure 5.22. The γ-index distribution of the two map of Fig. 5.21. The gamma-index 2mm/3% pass rate is 93.1%. The maximum value of the γ-index is 6, while the mean is 0.4. Values in dark blue (γ-index=-1) are the ones where the RBE-weighted dose has not to be considered and set as 0 Gy). The xy slice (left) shows the dose distribution at z=10.1 cm, which is in the peak region of the SOBP, while the other slices (center and right) are centred in x and y.

The comparison is analogous for what concerns the calculation of RBE. The longitudinal axis profile of the relative biological effectiveness is shown in Fig. 5.16, Fig. 5.18 and Fig. 5.20 for a beam of 100, 200 and 300 MeV/u respectively.
For what concerns the combination of more pencil beams at different energies, the map of the obtained RBE-weighted doses in FRED and FLUKA is presented in Fig. 5.21. The gamma-index 2mm/3% shows a pass rate of 93.1%.
The slightly worsening of the agreement, compared with the dose studied in previously paragraphs, is due to the fact that the RBE-weighted dose is strongly correlated to the spectrum of fragments that deposit the dose in the target and their energy. To better understand where the differences come from, one analysis that will be done soon is to compare the dose deposition from the primaries and from the individual charged fragments between FLUKA and FRED. Despite this difference, the result remains satisfactory. With the increasing of experiments focused on the ion fragmentation at energies of interest in particle physics (for example the experiment in progress FOOT [96][97][98][99][100]) it will be possible to adjust the scaling at energies higher than the one of Ganil, improving further the model.

5.2 Comparison with Data

AAfter checking the agreement between FRED and another well tested MC code (FLUKA) we simulated experiments found in the literature and compared FRED with data. The first experiment which has been simulated is the one used to benchmark the model: the Ganil experiment. Then we compared the FRED results with other experiments in the literature.

5.2.1 Ganil experiment

An experiment was performed in 2011 at GANIL to obtain cross-sections for a 95 MeV/nucleon carbon beam on different thin targets for angles from 4° to 43° [93]. To complete these data, another experiment was performed in 2013 again at GANIL to measure the fragmentation cross-section at zero degrees [95].

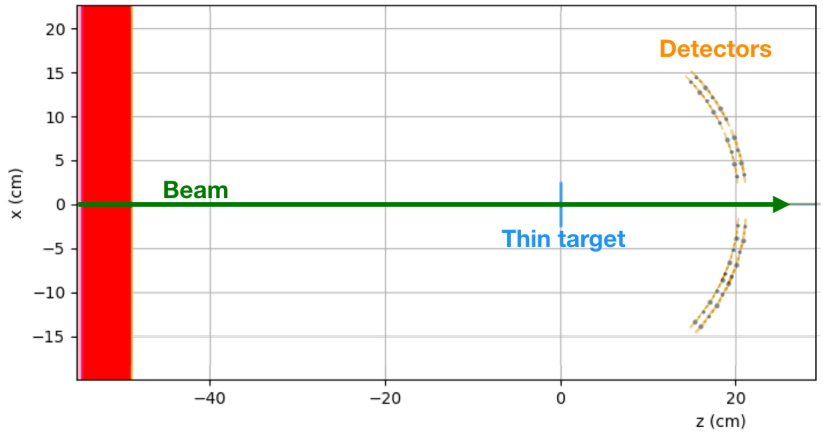

Figure 5.23. Set up of the GANIL experiment [93] simulated with the FRED code. The thin target is made of graphite with the same thickness (250 μm) and density (0.0411 g/cm^2) as the target used in the experiment. The detector at 82 cm of distances from the target is out of this image.

Currently, those are the only experiments that provide information about the double differential cross-section of ^{12}C beam fragmentation at energy compatible with the PT treatments.
Since those data have been used to develop the fragmentation model described in this thesis (Par. 4.3.4 and Par. 4.3.4), we tested as first check the agreement of the model with data.
The experiment consisted in a ^{12}C beam at 94.6 ± 0.09 MeV/u sent on different thin targets (C, CH_2, Al, Al_2O_3, ^{nat}Ti, PMMA ($C_5H_8O_2$)). For the charged particles detection, the setup consisted of four $\Delta E_{thin}/\Delta E_{thick}/E$ telescopes mounted two by two on two stages that allow rotation inside the vacuum chamber from 0° to 43° with 2° steps at a distance of 204 mm behind the target. A fifth telescope was mounted downstream, at a fixed angle of 4° and a distance of 820 mm behind the target. The set-up has been reproduced with a FRED simulation (Fig. 5.23) and the code has collected information only about the secondary fragments which crossed the detectors with the threshold energy reported in the paper of GANIL (Tab. 5.1).

Table 5.1. Energy threshold of the GANIL experiment [93].

Isotopes	^{1}H	^{2}H	^{3}H	^{3}He	^{4}He	^{6}He	^{6}Li	^{7}Li	
$\mathbf{E}_{thr}$ **[MeV]**	4.0	5.2	6.1	14.2	16.0	18.6	29.9	31.7	
Isotopes	^{7}Be	^{8}Be	^{10}Be	^{8}B	^{10}B	^{11}B	^{10}C	^{11}C	^{12}C
$\mathbf{E}_{thr}$ **[MeV]**	44.3	48.6	50.5	60.6	65.8	68.1	81.3	84.	86.9

For this thesis, a simulation of a ^{12}C beam (2×10^8 primary particles) on a target of ^{12}C has been compared with data. In particular, the probabilities of emission of each fragment and the double differential cross-sections have been compared.
In Fig. 5.24 it is possible to observe the comparison between the measured and simulated probability of emission of each possible fragment in linear and logarithmic scale. As explained in Par. 4.3.4, the iterative optimization has been used to obtain sampling probabilities as close as possible to GANIL results, conserving mass, charge and energy. All fragments are within the uncertainties of experimental data except for ^{1}H and ^{4}He. From this histogram, it is possible to observe that the most common fragments emitted are protons and ^{4}He followed by the other lighter fragments. Neutrons, which are almost the same as protons, are not shown because in the GANIL experiment only charged fragments were detected. For what concern ^{12}C, even if in the experimental data the cross-section of production of this isotope is reported, physically it is not a production of fragmentation but a projectile scattering. For this reason, it is not shown in the figure.
Another aspect that can emerge from a comparison with GANIL data is an agreement in the angular and energy distribution. From Fig. 5.25 to Fig. 5.29, the angular distributions of different ions from the fragmentation on carbon target is shown. The angles in the abscissa axis are the angles of production with respect of the beam direction.
The fragmentation cross-sections has been obtained in the following way:

$$\frac{d\sigma}{d\Omega}({}^{A}_{Z}X) = \frac{N_{{}^{A}_{Z}X} \times A_{target}}{N_{primary} \times \Omega \times \rho \times th \times N_A}, \tag{5.3}$$

where $N_{{}^{A}_{Z}X}$ is the number of ${}^{A}_{Z}X$ fragments detected, A and Z are respectively the mass and the charge of the fragment, $A_{target} = 12$ is the target mass, $N_{primary}$ is the

number of incident carbon nuclei, Ω =6.6 sr (or 0.43 for the detector at 4 degrees) is the solid angle of the detector, $\rho \times th = 0.0411$ g/cm^2 is the target area density and N_a is the Avogadro's number.

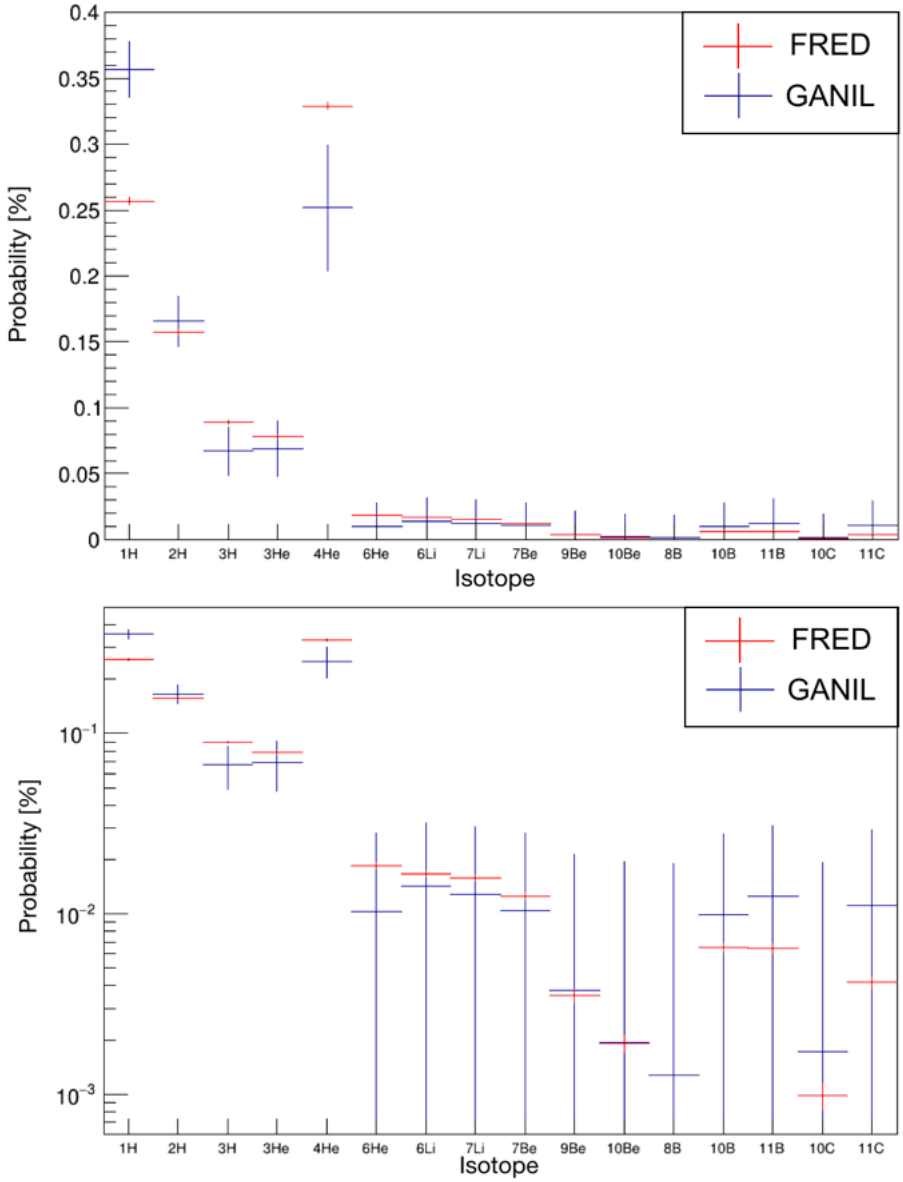

Figure 5.24. Production probability per isotope resulting from the fragmentation on a carbon target in linear (top) and logarithmic (bottom) scale. In blue, the probabilities extrapolated from the production cross-section of GANIL experiment [93] with the correspondent uncertainties are shown. The probability obtained from a FRED simulation, in the same condition of the experiment, is shown in red.

The behaviour of the angular distribution of the FRED simulation and the GANIL data are similar. They are sharp at the smallest angle and decrease more steeply as the atomic number increases. There are more evident differences at larger angles, where the statistic is lower. Helium-6 is the only exception in the GANIL distributions, it has a peak at 7 degrees instead of 4. Since there is no physical explanation for this shift of the peak, I suppose that during the experiment there were some difficulties to detect ^{6}He with the most distant detector (4°).
Those plots suggest that extracting the angular distribution of hydrogen fragments directly from the Gaussian-exponential distribution (Eq. 4.44) both for target and projectile fragmentation is the correct modality. As explained in Par. 4.3.4, a bidimensional fit has been performed on GANIL data and the code extracts from a Gaussian or exponential distribution to sample the projectile or the target fragmentation respectively. An exception has been made for the lighter fragments because, as one can observe from Fig. 4.18, Fig. 4.19 and Fig. 4.20, for them the difference between the exponential and Gaussian distribution is less evident.

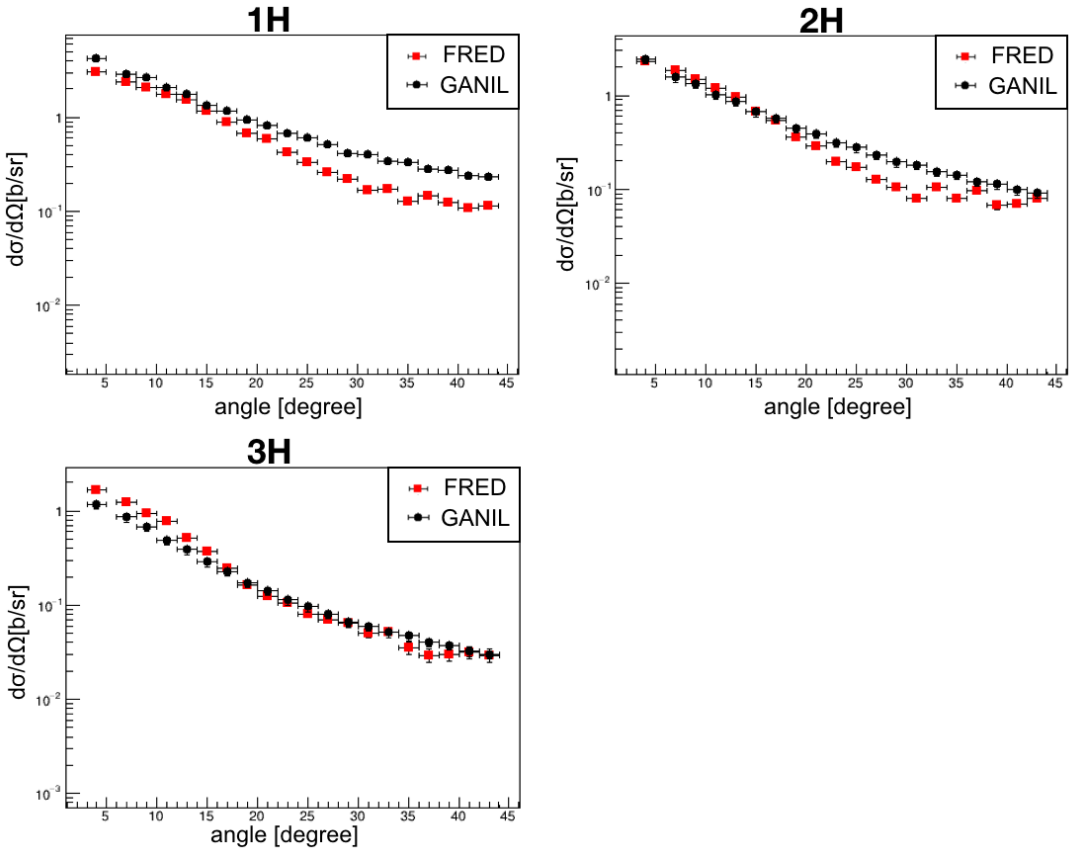

Figure 5.25. Angular distributions for fragments resulting from the ^{12}C fragmentation on carbon target. Each graph represents the distribution of an isotope of hydrogen. In black data obtained from the GANIL experiment [93], in red results of the FRED simulation in same condition of the experiment.

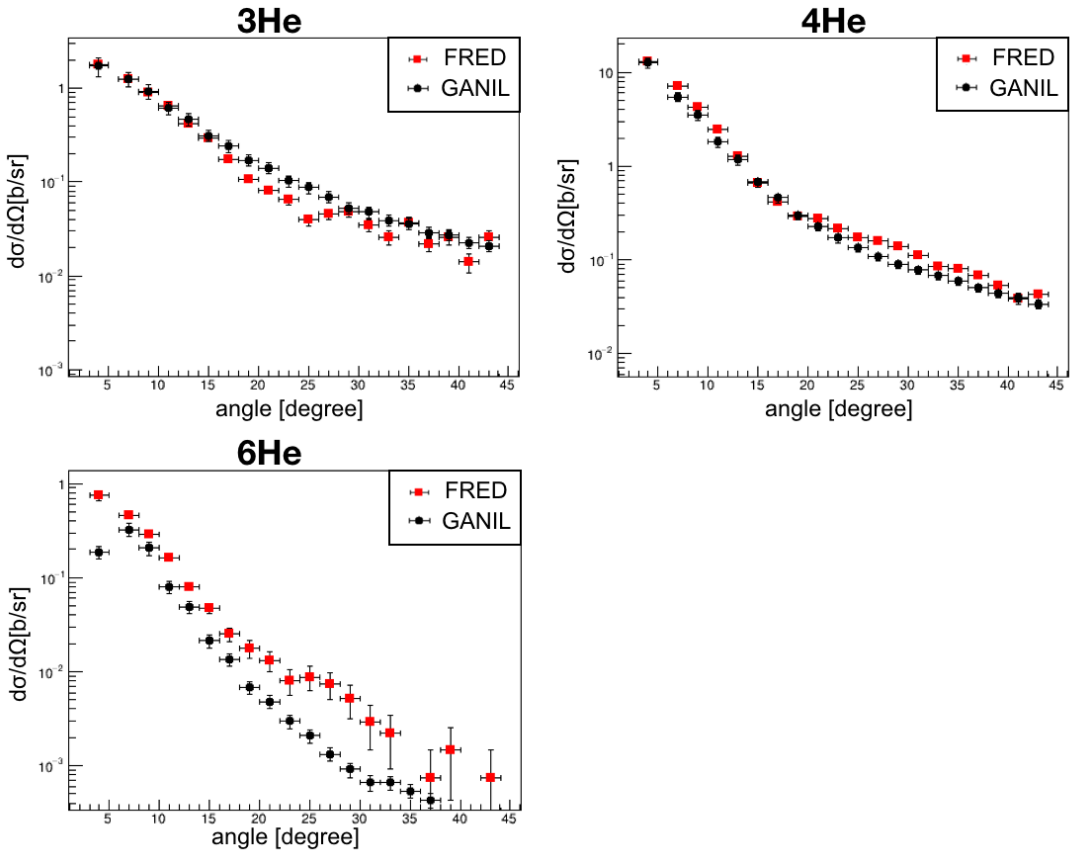

Figure 5.26. Angular distributions for fragments resulting from the ^{12}C fragmentation on carbon target. Each graph represents the distribution of an isotope of helium. In black data obtained from the GANIL experiment [93], in red results of the FRED simulation in same condition of the experiment.

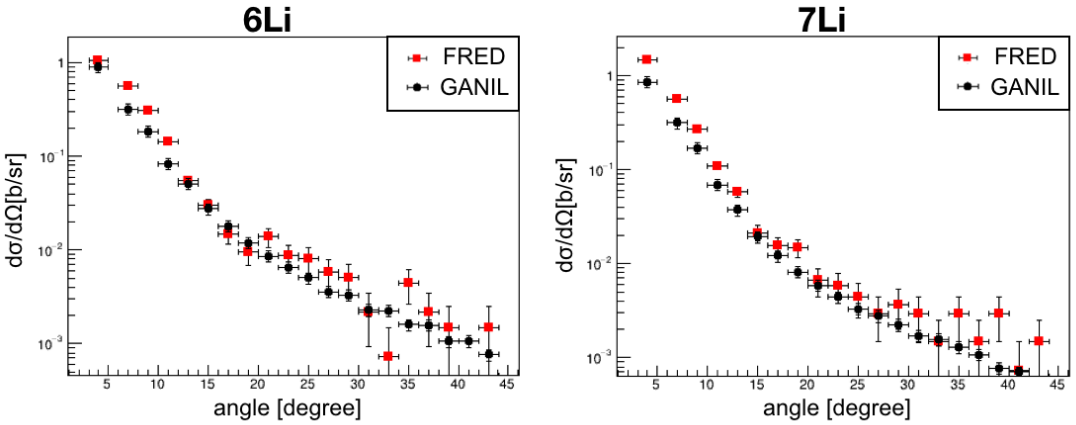

Figure 5.27. Angular distributions for fragments resulting from the ^{12}C fragmentation on carbon target. Each graph represents the distribution of an isotope of lithium. In black data obtained from the GANIL experiment [93], in red results of the FRED simulation in same condition of the experiment.

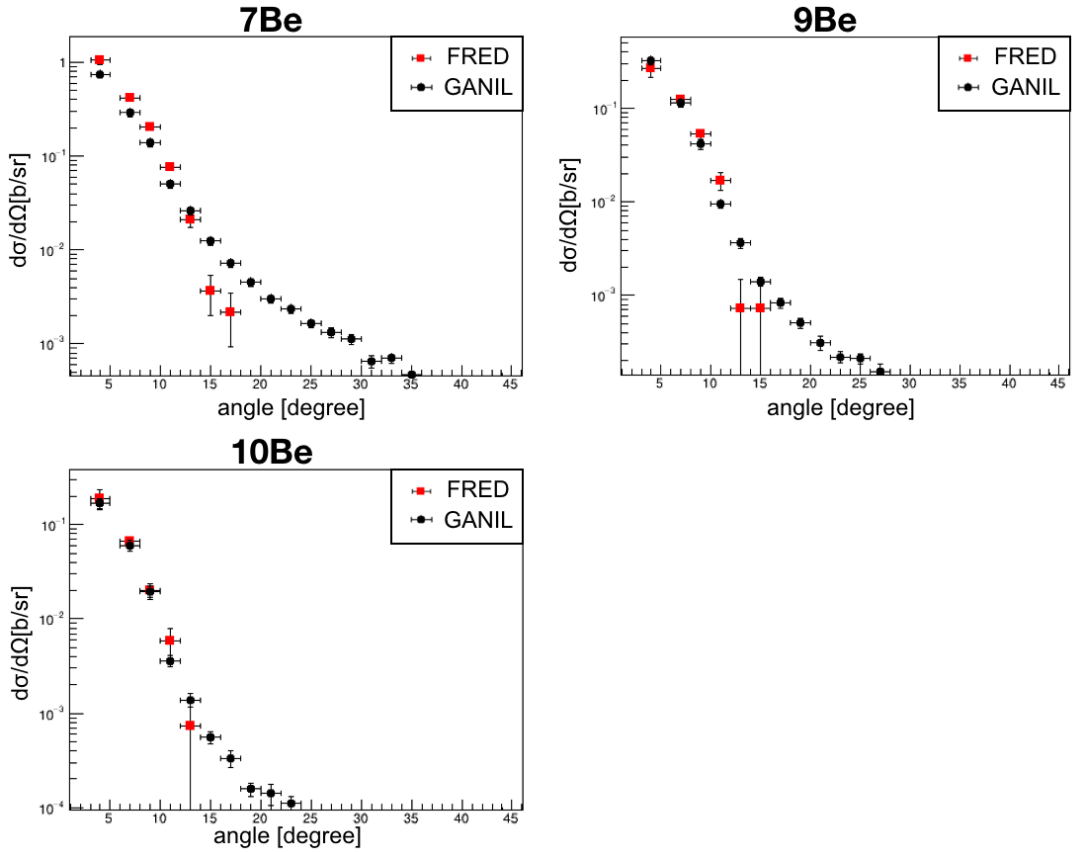

Figure 5.28. Angular distributions for fragments resulting from the ^{12}C fragmentation on carbon target. Each graph represents the distribution of an isotope of beryllium. In black data obtained from the GANIL experiment [93], in red results of the FRED simulation in same condition of the experiment.

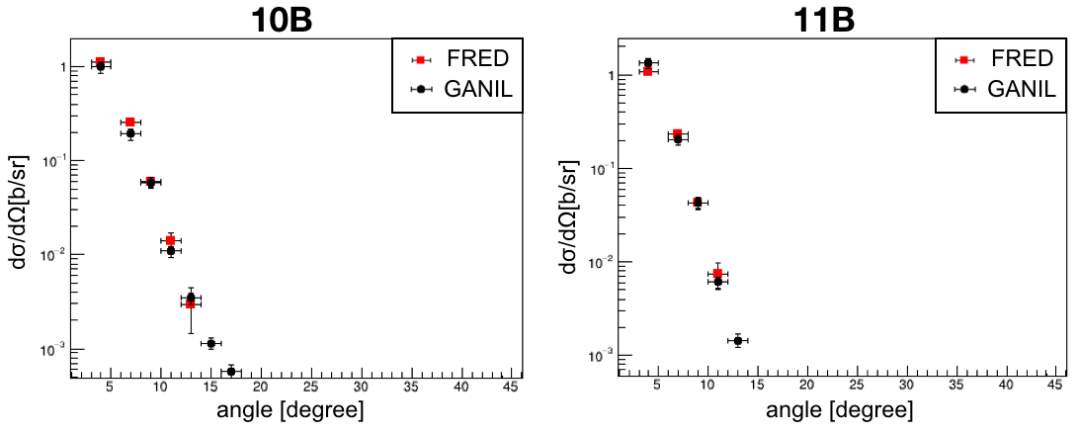

Figure 5.29. Angular distributions for fragments resulting from the ^{12}C fragmentation on carbon target. Each graph represents the distribution of an isotope of boron. In black data obtained from the GANIL experiment [93], in red results of the FRED simulation in same condition of the experiment.

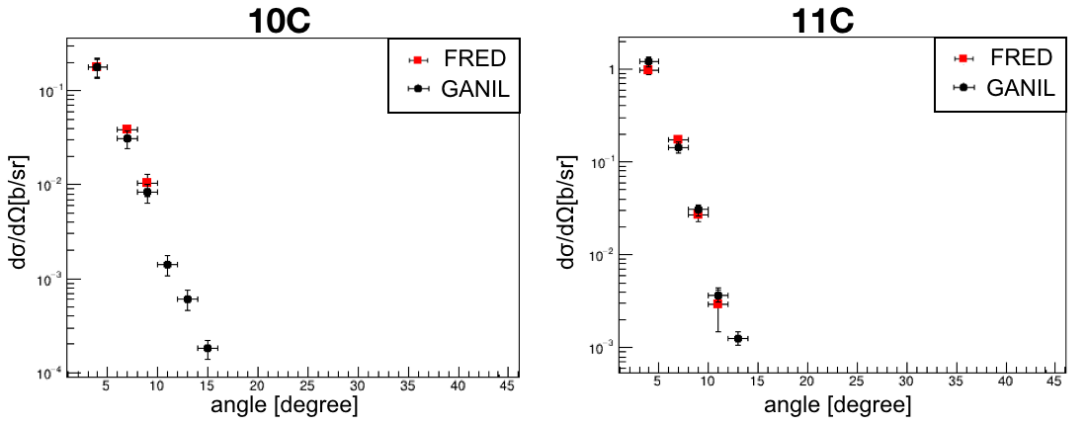

Figure 5.30. Angular distributions for fragments resulting from the ^{12}C fragmentation on carbon target. Each graph represents the distribution of an isotope of carbon. In black data obtained from the GANIL experiment [93], in red results of the FRED simulation in same condition of the experiment.

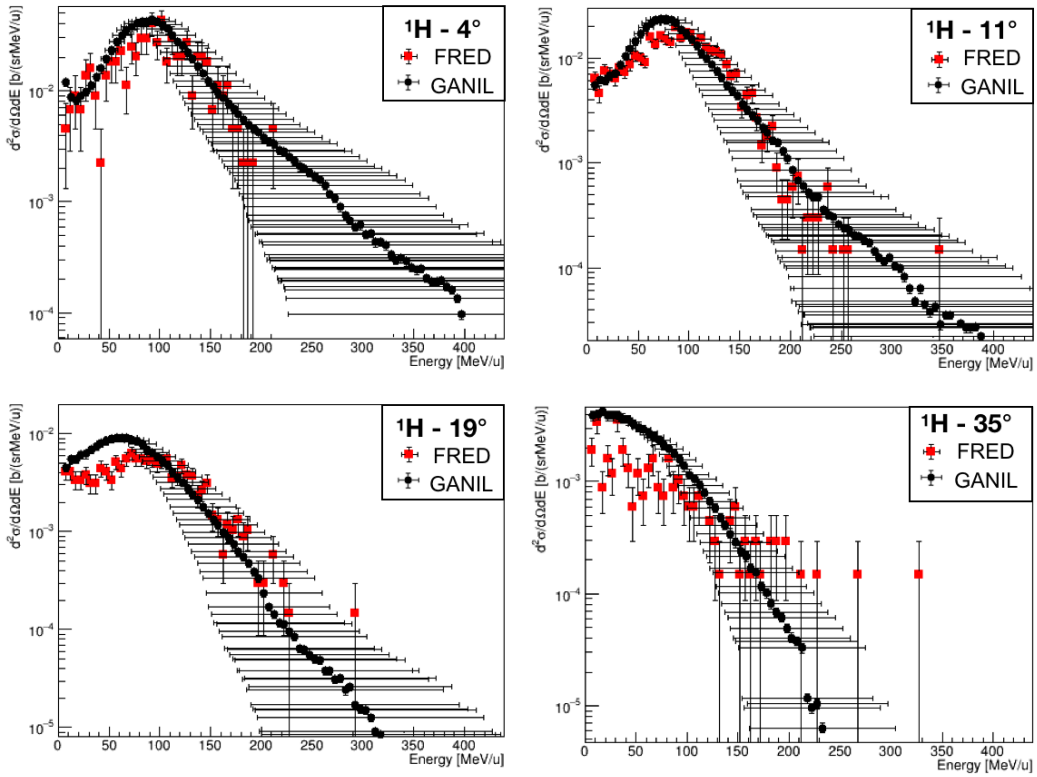

Figure 5.31. ^{1}H energy distribution for a carbon target at different angles. With circles, results of the GANIL experiment [93] with the correspondent uncertainties are shown. The energy distribution obtained from a FRED simulation, in the same condition of the experiment, is shown with squares. In the FRED plot, the uncertainties on energy are smaller than the marker (5 MeV).

.

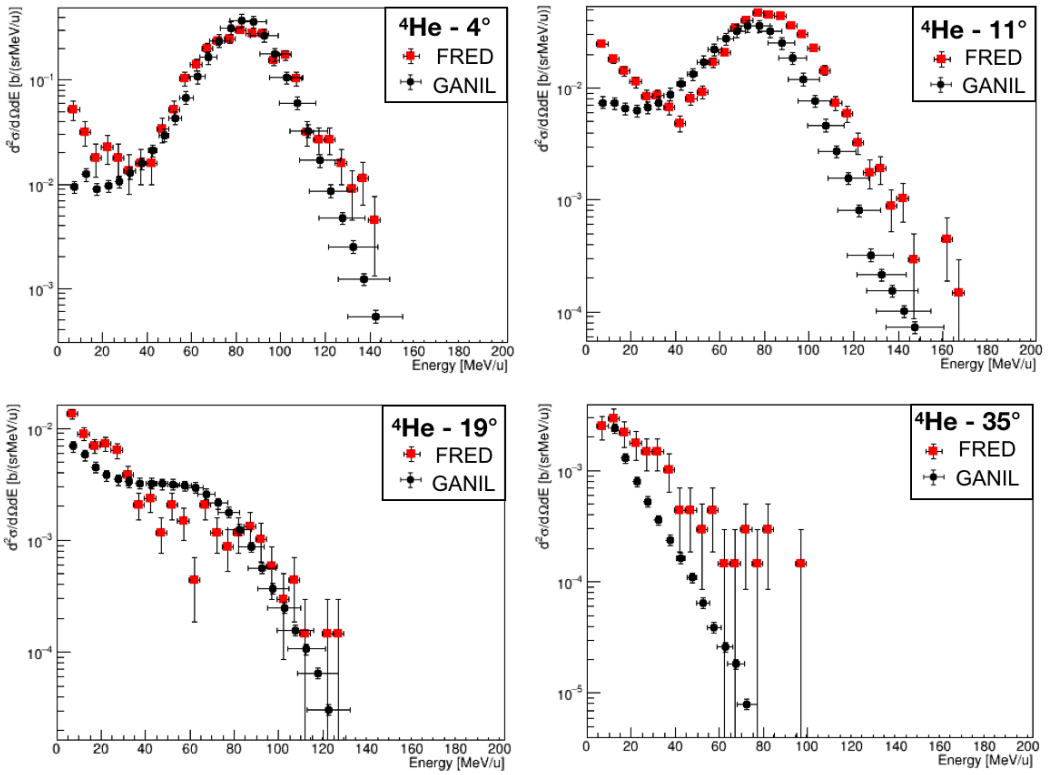

Figure 5.32. ^{4}He energy distribution for a carbon target at different angles. With circles, results of the GANIL experiment [93] with the correspondent uncertainties are shown. The energy distribution obtained from a FRED simulation, in the same condition of the experiment, is shown with squares.

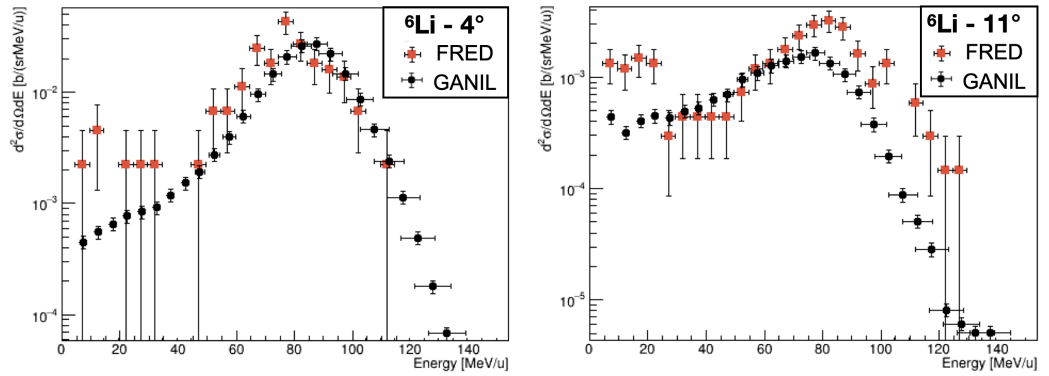

Figure 5.33. ^{6}Li energy distribution for a carbon target at different angles. With circles, results of the GANIL experiment [93] with the correspondent uncertainties are shown. The energy distribution obtained from a FRED simulation, in the same condition of the experiment, is shown with squares.

The last comparison with GANIL data is about the energy distributions at different angles. In Fig. 5.31, Fig. 5.32 and Fig. 5.33 the energy distributions at 4, 11, 19 and 35 degrees for 3 isotopes are shown. To match the experimental results,

the fragmentation cross-sections has been obtained in the following way:

$$\frac{d\sigma}{d\Omega}({}^{A}_{Z}X,\theta) = \frac{N_{{}^{A}_{Z}X,\theta} \times A_{target}}{N_{primary} \times \Omega \times \rho \times th \times N_A \times \Delta E}, \tag{5.4}$$

where $N_{{}^{A}_{Z}X,\theta}$ is the number of ${}^{A}_{Z}X$ fragments detected at the angle $\theta \pm 1°$, A and Z are respectively the mass and the charge of the fragment, $A_{target} = 12$ is the target mass, $N_{primary}$ is the number of incident carbon nuclei, Ω =6.6 sr (or 0.43 for the detector at 4 degrees) is the solid angle of the detector, $\rho \times th = 0.0411$ g/cm^2 is the target area density, $\Delta E = 5$ MeV is the energy interval of detection and N_A is the Avogadro's number.
The main feature to be highlighted from this comparison is that the distributions are peaked at the same energy, which is, as expected, almost the same energy per nucleon of the beam. On the other hand for the distributions at 11 degrees are slightly shifted comparing FRED simulation and GANIL data. Observing GANIL double cross-section data, it is evident that for some angles (for example 11 degrees) the distribution is not coherent with one of the other angles. To obtain a more physically proper model, in FRED this shift has been corrected.
Another important aspect to observe in those distributions is that in FRED there is a small peak at small energy for helium fragments not present in GANIL data. Those energies are principally due to the target fragmentation. This discrepancy can be the consequence of the fact that in the FRED code a mass and charge conservation is required but using cumulative obtained to mimic the GANIL cross-section. However, the experimental cross-sections are only with fragments that have enough energy to be detected and so they do not respect mass and charge conservation.

5.2.2 Haettner experiment

In the Haettner experiment [15], the characteristics of secondary charged particles at various depths of water were investigated experimentally using ^{12}C ion beams of 200 and 400 MeV/u delivered by the heavy-ion synchrotron SIS-18 at GSI Darmstadt.

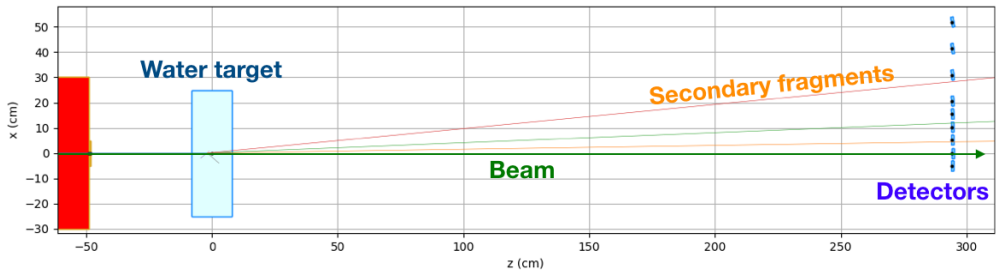

Figure 5.34. Set up of the Haettner experiment [15] simulated with the FRED code. The water target was depth 15.9 cm and the detectors were mounted on a linear drive at 2.94 m distance from the mid-target position.

Energy spectra and yields were recorded at lab angles of 0°-10° and at different water depths. In this thesis, the purpose of this comparison is to observe angular distribution and energy spectra of secondary fragments emitted by a 400 MeV/u beam of ^{12}C in water.
The set-up of the experiment has been simulated with FRED (Fig. 5.34). The water target with a depth of 15.9 cm has been chosen to observe the agreement of

the secondary fragment production in the plateau region of the dose profile. The detectors were mounted on a linear drive at 2.94 m distance from the mid-target position. The linear drive permitted to move the detector in the lateral direction with respect to the beam axis, covering an angular range of -1° to +10° between target center and detector position. To assure that the detector was always oriented perpendicular to the target center, the linear motion was mechanically coupled to a corresponding rotation of the detector.
In Fig. 5.35 the comparison between FRED and data of the angular distribution of charged fragments produced by 400 MeV/u ^{12}C ions in a water target in the plateau region is shown. The distribution of helium, lithium and beryllium isotopes are in excellent agreement and are for almost all angles within the experimental uncertainties.
For what concern hydrogen isotopes there are fewer hydrogen isotopes at small angles. This highlights the necessity of improving the angle scaling with a beam energy of hydrogen isotopes.

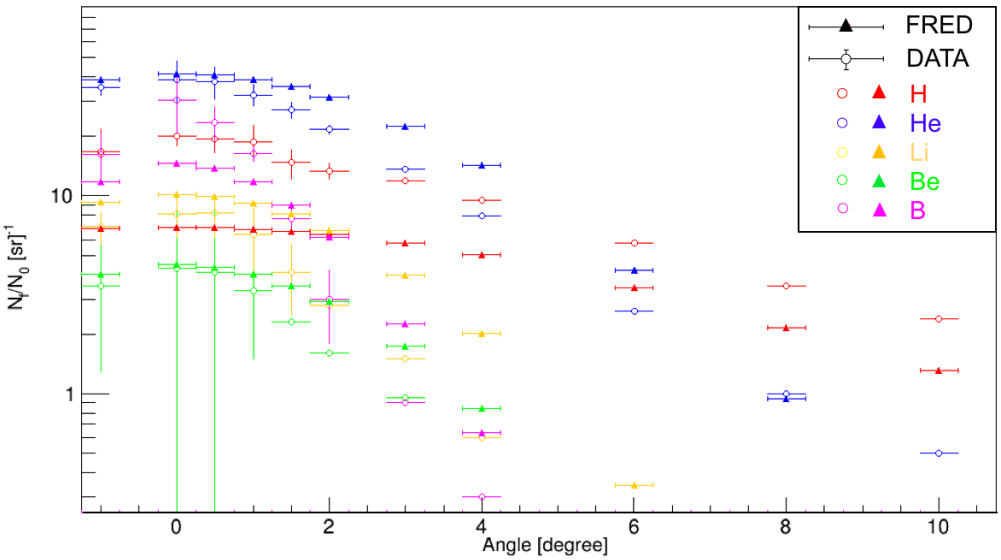

Figure 5.35. Angular distributions of charged fragments produced by 400 MeV/u ^{12}C ions in water targets of 15.9 cm thickness. The uncertainties in the number of fragment in the FRED distribution is smaller that the marker.

In fig. 5.36, energy spectra of nuclear fragments detected at 2° escaping from the 15.9 cm depth water target simulated with FRED and obtained in the experiment are shown. It is possible to observe that the shape of the distributions is almost the same but the distributions relatively to FRED simulation are slightly peaked at smaller energies. As observed for angular distribution, also in this situation this shift in energy can be solved by improving the energy scaling for fragments emitted. It must be stressed that the energy of 400 MeV/u is an upper limit of the energy range of interest in PT. Actually, a TPS rarely requires a beam of 400 MeV/u since the penetration is too high for a tumor unless the patient has an above-average volume. For this reason, developing the model, we have taken more attention to the agreement at lower energies. However, in absence of new experimental data, this comparison has been useful to understand possible mistakes of the code in the scaling of energy and angles of the new fragments emitted.

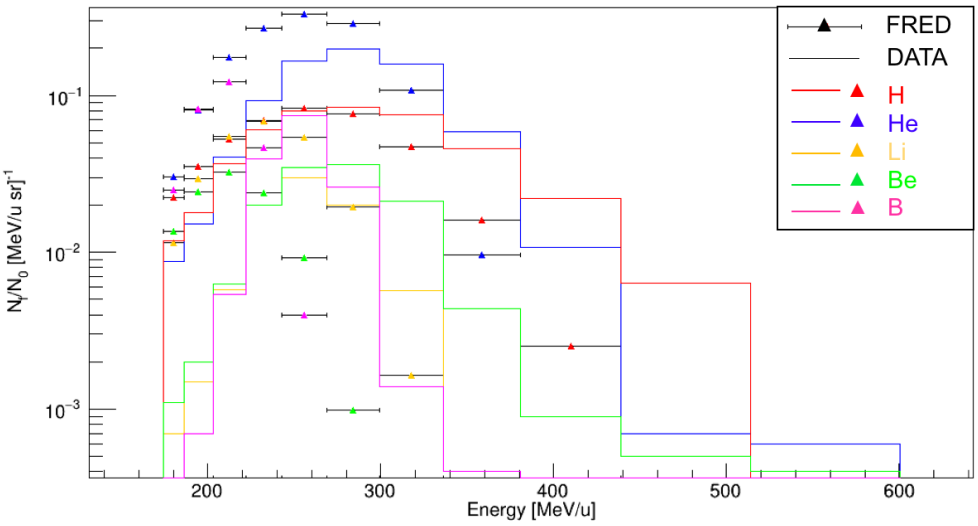

Figure 5.36. Energy spectra of secondary fragments from a 400 MeV/u ^{12}C beam recorded at 2° relative to the beam axis at a depth of 15.9 cm corresponding to the plateau region of the Bragg curve.

Conclusions

In this thesis, the development of a fast-MC simulating the carbon treatment in particle therapy, with an entirely new nuclear interaction model of carbon on light target nuclei, has been presented. The model has been developed to be implemented in the GPU based MC code, FRED. For this reason, in developing the algorithms the goal has been to balance accuracy, calculation time and GPU execution guidelines. In particular, maximum attention has been given to physical processes relevant for dose and RBE-weighted dose computation. Moreover, where possible, look-up tables have been implemented instead of performing an explicit calculation in view of the GPU implementation.
Some aspects of the interaction of carbon ions with matter are analogous to the ones already used in FRED for proton beams. In particular, for ionization energy loss and multiple scattering, only a few adjustments were necessary. On the contrary, the nuclear model was built from scratch. The approach has been to develop the nuclear model parameterizing existent data and applying physical scaling in the energy range where the data are missing. The elastic cross-section has been obtained from *ENDF/B-VII* data [88] while the calculation of the non-elastic cross-section was based on results reported on *Tacheki* [89], *Zhang* [90] and *Kox* [91][92] papers. Data used for the sampling of the combination of emitted fragments, energy and angle distributions, are relatives to the *Dudouet* [93] and *Divay* [94] experiments. To fill the gaps in the experimental data, an intercomparison between FRED and the full-MC FLUKA has been of help to check the adopted scaling.
The implementation of the LEM I model for the calculation of the RBE and RBE-weighted dose has been presented as well. This calculation is of fundamental importance for the application of the fast-MC code FRED in clinical practice. The user can easily change the α and β parameters of the LEM I model substituting an input table. In this way, it will be possible to use the parameters decided by the specific medical structure.
The model has been tested against the full-MC code FLUKA, commonly used in particle therapy, and then with two of the few experiments that it is possible to find in literature.
The agreement with FLUKA is excellent, especially for lower energies. In particular, the agreement with the full-MC is always within 2.5% of the total dose deposited in single pencil beams in the 100-300 MeV/u energy range. Simulating a SOBP composed of 225 beams per slice, the agreement of the dose distribution is within 1.7% and the gamma-index 2mm/3% test shows a pass rate of 93.3%. The RBE and RBE-weighted dose is in good agreement with FLUKA as well.
To compare FRED with data, the first experiment which was simulated was the one used to benchmark the model: the Ganil experiment of *Dudouet* [93] and *Divay* [94]. Angular and energy distributions show excellent agreement between the fast-MC and data. After that, the Haettner experiment [15] has been reproduced. In this case, the agreement is not as strong as the first simulated experiment. However, the

energy of this experiment, 400 MeV/u, is close to an upper limit of the energy range used in PT. In absence of new experimental data, this comparison has been useful for understanding possible mistakes in the code when scaling energy and angles of the new emitted fragments.
With the advent of new experiments focused on nuclear fragmentation, such as the FOOT experiment [96][97][98][99][100], it will be possible to make more comparisons with different set-ups and energies and, especially thanks to FOOT, to have more information about the target fragmentation.
Presently, the implementation of the ^{12}C model is satisfactory. The next step will be to port the model on GPU. After that, the accuracy of FRED dose recalculation will be compared with the CNAO TPS for carbon therapy to achieve clinical validation.

Bibliography

[1] Schiavi A et al. “Fred: a GPU-accelerated fast-Monte Carlo code for rapid treatment plan recalculation in ion beam therapy”. In: *Phys Med Biol* 62.18 (2017), pp. 7482–7504. DOI: 10.1088/1361-6560/aa8134.

[2] Bethe H and Ashkin J. *Experimental Nuclear Physics*. Ed. by E Segré. Vol. 1. 1953.

[3] *Particle Data Group. Passage of particles through matter*. 2013. URL: http//:pdg.lbl.gov/2013/reviews/rpp2013-rev-passage-particles-matter.pdf.

[4] Seltzer S M and Berger M J. “Energy loss straggling of protons and mesons: tabulation of the Vavilov distribution.” In: *Studies in Penetration of Charged Particles in Matter. Washington DC: National Academy of Sciences–National Research Council* (1964). Provided by the SAO/NASA Astrophysics Data System, 187–203. URL: https://ui.adsabs.harvard.edu/abs/1964spcp.conf..187S.

[5] Landau L. “On the energy loss of fast particles by ionization”. In: *J. Phys. (USSR)* 8 (1944), pp. 201–205. DOI: 10.1016/b978-0-08-010586-4.50061-4.

[6] Vavilov P V. “Ionization losses of high-energy heavy particles”. In: *Sov. Phys. JETP* 5.4 (1957), p. 749.

[7] Schardt D et al. “Heavy-ion tumor therapy: physical and radiobiological benefits”. In: *Rev Mod Phys* 82 (2010), pp. 383–425. DOI: 10.1103/RevModPhys.82.383.

[8] Molierè G. “Theorie der Streuung schneller geladener Teilchen II e Mehrfachund Vielfachstreu-ung.” In: *Z. Naturforsch.* 3.a (1948), pp. 78–97. DOI: 10.1515/zna-1948-0203.

[9] Bethe H A. “Molière’s theory of multiple scattering”. In: *Phys Rev* 89 (1953), 1256–1266. DOI: 10.1103/PhysRev.89.1256.

[10] Fano U. “Inelastic Collisions and the Molière Theory of Multiple Scattering”. In: *Phys Rev* 93 (1954), pp. 117–120. DOI: 10.1103/PhysRev.93.117.

[11] Highland L. “Some practical remarks on multiple scattering”. In: *Nuclear Instruments and Methods* 129.2 (1975), pp. 497–499. DOI: 10.1016/0029-554X(75)90743-0.

[12] Serber R. “Nuclear reactions at high energies”. In: *Phys Rev* 72 (1947), pp. 1114–1115. DOI: 10.1103/PhysRev.72.1114.

[13] Gottschalk B. *Physics of proton interactions in matter - Proton Therapy Physics*. Ed. by FL: Taylor Harald Paganetti (Boca Raton and Francis Group). 2012, pp. 19–60.

[14] Cussol D. "Nuclear Physics and Hadron Therapy". In: *La Colle sur Loup: Lectures at Ecole Joliot Curie* (2011), p. 12. DOI: in2p3-00623351f.

[15] Haettner E et al. "Experimental study of nuclear fragmentation of 200 and 400 MeV/u ^{12}C ions in water for applications in particle therapy". In: *Phys Med Biol* 58.23 (2013), 8265–8279. DOI: 10.1088/0031-9155/58/23/8265.

[16] Allisy A et al. "ICRU Report 51: Quantities and units in radiation protection dosimetry". In: *Journal of the International Commission on Radiation Units and Measurements* 26 (1993). DOI: 10.1093/jicru/os26.2.Report51.

[17] Lin S H. "The utility of Proton Beam Therapy with Concurrent Chemotherapy for the Treatment of Esophageal Cancer". In: *Cancer* 3 (2011), pp. 4090–4101. DOI: 10.3390/cancers3044090.

[18] Paganetti H et al. "Relative biological effectiveness (RBE) values for proton beam therapy". In: *Int J Radiat Oncol Biol Phys* 53 (2002), pp. 407–421. DOI: 10.1016/s0360-3016(02)02754-2.

[19] Hall E. *Radiobiology for the radiologist*. Lippincott Williams & Wilkins, 2006. URL: https://books.google.it/books?id=6HhjwRyqBzgC.

[20] Tiganelli W et al. "Kill-painting of hypoxic tumours in charged particle therapy". In: *Sci Rep* 5 (2015), p. 17016. DOI: https://doi.org/10.1038/srep17016.

[21] Sokol O et al. "Oxygen beams for therapy: advanced biological treatment planning and experimental verification". In: *Phys Med Biol* 62 (2017), pp. 7798–7813. DOI: 10.1088/1361-6560/aa88a0.

[22] Blakely E A et al. "Inactivation of human kidney cells by high energy monoenergetic heavy-ion beams". In: *Rad Res* 80 (1979), pp. 122–160. DOI: 10.2307/3575121.

[23] *Particle therapy facilities in clinical operation (update July 2020)*. Particle Therapy Co-Operative Group. 2020. URL: https://www.ptcog.ch/index.php/facilities-in-operation.

[24] *Particle therapy facilities under construction (update July 2020)*. Particle Therapy Co-Operative Group. 2020. URL: https://www.ptcog.ch/index.php/facilities-under-construction.

[25] Peach K et al. "Accelerator science in medical physics". In: *The British Journal of Radiology* 84 (2011), pp. 4–10. DOI: 10.1259/bjr/16022594.

[26] Wiedemann H. *Particle Accelerator Physics*. Springer Nature, 2015. DOI: 10.1007/978-3-319-18317-6.

[27] Flanz J. "Accelerators for Proton and Ion Therapy". In: *Proton and Carbon Ion Therapy* (2013). Ed. by M C Ma and T Lomax, pp. 15–28.

[28] Owen H, Lomax A, and Jolly S. "Current and future accelerator technologies for charged particle therapy". In: *Nuclear Instruments and Methods in Physics Research Section A: Accelerators, Spectrometers, Detectors and Associated Equipment* 809 (2016), pp. 96–104. DOI: 10.1016/j.nima.2015.08.038.

[29] Myers S, Degiovanni A, and Farr J B. "Future Prospects for Particle Therapy Accelerators". In: *Reviews of Accelerator Science and Technology* 10 (2019), pp. 49–92. DOI: 10.1142/S1793626819300056.

[30] Suh H S et al. "Magnet design for proton and carbon ion synchrotron for cancer therapy". In: *J Korean Phys Soc* 56 (2010), pp. 1947–1952. DOI: 10.3938/jkps.56.1947.

[31] Rossi S. "The National Centre for Oncological Hadrontherapy (CNAO): Status and perspectives". In: *Physica Medica* 31.4 (2015), pp. 333–351. DOI: 10.1016/j.ejmp.2015.03.001.

[32] Jia X et al. "GPU-based fast Monte Carlo dose calculation for proton therapy". In: *Phys Med Biol* 57 (2012), 7783–7797. DOI: 10.1088/0031-9155/57/23/7783.

[33] Paganetti H. "Range uncertainties in proton therapy and the role of Monte Carlo simulations". In: *Phys Med Bio* 57.11 (2012), pp. 99–117. DOI: 10.1088/0031-9155/57/11/r99.

[34] Paganetti H et al. "Clinical implementation of full Monte Carlo dose calculation in proton beam therapy". In: *Phys Med Bio* 53 (2008), pp. 4825–53. DOI: doi:10.1088/0031-9155/53/17/023.

[35] Jia X et al. "GPU-based high-performance computing for radiation therapy". In: *Phys Med Biol* 59.4 (2014), pp. 151–82. DOI: 10.1088/0031-9155/59/4/R151.

[36] Jia X et al. "GPU-based fast cone beam CT reconstruction from undersampled and noisy projection data via total variation". In: *Phys Med Biol* 37 (2010), pp. 3441–3441. DOI: 10.1118/1.3469447.

[37] Giantsoudi D et al. "Validation of a GPU-based Monte Carlo code (gPMC) for proton radiation therapy: clinical cases study". In: *Phys Med Biol* 60.6 (2015), pp. 2257–69. DOI: 10.1088/0031-9155/60/6/2257.

[38] Xu F and Mueller K. "Accelerating popular tomographic reconstruction algorithms on commodity PC graphics hardware". In: *IEEE Trans Nucl Sci* 52 (2005), pp. 654–63. DOI: 10.1109/TNS.2005.851398.

[39] Sharp G C et al. "GPU-based streaming architectures for fast cone-beam CT image reconstruction and demons deformable registration". In: *Phys Med Biol* 52 (2007), 5771–83. DOI: 10.1088/0031-9155/52/19/003.

[40] Yan G et al. "Fast cone-beam CT image reconstruction using GPU hardware". In: *J X-Ray Sci Technol* 16 (2008), 225–34.

[41] Gu X et al. "GPU-based ultra fast dose calculation using a finite size pencil beam model". In: *Phys Med Biol* 54 (2009), 6287–97. DOI: 10.1088/0031-9155/54/20/017.

[42] Gu X et al. "Implementation and evaluation of various demons deformable image registration algorithms on a GPU". In: *Phys Med Biol* 55 (2010), 207–19. DOI: 10.1088/0031-9155/55/1/012.

[43] Hissoiny S et al. "Fast convolution-superposition dose calculation on graphics hardware". In: *Med Phys* 36 (2009), 1998–2005. DOI: 10.1118/1.3120286.

[44] Men C et al. "GPU-based ultra fast IMRT plan optimization". In: *Phys Med Biol* 54 (2009), 6565–73. DOI: 10.1088/0031-9155/54/21/008.

[45] Men C et al. "GPU-based ultra-fast direct aperture optimization for online adaptive radiation therapy". In: *Phys Med Biol* 55 (2010), 4309–19. DOI: 0.1088/0031-9155/55/15/008.

[46] Men C et al. "Ultrafast treatment plan optimization for volumetric modulated arc therapy (VMAT) ". In: *Med Phys* 37 (2010), 5787–91. DOI: 10.1118/1.3491675.

[47] Samant S S et al. “High performance computing for deformable image registration: towards a new paradigm in adaptive radiotherapy”. In: *Med Phys* 35 (2008), 3546–53. DOI: 10.1118/1.2948318.

[48] Pshenichnov I, Mishustin I, and Greiner W. “Distributions of positron-emitting nuclei in proton and carbon-ion therapy studied with GEANT4”. In: *Phys Med Biol* 51 (2006), pp. 6099–6112. DOI: 10.1088/0031-9155/51/23/011.

[49] Parodi K et al. “In-beam PET measurements of β^+ radioactivity induced by proton beams”. In: *Phys Med Biol* 47 (2002), 21–36. DOI: 10.1088/0031-9155/47/1/302.

[50] Fiorina E et al. “Monte Carlo simulation tool for online treatment monitoring in hadrontherapy with in-beam PET: A patient study”. In: *Physica Medica* 51 (2018). DOI: 10.1016/j.ejmp.2018.05.002.

[51] Ferrero V et al. “Online proton therapy monitoring: clinical test of Silicon-photodetector-based in-beam PET”. In: *Scientific Reports* 8 (2018), p. 4100. DOI: 10.1038/s41598-018-22325-6.

[52] Knopf A et al. “Systematic analysis of biological and physical limitations of proton beam range verification with offline PET/CT scans”. In: *Phys Med Biol* 54 (2009), pp. 4477–95. DOI: 10.1088/0031-9155/54/14/008.

[53] Bauer J et al. “Implementation and initial clinical experience of offline PET/CT-based verification of scanned carbon ion treatment”. In: *Radiother Oncol* 107 (2013), pp. 218 –226. DOI: 10.1016/j.radonc.2013.02.018.

[54] Nishio T et al. “The Development and Clinical Use of a Beam ON-LINE PET System Mounted on a Rotating Gantry Port in Proton Therapy”. In: *Int J Radiat Oncol Biol Phys* 76 (2010), pp. 277–286. DOI: 10.1016/j.ijrobp.2009.05.065.

[55] Zhu X et al. “Monitoring proton radiation therapy with in-room PET imaging”. In: *Phys Med Bio* 56 (2011), pp. 4041–4057. DOI: 10.1088/0031-9155/56/13/019.

[56] Pinto M et al. “Absolute prompt-gamma yield measurements for ion beam therapy monitoring”. In: *Phys Med Biol* 60 (2015), pp. 565–594. DOI: 10.1088/0031-9155/60/2/565.

[57] Smeets J et al. “Prompt gamma imaging with a slit camera for real time range control in particle therapy”. In: *Phys Med Biol* 57 (2012), 3371–3405. DOI: 10.1088/0031-9155/57/11/3371.

[58] Piersanti L et al. “Measurement of charged particle yields from PMMA irradiated by a 220 MeV/u ^{12}C beam”. In: *Phys Med Bio* 59 (2014), pp. 1857–1872. DOI: 10.1088/0031-9155/59/7/1857.

[59] Muraro S et al. “Monitoring of Hadrontherapy Treatments by Means of Charged Particle Detection”. In: *Frontiers in Oncology* 6 (2016), p. 177. DOI: 10.3389/fonc.2016.00177.

[60] Agodi C et al. “Charged particle’s flux measurement from PMMA irradiated by 80 MeV/u carbon ion beam”. In: *Phys Med Bio* 57 (2012), pp. 5667–5678. DOI: 10.1088/0031-9155/57/18/5667.

[61] Agodi C et al. “Corrigendum: Charged particle’s flux measurement from PMMA irradiated by 80 MeV/u carbon ion beam”. In: *Phys Med Bio* 59 (2014), 7563–7564. DOI: 10.1088/0031-9155/59/23/7563.

[62] Gwosch K et al. “Non-invasive monitoring of therapeutic carbon ion beams in a homogeneous phantom by tracking of secondary ions”. In: *Phys Med Bio* 58 (2013), pp. 3755–3773. DOI: 10.1088/0031-9155/58/11/3755.

[63] Fischetti M et al. “Inter-fractional monitoring of 12C ions treatments: results from a clinical trial at the CNAO facility”. In: *Scientific Report, Nature* (2020), p. 20735. DOI: 10.1038/s41598-020-77843-z.

[64] Traini G et al. “Review and performance of the Dose Profiler, a particle therapy treatments online monitor”. In: *Phys Med* 65 (2019), pp. 84–93. DOI: 10.1016/j.ejmp.2019.07.010.

[65] De Simoni M et al. “In-room test results at CNAO of an innovative PT treatments online monitor (Dose Profiler)”. In: *Il nuovo Cimento* 41 C (2018), p. 209. DOI: 10.1393/ncc/i2018-18209-2.

[66] Schneider W et al. “Correlation between CT numbers and tissue parameters needed for Monte Carlo simulations of clinical dose distributions”. In: *Phys Med Biol* 45 (2000), p. 459. DOI: :10.1088/0031-9155/45/2/314.

[67] Jiang H et al. “ Adaption of GEANT4 to Monte Carlo dose calculations based on CT data”. In: *Med Phys* 45 (2004), p. 459. DOI: 10.1118/1.1796952.

[68] Parodi K et al. “ Patient study of in vivo verification of beam delivery and range, using positron emission tomography and computed tomography imaging after proton therapy”. In: *Int J Radiat Oncol Biol Phys* 68 (2007), 920–34. DOI: 10.1016/j.ijrobp.2007.01.063.

[69] Mairani A et al. “ The FLUKA Monte Carlo code coupled with the local effect model for biological calculations in carbon ion therapy”. In: *Phys Med Biol* 55 (2010), 4273–89. DOI: 10.1088/0031-9155/55/15/006.

[70] Böhlen T T et al. “ Benchmarking nuclear models of FLUKA and GEANT4 for carbon ion therapy”. In: *Phys Med Biol* 55 (2010), p. 5833. DOI: 10.1088/0031-9155/55/19/014.

[71] Battistoni G et al. “Overview of the FLUKA code”. In: *Ann Nucl Energy* 82 (2015), p. 10. DOI: 10.1016/j.anucene.2014.11.007.

[72] Sommerer F et al. “In-beam PET monitoring of mono-energetic (16)O and (12)C beams: experiments and FLUKA simulations for homogeneous targets”. In: *Phys Med Biol* 54 (2009), p. 3979. DOI: 10.1088/0031-9155/54/13/003.

[73] Enghardt W et al. “Dose quantification from in-beam positron emission tomography”. In: *Radiother Oncol* 73 (2004), S96–8. DOI: 10.1016/S0167-8140(04)80024-0.

[74] Schaffner B et al. “Dose calculation models for proton treatment planning using a dynamic beam delivery system: an attempt to include density heterogeneity effects in the analytical dose calculation”. In: *Phys Med Bio* 44 (1999), pp. 27–41. DOI: 10.1088/0031-9155/57/20/6381.

[75] Parodi K. “Clinical CT-based calculations of dose and positron emitter distributions in proton therapy using the fluka Monte Carlo code”. In: *Phys Med Biol* 52 (2007), 3369–3387. DOI: 10.1088/0031-9155/52/12/004.

[76] Titt U et al. “Comparison of mcnp X and geant 4 proton energy deposition predictions for clinical use”. In: *Phys Med Biol* 57 (2012), 6381–6393. DOI: 10.1088/0031-9155/57/20/6381.

[77] Kohno R et al. “Experimental evaluation of validity of simplified Monte Carlo method in proton dose calculations”. In: *Phys Med Biol* 48 (2003), pp. 1277–88. DOI: 10.1088/0031-9155/48/10/303.

[78] Fippel M and Soukup M. “A Monte Carlo dose calculation algorithm for proton therapy”. In: *Med Phys* 31.8 (2004), pp. 2263–2273. DOI: 10.1118/1.1769631.

[79] Li J S et al. “A particle track-repeating algorithm for proton beam dose calculation”. In: *Phys Med Biol* 50 (2005), pp. 1001–10. DOI: 10.1088/0031-9155/50/5/022.

[80] Yepes P et al. “Monte Carlo fast dose calculator for proton radiotherapy: application to a voxelized geometry representing a patient with prostate cancer”. In: *Phys Med Biol* 54 (2009), N21–28. DOI: 10.1088/0031-9155/54/1/N03.

[81] Bodensteiner D. “RayStation: External beam treatment planning system”. In: *Medical Dosimetry* 43 (2018), pp. 168–176. DOI: 10.1016/j.meddos.2018.02.013.

[82] Mzenda B et al. “Modeling and dosimetric performance evaluation of the RayStation treatment planning system”. In: *Radiation Oncology Physics* 15 (2014), pp. 29–46. DOI: 10.1120/jacmp.v15i5.4787.

[83] *Particle therapy facilities in clinical operation (update July 2020)*. 2020. URL: http://www.fluka.org/fluka.php.

[84] Parodi K et al. “Monte Carlo simulations to support start-up and treatment planning of scanned proton and carbon ion therapy at a synchrotron-based facility”. In: *Phys Med Biol* 57 (2012), p. 3759. DOI: 10.1088/0031-9155/57/12/3759.

[85] Battistoni G et al. “The FLUKA Code: An Accurate Simulation Tool for Particle Therapy”. In: *Frontiers in Oncology* 6 (2016), p. 116. DOI: 10.3389/fonc.2016.00116.

[86] Berger M J. “Monte Carlo Calculation of the penetration and diffusion of fast charged particles”. In: *Methods in Computational Physics* I (1963). Ed. by B Alder, S Fernbach, and M Rotenberg, pp. 135–215.

[87] Mairani A et al. “ A Monte Carlo-based treatment planning tool for proton therapy”. In: *Phys Med Biol* 58 (2013), 2471–90. DOI: 0.1088/0031-9155/58/8/2471.

[88] Chadwick M B, Herman M, and Obložinský P. “ENDF/B-VII.1 Nuclear Data for Science and Technology: Cross Sections, Covariances, Fission Product Yields and Decay Data”. In: *Nuclear Data Sheets* 112.12 (2011). Special Issue on ENDF/B-VII.1 Library, pp. 2887 –2996. ISSN: 0090-3752. DOI: 10.1016/j.nds.2011.11.002. URL: http://www.sciencedirect.com/science/article/pii/S009037521100113X.

[89] Takechi M et al. “Reaction cross sections at intermediate energies and Fermi-motion effect”. In: *Phys Rev C* 79.6 (2009), p. 061601. DOI: 10.1103/PhysRevC.79.061601.

[90] Zhang H Y et al. “Measurement of reaction cross section for proton-rich nuclei (A<30) at intermediate energies”. In: *Nuclear Physics* 707 (2002), p. 303. DOI: 10.1016/S0375-9474(02)01007-2.

[91] Kox S et al. "Direct Measurements of Heavy-Ion Total Reaction Cross Sections at 30 And 83 MeV/Nuclon". In: *Nuclear Physics* 420 (1984), pp. 162–172. DOI: 10.1016/0375-9474(84)90663-8.

[92] Kox S et al. "Transparency Effects in Heavy-Ion Collisions Over the Energy Range 100-300 MeV/Nuclon." In: *Physics Letters* 159 (1985), pp. 15–18. DOI: 10.1016/0370-2693(85)90110-8.

[93] Dudouet J et al. "Double-differential fragmentation cross-section measurements of 95 MeV/nucleon ^{12}C beams on thin targets for hadron therapy". In: *Phys Rev C* 88 (2013), p. 024606. DOI: 10.1103/PhysRevC.88.024606.

[94] Divay C et al. "Differential cross section measurements for hadron therapy: 50 MeV/nucleon ^{12}C reactions on H, C, O, Al, and ^{nat}Ti targets". In: *Phys Rev C* 95 (2017), p. 044602. DOI: 10.1103/PhysRevC.95.044602.

[95] Dudouet J et al. "Zero-degree measurements of ^{12}C fragmentation at 95 MeV/nucleon on thin targets". In: *Phys Rev C* 89 (2014), p. 064615. DOI: 0.1103/PhysRevC.89.064615.

[96] Traini G et a. "Performance of the ToF detectors in the foot experiment". In: *Nuovo Cimento della Societa Italiana di Fisica C* 43 (2020). DOI: 10.1393/ncc/i2020-20016-5.

[97] Dong Y et al. "The Drift Chamber detector of the FOOT experiment: Performance analysis and external calibration". In: *Nuclear Instruments and Methods in Physics Research, Section A: Accelerators, Spectrometers, Detectors and Associated Equipment* 986 (2020). DOI: 10.1016/j.nima.2020.164756.

[98] Morrocchi M et al. "Development and characterization of a ΔE-TOF detector prototype for the FOOT experiment". In: *Nuclear Instruments and Methods in Physics Research, Section A: Accelerators, Spectrometers, Detectors and Associated Equipment* 916 (2019), pp. 116–124. DOI: 10.1016/j.nima.2018.09.086.

[99] Valle S M et al. "The FOOT (FragmentatiOn Of Target) experiment". In: *Nuovo Cimento della Societa Italiana di Fisica C* 41 (2018), p. 169. DOI: 10.1393/ncc/i2018-18169-5.

[100] Andrey A et al. "The foot fragmentation of target experiment". In: *Proceedings of the 15th International Conference on Nuclear Reaction Mechanisms, NRM* (2019), pp. 305–311. URL: https://cds.cern.ch/record/2670292.

[101] Schuemann J et al. "TH-A-19A-02: Expanding TOPAS Towards Biological Modeling". In: *Med Phys* 41 (2014), p. 533. DOI: https://doi.org/10.1118/1.4889535.

[102] Faddegon B et al. "The TOPAS tool for particle simulation, a Monte Carlo simulation tool for physics, biology and clinical research". In: *Physica medica : PM : an international journal devoted to the applications of physics to medicine and biology : official journal of the Italian Association of Biomedical Physics* 72 (2020), pp. 114–121. DOI: https://doi.org/10.1016/j.ejmp.2020.03.019.

[103] Chadwick M B and Young P G. "Proton Nuclear Interactions Up to 250 MeV for Radiation Transport Simulations of Particle Therapy". In: *Proc. Int. Particle Therapy Meeting and PTCOG XXIV* (1996).

[104] Chadwick M B et al. *High-Energy Nuclear Data Libraries for Accelerator-Driven Technologies: Calculational Method for Heavy Recoils*. 1996, pp. 483–489. ISBN: 91-506-1220-4.

[105] Kox S et al. “Trends of total reaction cross sections for heavy ion collisions in the intermediate energy range”. In: *Phys Rev C* 35 (1987), pp. 1678–91. DOI: 10.1103/PhysRevC.35.1678.

[106] Geant4 Collaboration. *Physics Reference Manual*. 2017. URL: https://indico.cern.ch/event/679723/contributions/2792554/attachments/1559217/2454299/PhysicsReferenceManual.pdf.

[107] Malmer C. “ICRU Report 63. Nuclear Data for Neutron and Proton Radiotherapy and for Radiation Protection”. In: *Med Phys* 28 (2001). DOI: 10.1118/1.1369116.

[108] Golovkov M et al. “Fragmentation of 270 A MeV carbon ions in water”. In: *Advances in Hadrontherapy* GSI-97-08 (1997), pp. 316–324.

[109] Matsufuji N et al. “Spatial fragment distribution from a therapeutic pencil-like carbon beam in water”. In: *Phys Med Biol* 50.14 (2004), pp. 3393–403. DOI: 10.1088/0031-9155/50/14/014.

[110] Petti P L et al. “Design of beam modulating devices for charged particle therapy”. In: *Med. Phys.* 18 (1991), pp. 513–518. DOI: 10.1118/1.596655.

[111] Kanai T et al. “Irradiation of Mixed Beam and Design of Spread-Out Bragg Peak for Heavy-Ion Radiotherapy”. In: *Radiation Research* 147 (1997), pp. 78–85. DOI: 10.2307/3579446.

[112] Kanai T et al. “Biophysical characteristics of HIMAC clinical irradiation system for heavy-ion radiation therapy”. In: *International Journal of Radiation Oncology Biology Physics* 44 (1999), pp. 201–210. DOI: 10.1016/S0360-3016(98)00544-6.

[113] Scholz M and Kraft G. “Track structure and the calculation of biological effects of heavy charged particles”. In: *Advances in Space Research* 18.1 (1996), pp. 5–14. ISSN: 0273-1177. DOI: 10.1016/0273-1177(95)00784-C.

[114] Scholz M et al. “Computation of cell survival in heavy ion beams for therapy”. In: *Radiation and Environmental Biophysics* 36 (1997), 59–66. DOI: 10.1007/s004110050055.

[115] Scholz M Kraft G and Bechthold U. “Tumor therapy and track structure”. In: *Radiat Environ Biophys* 38 (1999), 229–237.

[116] Krämer M and Scholz M. “Treatment planning for heavy-ion radiotherapy: calculation and optimization of biologically effective dose”. In: *Phys in Med and Bio* 45.11 (2000), pp. 3319–3330. DOI: 10.1088/0031-9155/45/11/314.

[117] Krämer M and Scholz M. “Rapid calculation of biological effects in ion radiotherapy”. In: *Phys in Med and Bio* 51.8 (2006), pp. 1959–1970. DOI: 10.1088/0031-9155/51/8/001.

[118] Ballarini F et al. “Estimating mixed field effects: An application supporting the lack of a non-linear component for chromosome aberration induction by neutrons”. In: *Radiation Protection Dosimetry* 103.1 (Jan. 2003), pp. 19–27. DOI: 10.1093/oxfordjournals.rpd.a006109.

[119] Magro G et al. “The FLUKA Monte Carlo code coupled with the NIRS approach for clinical dose calculations in carbon ion therapy”. In: *Phys Med Bio* 62 (2017), p. 3814. DOI: 10.1088/1361-6560/aa642b.

Acknowledgments

I will switch to my mother language (with a few exceptions for non-Italian friends) for the most important and difficult part of the thesis: the acknowledgements.
Ritengo infatti che dietro un centinaio di pagine e tre anni di lavoro ci sia anche tutto l'aiuto, lavorativo e soprattutto psicologico, di chi mi è stato vicino.

Per primo ci tengo a ringraziare Prof Pat. Vincenzo sei stato un sostegno costante soprattutto in questo ultimo anno di lockdown in cui ci videochiavamo quotidianamente per risolvere le problematiche del codice, riflettere sui risultati ottenuti, ma soprattutto per raccontarci degli allenamenti in casa, i cibi cucinati, e degli acciacchi comuni che ci ritroviamo! Sei la miglior guida che si possa desiderare in questo mondo tortuoso che è la ricerca.
Grazie Angelo per avermi accompagnato nel fantastico mondo di FRED e grazie per tutta la pazienza.
Grazie Prof Battistoni per aver sempre messo a disposizione la tua esperienza per la realizzazione di questa tesi. I tuoi consigli sono sempre stati fondamentali.

Sicuramente, per superare il dottorato con più risate che pianti, è stato importante il supporto di tutto il gruppo SBAI. Non avrei potuto desiderare di passare le mie giornate con persone migliori, l'unico dispiacere è che l'ultimo anno l'abbiamo dovuto passare a distanza. In particolare grazie Michela, un'amica e la "mamma" del gruppo. Sempre con il consiglio giusto al momento giusto, quando ho un dubbio esistenziale, burocratico, o semplicemente ho bisogno di "parlarne con qualcuno" sicuramente penso a te. Grazie a l'altra colonna portante del gruppo, Alessio. Grazie perché nonostante dopo la magistrale tu non sia stato più il mio relatore, sei (e sempre sarai) un punto di riferimento. Grazie inoltre per le corse dentro il Verano e per appoggiare qualsiasi sfida sportiva con la giusta competitività! Grazie a Toppi per la bellissima musica che consigli. Grazie a Eliana per le risate, le chiacchierate e i fotomontaggi. Nonostante la distanza ti sento sempre molto vicina!
Grazie poi al mitico GrupposuocereDISAGIOeFR. In particolare grazie Riccardo che ormai mi sopporti tutti i giorni da quasi 10 anni. Non avrei mai superato gli ostacoli burocratici, prima universitari e poi del dottorato, senza di te. Ma soprattutto le giornate sarebbero state molto più noiose senza i tuoi gossip e senza condividere con te la passione per il trash. Grazie Giacomo per tutto quello che mi hai insegnato in questi anni, io spero di averti insegnato a rispondere al cellulare per evitare nostri attacchi d'ansia. Proprio per questo, grazie anche per averci sopportato nei nostri momenti più alti di pazzia. Grazie Marta per essere stata con me M&Ms, questo percorso è stato sicuramente più bello condiviso con te. In questi anni ci siamo fatte tantissime risate ma anche pianti, è stato più facile superare alcuni momenti grazie al tuo sostegno. Lucia grazie per le risate, per le parole e i detti popolari che ci hai insegnato. Grazie Gaia per la tua pazzia che si nasconde dietro il viso di una ragazza tutta seria e grazie per tutti gli spettegolamenti.*
Grazie poi all'estensione milanese del gruppo e a tutte le numerose laureande e i pochi laureandi che hanno passato del tempo con noi, ognuno ha lasciato una traccia di sè ma siete troppi per fare l'elenco.

Now I would like to thank all the wonderful people I have been lucky enough to meet at the schools I've done over the years.
Thanks to the "Jägermeister" group of the JUAS. Thanks to Martina, Alex, Markus, Hélèn, Nicolas, Simon, Rakesh, Thomas and Jonas. I have only wonderful memories

of those five weeks spent studying but mostly playing ping-pong, foosball, eating, drinking, and getting to know the wonderful people you are.
Thanks to the "Habibi marriage" group of ESA FAIR radiation summer school. Thanks to Ligia, Francesca, Sofia, Eloise, Claudia, Manuel and Naser. When you meet someone you will form a strong friendship with you feel it immediately and with you it was so. I'm glad we continued to hear from each other often despite the distance, with you it's nice to both be silly, talk about important issues, confide in each other, sharing concerns and good news! You are very smart people and I am sure you will give big contributions to research!

Ringrazio gli amici fisici (e non) che ormai da troppi anni mi sopportano. Grazie Federico, Guido, Vincenzo, Bob, Francesca, Giorgio, Marco, Pb, Cristian, Eugenio, Silvia e Peppe. Siete uno dei più bei doni che ho ricevuto dalla fisica. Grazie Valentina per la tua preziosa amicizia e per aver condiviso con me tante ansie, è sempre bello sapere di non essere soli.

Non posso non ringraziare anche le mie Puzzone. So che ci sarete sempre, che sia per festeggiare o per sfogarsi, per un aiuto, per mangiare, sognare il prossimo viaggio, fare le stupide, parlare di cose serie. Grazie per tutte le volte che avete accettato i miei "non posso devo studiare", "non posso devo lavorare" e grazie per tutte le volte che avete sopportato le mie ansie croniche. Grazie Chiara, Sara, Laura, Alice, Cecilia, Isabella, Floriana, Sofia. Siete la mia certezza.

Un ringraziamento speciale va alla mia famiglia. Mamma e papà grazie per avermi sempre spinto a fare quello che più mi piaceva, appoggiato le mie scelte e stimolato la mia curiosità. Tutti i traguardi che ho raggiunto li devo alle basi che mi avete aiutato a costruire negli anni. Grazie Nicolò perché averti vicino nei momenti di difficoltà che abbiamo passato quest anno è stato veramente importante. Grazie ai nonni, zii (acquisiti e non) e i cugini per esserci sempre.

Per ultimo ho lasciato la persona che più di tutti merita questi ringraziamenti. Grazie Alessandro. Sei sempre riuscito a calmare le mie mille ansie, bastano le tue parole confortanti e i tuoi abbracci per far sembrare tutto più leggero. Grazie perché hai sopportato i miei weekend incasinati tra arbitraggio e dover lavorare alla tesi. Grazie perché senza di te non so come sarei sopravvissuta chiusa in casa, io che ci tornavo solo per dormire, senza sport, nell'ultimo anno di dottorato. Grazie perché mi spingi a pensare al mio futuro senza rischiare di guardarmi indietro con dei rimpianti anche se questo potrebbe dover dire di stare un po' distante da te. Sei la migliore persona che potessi desiderare al mio fianco.